Synthesis, characterization and properties of hybrid organic-inorganic perovskites for photovoltaic applications

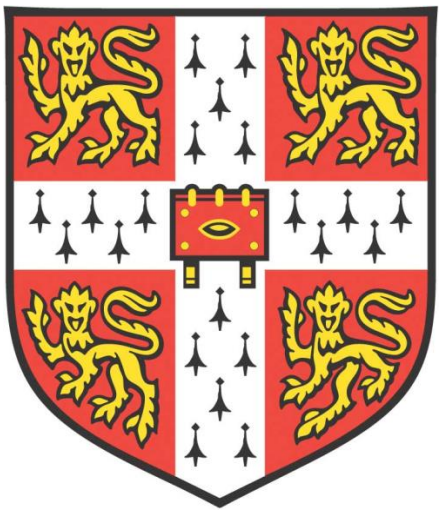

Shijing Sun

Trinity College

Department of Materials Science and Metallurgy

University of Cambridge

This dissertation is submitted for the degree of Doctor of Philosophy

October 2017

Abstract

Synthesis, characterization and properties of hybrid organic-inorganic perovskites for photovoltaic applications

Shijing Sun

The hybrid organic-inorganic perovskites (HOIPs), e.g. methylammonium and formamidinium lead halide (MA/FAPbX_3, X = I, Br or Cl), are a class of materials that has recently achieved remarkable performances in photovoltaic applications. This thesis describes the synthesis, structure and properties of this class of perovskites, with particular focus on their crystal chemistry, mechanical responses and structural diversity.

Understanding the unique crystal chemistry of HOIPs is crucial for device design. While MA-based perovskites have been widely studied, there are still many open questions on the crystal chemistry of FA-based perovskites. In this work, FAPbX_3 (X= Br or I) was shown to undergo a cubic ($Pm\bar{3}m$) to tetragonal ($P4/mbm$) transition on cooling. Studies on the high-pressure crystallography of $FAPbI_3$ exhibited a similar trend and further illustrated band gap tuning via external stimuli. In addition, the cubic lattice of $FAPbBr_3$ was found to be more strained than its MA counterpart. The observed intrinsic strain was modelled with anisotropic line broadening and <100> was found to be the least strained direction.

To explore potential applications in flexible devices, crystals of single (Pb-based) and double (Bi-based) perovskites were probed by nanoindentation and their mechanical properties, such as Young's moduli (*E*) (10 – 20 GPa) and hardnesses *(H)* (0.2 -0.5 GPa), were determined. The mechanical responses of MA- and FA-based hybrid perovskites correlated well with the chemical and structural variations in these analogues, showing a general trend of $E_{Cl} > E_{Br} > E_I$ and $E_{Pb} > E_{Bi}$.

By analogy with classical inorganic perovskites, the hybrid phases can crystallise in both three-dimensional (3D) and low dimensional perovskite-like forms. To improve the stability and remove the toxicity in the current prototypical hybrid perovskites, compositional engineering was applied, focusing on non-toxic bismuth (Bi) as a viable alternative to lead (Pb) in future photovoltaic materials. We report a new layered perovskite, $(NH_4)_3Bi_2I_9$, which exhibits a band gap of 2.0 eV, comparable to $MAPbBr_3$ and $FAPbBr_3$. This work contributes to the materials design goal of more stable and eco-friendly perovskite devices.

To my parents

Shoot for the moon. Even if you miss, you'll land among the stars.

(Norman Vincent Peale)

Declaration

This dissertation is submitted for the degree of Doctor of Philosophy at the University of Cambridge, UK. The research described herein was carried out by myself under the supervision of Professor Anthony K. Cheetham, Goldsmiths' Professor of Materials Science, University of Cambridge. This dissertation is the result of my own work and includes nothing, which is the outcome of work done in collaboration except where declared in the Preface and specifically indicated in the text. It has not been previously submitted, or is being concurrently submitted, in part or whole, to any university of institution for any degree, diploma, or other qualification. This dissertation does not exceed the prescribed word limit.

Shijing Sun

Cambridge, UK

Abstract

Synthesis, characterization and properties of hybrid organic-inorganic perovskites for photovoltaic applications

Shijing Sun

The hybrid organic-inorganic perovskites (HOIPs), e.g. methylammonium and formamidinium lead halide (MA/FAPbX_3, X = I, Br or Cl), are a class of materials that has recently achieved remarkable performances in photovoltaic applications. This thesis describes the synthesis, structure and properties of this class of perovskites, with particular focus on their crystal chemistry, mechanical responses and structural diversity.

Understanding the unique crystal chemistry of HOIPs is crucial for device design. While MA-based perovskites have been widely studied, there are still many open questions on the crystal chemistry of FA-based perovskites. In this work, FAPbX_3 (X= Br or I) was shown to undergo a cubic ($Pm\bar{3}m$) to tetragonal ($P4/mbm$) transition on cooling. Studies on the high-pressure crystallography of $FAPbI_3$ exhibited a similar trend and further illustrated band gap tuning via external stimuli. In addition, the cubic lattice of $FAPbBr_3$ was found to be more strained than its MA counterpart. The observed intrinsic strain was modelled with anisotropic line broadening and <100> was found to be the least strained direction.

To explore potential applications in flexible devices, crystals of single (Pb-based) and double (Bi-based) perovskites were probed by nanoindentation and their mechanical properties, such as Young's moduli (*E*) (10 – 20 GPa) and hardnesses *(H)* (0.2 -0.5 GPa), were determined. The mechanical responses of MA- and FA-based hybrid perovskites correlated well with the chemical and structural variations in these analogues, showing a general trend of $E_{Cl} > E_{Br} > E_I$ and $E_{Pb} > E_{Bi}$.

By analogy with classical inorganic perovskites, the hybrid phases can crystallise in both three-dimensional (3D) and low dimensional perovskite-like forms. To improve the stability and remove the toxicity in the current prototypical hybrid perovskites, compositional engineering was applied, focusing on non-toxic bismuth (Bi) as a viable

alternative to lead (Pb) in future photovoltaic materials. We report a new layered perovskite, $(NH_4)_3Bi_2I_9$, which exhibits a band gap of 2.0 eV, comparable to $MAPbBr_3$ and $FAPbBr_3$. This work contributes to the materials design goal of more stable and eco-friendly perovskite devices.

Acknowledgements

The work carried out through my PhD would have not been possible with the generous help of many people. First and foremost, I would like to express my deepest gratitude to my PhD mentor, Professor Tony Cheetham. I count myself very lucky to have been Tony's student. I have benefited hugely from his immense scientific knowledge and have learned what makes a good scientist by following his example. Over the course of my PhD, Tony has provided countless insights and his great personal qualities have made my experience as a researcher a very happy one. I will always be grateful for the invaluable guidance, encouragement and opportunities Tony gave me. It is thanks to him that I have been able to expand my horizons and realise my potential as a scientist.

My heartfelt thanks go to my friends and co-workers in the FIHM group. Since joining the group as a Part III student, I am very grateful to Professor Wei Li, for his friendliness and for training me on the nanoindentation and X-ray diffraction experiments. My work has been hugely supported by the perovskite sub-team. Special mention goes to Dr. Fengxia Wei, who kindly helped organise my visit to the National University of Singapore, and to Dr. Yue Wu, for his generous advice and encouragement during my thesis writing. I also highly appreciate the help from Dr. Gregor Kieslich, who introduced and took me to my first synchrotron beamtime.

Much collaborative work was done with the computational scientists and I am very thankful to have been working closely with Dr. Paul Bristowe, Zeyu Deng, Dr. Federico Brivio and Dr. Jung-Hoon Lee. I would also like to thank Gregoire Paille from Ecole Normale Supérieure, and Fei Xie, my Part III intern, who helped with my projects during their studies in Cambridge. Furthermore, I greatly appreciate the helpful discussions and so much delightful tea time spent with the current and recent members of FIHM group: Edward Gamblin, Dr. Emma Baxter, Dr. Hamish Yeung, Professor Huaqiang Cao, Dr. Michael Wharmby, Prof. Neng Li, Sammy Shaker, Dr. Satoshi Tominaka, Dr. Sebastian Henke, Dr Shuai Cao, Dr. Sneha Bajpe and Dr. Tom Bennett.

Acknowledgements

I would like to extend my gratitude to our collaborators and my sincere thanks also go to the following researchers for their help throughout my PhD: Professor Judith Driscoll, Professor John Wang, Dr. Qilei Song, Dr. Shan Jiang, Dr. Robert Hoye, Dr. Yanan Fang, Dr. Guan Cao, Dr. Michael Gaultois, Furkan Isikgor, Stefania Cacovich, and Tiesheng Wang. I benefited greatly from the technical expertise from Mary Vickers, Andrew Moss, Andrew Rayment and Robert Cornell at the Materials Science Department, as well as from Dr. Chiu Tang and Dr. Dave Allan at the Diamond Beamlines. In addition, I am grateful to the tutoring I received at the Durham X-Ray Structure Analysis School 2015.

Last but not the least, I would like to say a big thank you to my dear family and friends for all their love, continuous support and company. It has been a privilege for me to spend the past 7 years and a half living in this beautiful town pursuing undergraduate and graduate studies. When I think back on the day I did my first teaching, the evenings I spent in the Trinity College library, those spring flowers on the backs every year and many other memorable days and places – it feels like my second home, and thank you all for making my stay such a wonderful experience.

Supervision and collaborations

The research described in this dissertation was carried out at the Department of Materials Science and Metallurgy, University of Cambridge under the supervision of Professor Anthony K. Cheetham. The work is all original and has been carried out solely by the author or in collaboration with others as detailed below:

Department of Materials Science and Metallurgy, University of Cambridge:

Functional Inorganic and Hybrid Materials Group:

Dr. Fengxia Wei synthesized the double perovskites and worked with the author to prepare lead perovskites. Dr. Gregor Kieslich and the author worked on extending the tolerance factors concept to hybrid systems. Structural characterizations using the Synchrotron facilities were carried out by the author, Dr. Gregor Kieslich, Dr. Yue Wu and Dr. Fengxia Wei. The above colleagues of the author also contributed to the data analysis of single crystal and powder X-ray diffraction. The author supervised Fei Xie (master student) on the study of optical properties of lead-free perovskites and Fei Xie conducted the UV-vis spectrometry measurements.

Atomistic Simulation Group:

Computational studies were conducted in collaboration with the computational scientists under the supervision of Dr. Paul Bristowe. DFT calculations were carried out by Dr. Federico Brivio (on the cation dynamics of $FAPbBr_3$), Dr. Jung-Hoon Lee (on the electronic structure of $(NH_4)_3Bi_2I_9$) and Zeyu Deng (on the electronic structures and elastic properties of $FAPbI_3$, $FAPbBr_3$, and double perovskites). Zeyu also performed *ab initio* molecular dynamics simulations (AIMD) on $MAPbBr_3$ and $FAPbBr_3$.

Department of Chemistry, University of Cambridge:

Elemental analysis was carried out using the microanalysis run by Alan Dickerson.

Supervision and collaborations

Department of Materials Science and Engineering, National University of Singapore:

Single crystals of $FAPbI_3$ and $FAPbBr_3$ were prepared by Furkan Isikgor and posted to the author for nanoindentation experiments.

Department of Materials Science and Engineering, Nanyang Technological University of Singapore:

Single crystals of $MAPbX_3$ (X = I, Br or Cl) were prepared by Dr. Yanan Fang and posted to the author for nanoindentation experiments.

National Institute of Materials Science, Japan:

The author posted single crystals and powder sample of $(NH_4)_3Bi_2I_9$ to Japan and the conductivity measurements of were carried out by Dr. Satoshi Tominaka.

List of publications

Some of the results reported in this thesis have been published in the following peer reviewed journals:

1. G. Kieslich, **S. Sun** and A. K. Cheetham "Solid-state principles applied to organic–inorganic perovskites: new tricks for an old dog", *Chem. Sci.*, 2014, **5**, 4712–4715.

2. **S. Sun**, Y. Fang, G. Kieslich, T. J. White and A. K. Cheetham, "Mechanical properties of organic-Inorganic halide perovskites, $CH_3NH_3PbX_3$ (X=I, Br and Cl), by nanoindentation", *J. Mater. Chem. A*, 2015, **3**, 18450-18455.

3. F. Wei, Z. Deng, **S. Sun**, F. Xie, G. Kieslich, D. M. Evans, M. A. Carpenter, P.D. Bristowe, and A. K. Cheetham, "The synthesis, structure and electronic properties of a lead-free hybrid inorganic–organic double perovskite $(MA)_2KBiCl_6$ (MA= methylammonium)", *Mater. Horiz.*, 2016, **3**, 328-332.

4. Z. Deng, F. Wei, **S. Sun**, G. Kieslich, A. K. Cheetham and P.D. Bristowe, "Exploring the properties of lead-free hybrid double perovskites using a combined computational-experimental approach", *J. Mater. Chem. A*, 2016, **4** 12025-12029.

5. **S. Sun**, S. Tominaka, J. H. Lee, F. Xie, P. D. Bristowe, and A. K. Cheetham. "Synthesis, crystal structure and properties of a perovskite-related bismuth phase, $(NH_4)_3Bi_2I_9$." *APL Materials*, 2016, **4**, 031101.

6. F. Wei, Z. Deng, **S. Sun**, F. Zhang, D. M. Evans, G. Kieslich, D. M. Evans, S. Tominaka, M. A. Carpenter, J. Zhang, P.D. Bristowe, and A. K. Cheetham, "The synthesis and properties of a lead-free hybrid inorganic–organic double perovskite $(CH_3NH_3)_2AgBiBr_6$", *Chem. Mater.*, 2017, **29**, 1089-1094.

7. **S. Sun**, Z. Deng, Y. Wu, F. Wei, F. H. Isikgor, F. Brivio, M. W. Gaultois, J. Ouyang, P. D. Bristowe, A. K. Cheetham and G. Kieslich, "Variable temperature and high-pressure crystal chemistry of perovskite formamidinium lead iodide: a single crystal X-ray diffraction and computational study", *Chem. Comm.*, 2017, 017, **53**, 7537-7540.

8. **S. Sun**, F. H. Isikgor, Z. Deng, F. Wei, G. Kieslich, P. D. Bristowe, J. Ouyang and A. K. Cheetham, "Factors influencing the mechanical properties of

formamidinium lead halides and related hybrid perovskites", *ChemSusChem,* 2017, accepted manuscript.

Results in the following peer reviewed journals, which have been also published during the author's PhD, are not included in this thesis:

1. G. Kieslich, **S. Sun** and A. K. Cheetham, "An extended Tolerance Factor approach for organic–inorganic perovskites", *Chem. Sci.,* 2015, **6**, 3430-3433.
2. G. Kieslich, S. Kumagai, K. T. Butler, T. Okamura, C. Hendon, **S. Sun**, M. Yamashita, A. Walsh and A. K. Cheetham, "Role of entropic effects in controlling the polymorphism in ferroelectric metal-organic frameworks", *Chem. Commun.*, 2015, **51**, 15538-15541.
3. **S. Sun**, S. Henke, M. Wharmby, H. H.-M. Yeung, W. Li and A. K. Cheetham, "Mechanical properties of a calcium dietary supplement, calcium fumarate trihydrate". *Inorg. Chem.*, 2015, **54**, 11186–11192.
4. G. Kieslich, A. C. Forse, **S. Sun**, K. T. Butler, S. Kumagai, Y. Wu, M. R. Warren, A. Walsh, C. P. Grey, and A. K. Cheetham. "Role of amine–cavity interactions in determining the structure and mechanical properties of the ferroelectric hybrid perovskite $[NH_3NH_2]Zn(HCOO)_3$." *Chem. Mater.*, 2016, **28**, 312–317.
5. G. Kieslich, S. Kumagai, A. C. Forse, **S. Sun**, S. Henke, M. Yamashita, C. P. Grey, and Anthony K. Cheetham. "Tuneable mechanical and dynamical properties in the ferroelectric perovskite solid solution $[NH_3NH_2]_{1-x}[NH_3\,OH]_x$ Zn $(HCOO)_3$." *Chem. Sci.*, 2016, **7**, 5108-5112.
6. Q. Song, S. Jiang, T. Hasell, M. Liu, **S. Sun**, A. K. Cheetham, E. Sivaniah, and A. I. Cooper. "Porous organic cage thin films and molecular-sieving membranes." *Advanced Materials***,** 2016, **28**, 2629–2637.
7. T. Wang, M. Farajollahi, S. Henke, T. Zhu, S. R. Bajpe, **S. Sun**, J. Barnard, J. S. Lee, J. D. W. Madden, A. K. Cheetham and S. K. Smoukov, "Functional conductive nanomaterials *via* polymerisation in nano-channels: PEDOT in a MOF", *Mater. Horiz.***,** 2017, **4**, 64-71.
8. C. Guan, W. Zhao, Y, Hu, Z. Lai, X. Li, **S. Sun**, H. Zhang, A. K. Cheetham and J. Wang, "Cobalt oxide and N-doped carbon nanosheets derived from a single

two-dimensional metal–organic framework precursor and their application in flexible asymmetric supercapacitors", *Nanoscale Horiz.* 2017, **2**, 99-105.

9. S. Jiang, Q. Song, A. Massey, S. Y. Chong, L. Chen, **S. Sun**, T. Hasell, R. Raval, E. Sivaniah, A.K. Cheetham, and A. I. Cooper, "Oriented 2D porous organic cage crystals", *Angew. Chem., Int. Ed.*, 2017, accept manuscript.

Contents

List of abbreviations and acronyms

0D, 1D, 2D or 3D	zero, one, two or three-dimensional (perovskites)
AIMD	*ab initio* first principle molecular dynamics
ADP	anisotropic displacement parameter
DFT	first principle density functional theory
DOS	density of states
E	Young's modulus
FA	formamidinium ion, $(NH_2)_2CH^+$
FWHM	full width at half maximum
GUA	guanidinium ion, $C(NH_2)_3^+$
H	hardness
HOIP	hybrid organic-inorganic perovskites
HP	high pressure
MA	methylammonium ion, $CH_3NH_3^+$
p	pressure
PXRD	powder X-ray diffraction
SCXRD	single crystal X-ray diffraction
T	temperature
TGA	thermogravimetric analysis
VT	variable temperature

Aim of the research and organisation of this thesis

Renewable energy sources have attracted increasing attention in recent years due to growing global energy demands as well as environmental considerations. Research and development into promising new materials and devices that improve the use of renewable energy, for example solar cells and eco-friendly light emitting diodes, have been under the spotlight in both academia and industry. Among these initiatives, a relatively young class of organic-inorganic materials, namely hybrid organic-inorganic perovskites (HOIPs), has recently achieved remarkable success in photovoltaic devices. In particular, the efficiencies of solar cells using prototypical lead hybrid perovskites, for example, methylammonium lead iodide ($MAPbI_3$), have soared from less than 4% in 2009[1] to over 22% by the start of 2017.[2]

However, despite the intensive research efforts in this area, the commercialization of hybrid perovskite solar cells faces two major challenges: the stability of the halide HOIPs and the toxicity of lead. This research addresses the structural, chemical and mechanical stability of the known perovskites, as well as to exploring the structural diversity of HOIPs and alternatives to the prototypical $MAPbI_3$.

The thesis comprises seven chapters. The research background is given in the introductory Chapter 1, followed by experimental methods in Chapter 2. Chapter 3 and 4 are devoted to studies of a family of 3D hybrid halide perovskites, formamidinium (FA) lead halides. The crystal chemistry of $FAPbI_3$ and $FAPbBr_3$ under external stimuli such as temperature and pressure is described in Chapter 3 and the intrinsic strain in $FAPbBr_3$ is modelled in Chapter 4. In Chapter 5, the mechanical properties of the MA- and FA-based perovskites and double perovskites are discussed in detail. Hybrid perovskite-related architectures are explored in Chapter 6, focusing on employing Bi as an alternative to Pb in photovoltaic applications. General conclusions and the future outlook for the field are outlined in Chapter 7. Finally, references and appendix are listed at the end of the thesis as supplementary information.

Chapter 1 Introduction

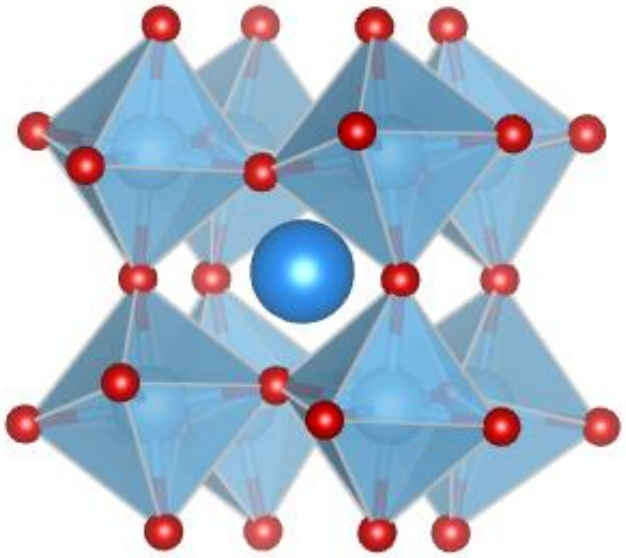

This chapter outlines the research background of this thesis. There is currently a lot of attention drawn to halide HOIP materials, which have recently revolutionized the area of new generation solar cells. The development of HOIPs and perovskite materials for photovoltaic applications are first reviewed, and the recent interest in materials chemistry as well as the structure-property relationships of the HOIPs are then discussed.

1.1 Overview of HOIPs

1.1.1 A brief history of hybrid perovskites

Following his discovery of $CaTiO_3$ in 1839, German mineralogist Gustav Rose named this mineral after the Russian mineralogist and aristocrat Count Lev Perovski. Today the word perovskite is a general term to describe crystals strucutral analogues of $CaTiO_3$.[3] Perovskite structures have the general chemical formula of ABX_3, where an A site cation sits in the cavity of BX_6 octahedron, as shown in Figure 1-1 (a). In addition to the three-dimensional (3D) perovskites, this family of materials also includes low dimensional perovskites (blocks of 3D perovskite structure separated by additional motifs, e.g. $A_{n+1}B_nX_{3n+1}$)[4] and double perovskites (e.g. $A_2B^IB^{III}X_6$).[5] Materials with perovskite or perovskite-like structures have played a central role in the development of condensed matter physics and materials chemistry over the last few decades.[6,7] Among those, the development of inorganic perovskite oxides (ABO_3) has been particularly significant for a wide range of applications such as ferroelectrics, high-temperature superconductors, and giant magnetoresistance devices.[8]

Traditionally, the field of materials chemistry has been divided into organic and inorganic systems. However, in the last few decades, a new class of materials, often referred to as hybrid organic-inorganic frameworks, has attracted considerable attention since their enormous structural and chemical diversity leads to potential technological applications beyond either purely organic or inorganic systems.[9,10] HOIPs are a subclass of the perovskite family, in which at least one of sites is replaced by organic cations or organic linkers. An example of a halide HOIP is methylammonium lead iodide ($MAPbI_3$), where the A-site cavity is filled by the organic amine (Figure 1-1 (b)). HOIPs can also have a diverse range of linkers on the X-site, including halides, azides, formates, dicyanamides, cyanides and dicyanometallates.[11] As shown in Figure 1-1 (c), metal formates $AB(HCOO)_3$ (A = protonated amine, B = divalent metal) exhibit multiferroic behaviour[12] and tuneable mechanical properties.[13]

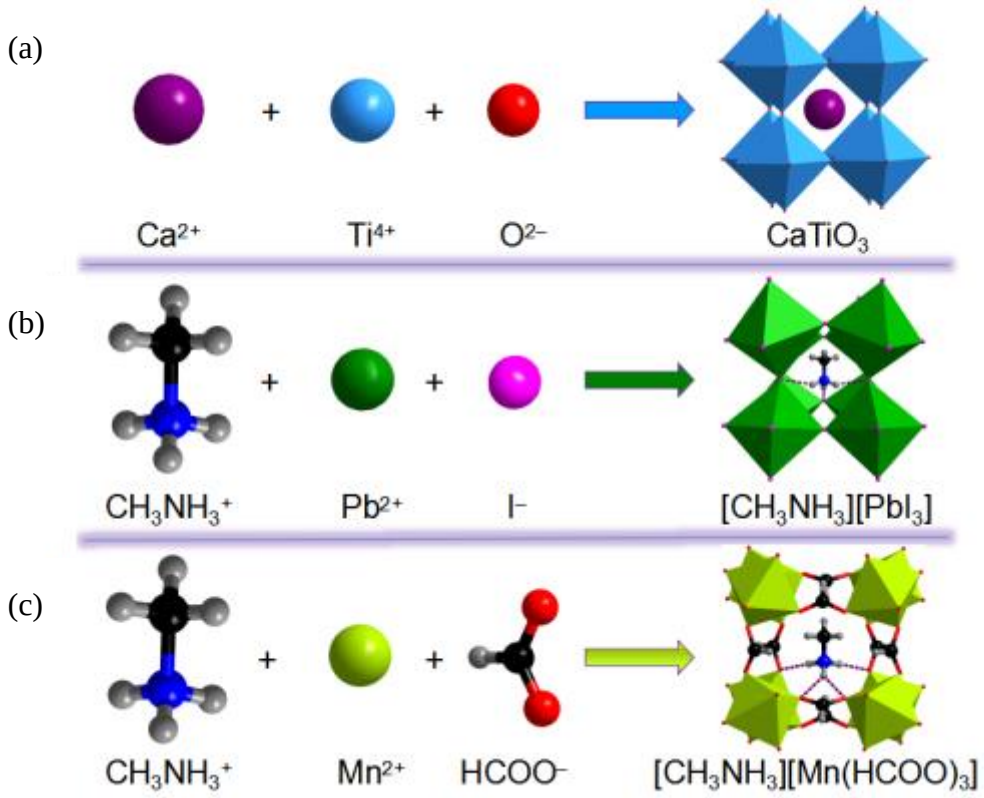

Figure 1-1 Evolution from perovskite oxides to HOIPs with organic A-site, then to HOIPs with both organic A- and X-sites. Reproduced from Cheetham *et al.* [11]

Research in HOIPs has recently attracted a lot of attention in both materials science and the renewable energy community, due to the intriguing properties of the hybrid halide perovskites, especially $MAPbI_3$, for photovoltaic applications. Hybrid halide perovskites and related structures are a subclass of the HOIPs where the A site is occupied by an ammonium cation, the B site contains a divalent Group IV metal, and the X site contains a halogen anion. The cubic perovskite structure of $MAPbX_3$ (MA = methylammonium and X = I, Br, Cl) was firstly reported by Weber in 1978.[14] However, studies of these materials for optoelectronic devices did not start until the 1990s. Pioneered by Mitzi *et al*. at IBM,[4,15] a range of semiconducting perovskite-like materials with remarkable structural versatility was developed for optoelectronic applications, such as in light-emitting diodes (LEDs) and transistors.[16,17] The exceptional utility of hybrid halide perovskites for photovoltaic applications, on the other hand, only started in 2009, when a photoelectrochemical cell incorporating a layer of $MAPbI_3$ as a visible light sensitiser was reported by Miyasaka *et al.*[1] The initial power conversion efficiencies were 3.1% and 3.8% with $MAPbBr_3$ and $MAPbI_3$ respectively.

1.1.2 Recent emergence of perovskite solar cells

With minimum detrimental impact on the environment, solar energy is arguably the most abundant clean energy source and has been promoted as a reliable alternative to fossil fuels in the context of future sustainable economic growth.[18] For the past 40 years, the solar cell industry has been dominated by silicon based solar cells due to their high efficiency and low costs. New generation solar cells have also been developed based on CdTe and CIGS ($CuIn_{1-x}Ga_xSe$), as well as organic dyes [18] The rapid increase in perovskite cell efficiency in recent years is illustrated in Figure 1-2.

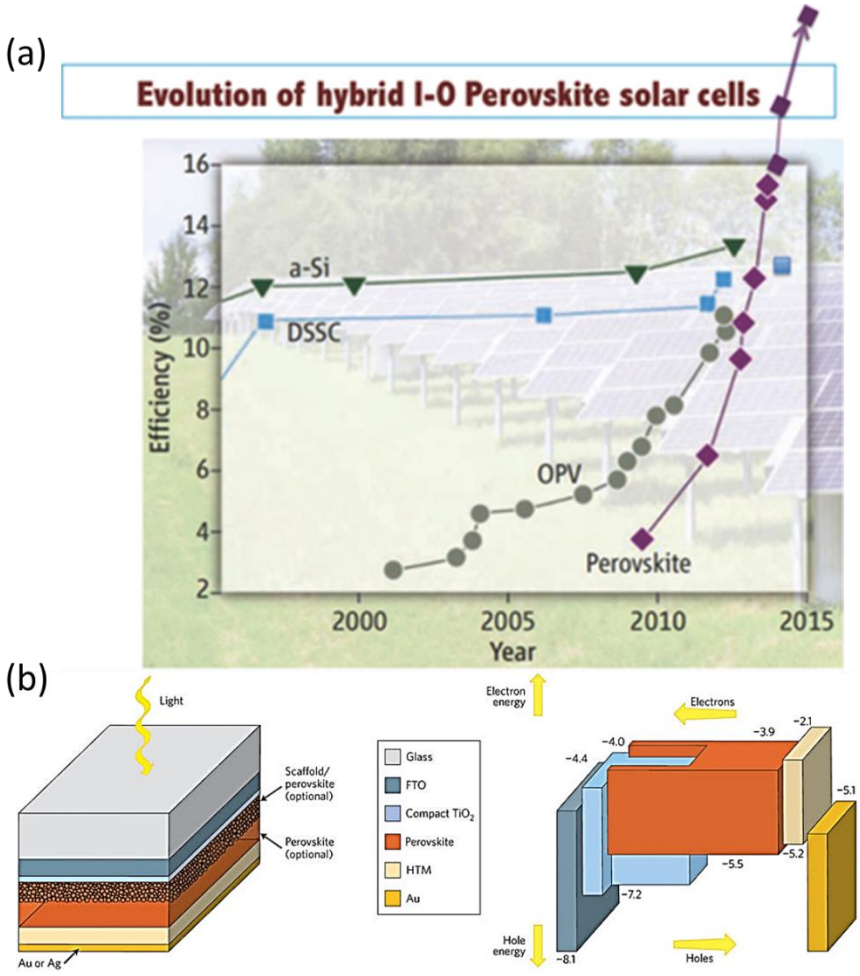

Figure 1-2 (a) Electrical power conversion efficiency of the best cells at the time. OPV: organic photovoltaics; DSSC: dye-sensitized solar cell; a-Si: amorphous Si solar cell. Reproduced from Cahen *et al.*[19] (b) Illustration of a general perovskite solar cell (left) and vacuum energy levels (in eV) for corresponding materials (right). Reproduced from Snaith *et al.*[20]

Despite the low initial conversion efficiency when hybrid perovskites first re-entered into the literature as visible-light sensitizers for photovoltaic devices in 2009,[1] rapid progress

has been made following the development of solid-state perovskite devices.[21,22] By the end of 2013, around the time when the research described in this thesis began, the power efficiency of perovskite solar cells had already reached over 16%.[2] Due to advances in materials processing and improved device architectures, perovskite solar cells have now (2017) achieved a certified laboratory efficiency of 22.1% in just over 7 years of research.[2] This number has exceeded the conversion efficiencies of organic and dye sensitised solar cells (around 10%), and it is approaching that of crystalline silicon (around 25%). According to the theory of Shockley–Queisser limit, the maximum theoretical solar conversion efficiency is around 33.7% for a solar cell using a single p-n junction with an optimal band gap of 1.34 eV.[23]

The halide perovskites have been used as a light absorber and as an electron and hole transporter in solar cells.[24] Mesoporous TiO_2-based solar cells, where the perovskites were used as light sensitizersm were firstly introduced. A breakthrough was soon achieved by applying meso-superstructured solar cells based on metal oxides, were Al_2O_3 and TiO_2 were merely as a scaffold layer for the halide perovskite.[21,25] Shortly after, planar heterojunction-structured perovskite solar cells were also developed, which took into account of the bifunctional property (light harvesting and charge transporting) of perovskites and avoided using the mesoporous oxides. The structural progresses of perovskite solar cells are shown in Figure 1-3.[26]

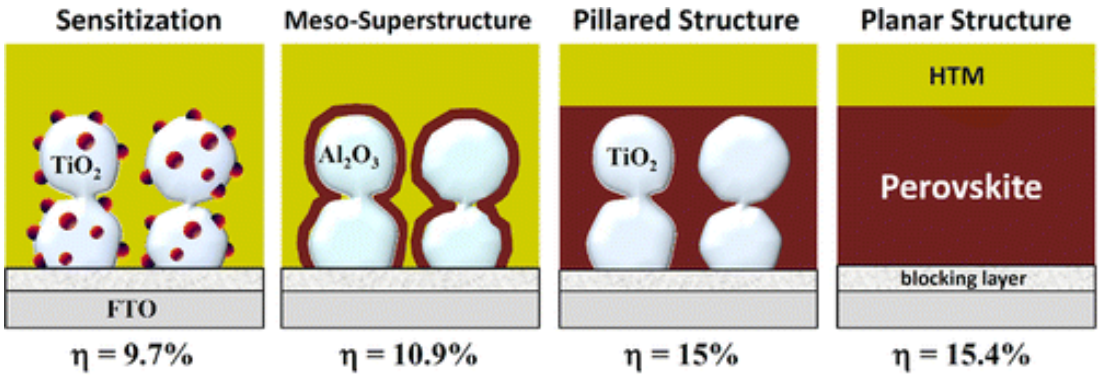

Figure 1-3 Structural progress of perovskite-based solid-state solar cells from a perovskite dot deposited on TiO_2 with an efficiency of 9.7% to a planar p-n junction with efficiency of 15.4%, via the meso-superstuructured scaffold. Reproduced from Park *et al*.[26]

The extraordinary performance of this family of hybrid perovskites has been attributed to their large absorption coefficients, direct bandgaps, long-range electron-hole transport lengths, and high charge carrier mobilities.[21,27,28] The prototypical hybrid halide perovskites, especially $MAPbI_3$, have opened up a new route to achieve low cost, low temperature and solution processable photovoltaic devices.[29,30] Therefore, much current research is focused on the controlled tuning of materials composition, film morphology and device design, in order to understand the mechanism of charge transport as well as further enhance the conversion efficiencies of the perovskite solar cells and develop perovskite optoelectronic devices.[21,27,28,31–39] Furthermore, single crystals have attracted increasing attention due to their high diffusion lengths compared with polycrystalline thin films, which is critical for achieving high PV efficiencies.[40,41] In addition, these HOIPs have also shown potential in areas such as light emitting diodes, field effect transistors, ultra-lasers, photodetectors, and solar thermoelectric applications.[34,36,42–45]

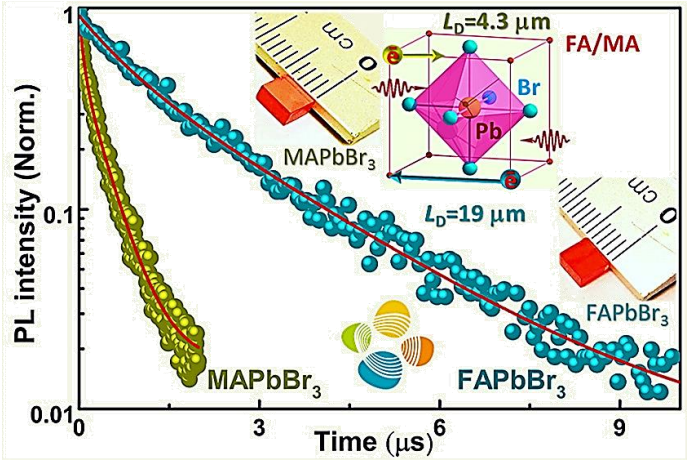

Figure 1-4 Photoluminescence of $FAPbBr_3$ and $MAPbBr_3$ single crystals. Reproduced from Bakr *et al.*[46]

While initial attempts used $MAPbX_3$ (X = I, Br or Cl), formamidium-based perovskites, $FAPbX_3$ ($FA = CH(NH_2)_2^+$), have become a focus of attention due to their superior transport properties,[47] improved thermal stability at high temperatures,[29] and more optimal bandgaps.[48] Alloys of FA/MA have been shown to combine high efficiency and stability.[49–52] Bakr *et al.* observed long carrier dynamics in FA-based perovskites, with carrier diffusion lengths measured to be 6.6 μm for $FAPbI_3$ and 19.0 μm for $FAPbBr_3$ crystals. Figure 1-4 shows that the $FAPbBr_3$ crystals displayed a 5-fold longer

carrier lifetime and 10-fold lower dark carrier concentration than those of $MAPbBr_3$ single crystals.

1.2 The $APbX_3$ perovskites

1.2.1 Synthesis and phase stability

Most current studies on halide HOIPs for photovoltaic applications focus on lead halide perovskites, which achieved the record-breaking conversion efficiencies of perovskite solar cells. Following the solution method developed by Poglitsch and Weber in 1987,[53] the overall synthesis for lead halide perovskites involves two steps: a) the preparation of amine halide and then b) the synthesis of perovskites. For example, a typical synthesis route for thin film $MAPbI_3$ is to dissolve the mixture of MAI and PbI_2 in γ-butyrolactone or anhydrous N,N-dimethylformamide (DMF) and thin films are produced by spin coating with annealing.[24,30] Although thin films are beneficial for device fabrications, single crystals are desirable for the study and analysis of the material itself.[47,54] For crystal and bulk powder samples, solid MAI is commonly prepared by mixing excess methylamine solution (in methanol or ethanol) with hydriodic acid aqueous solution (HI) and then removing the solvent.[24] A typical synthesis for $MAPbI_3$ crystals involves heating MAI and PbI_2 or $Pb(CH_3COO)_2$ in HI solution or organic solvent (e.g. anhydrous ethanol[55]) up to 120 ^oC and black crystals can be harvested upon cooling.[54,56,57] Large single crystals of $MAPbI_3$ with sizes up to 2 mm in length have been reported by White *et al*. as seen in Figure 1-5. The crystal exhibited a tetragonal structure at room temperature with space group of $I4/mcm$. An orthorhombic to tetragonal transition has been observed at 161.4 K, and a tetragonal to cubic transition at 330.4 K.

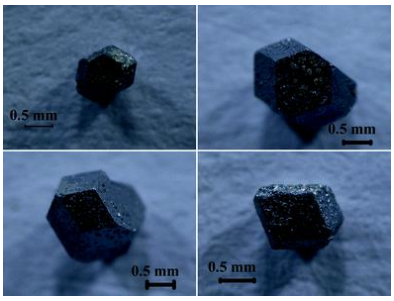

Figure 1-5 Example images of the $MAPbI_3$ single crystals grown using the method described by Poglitsch and Weber. Reproduced from White *et al*.[56]

Figure 1-6 shows a representative $APbX_3$ perovskite structure.[58,59] It is built upon corner-sharing PbX_6 octahedra, which are emphasized by pink shaded polyhedra, and A cations filling the 12-fold coordination site formed in the middle of the cube of eight octahedra. The aristotype perovskite architecture adopts the cubic space group $Pm\bar{3}m$. For hybrid halide perovskites, this means that the organic cations on the A-site, in this case MA or FA, are fully disordered to reflect the symmetry.

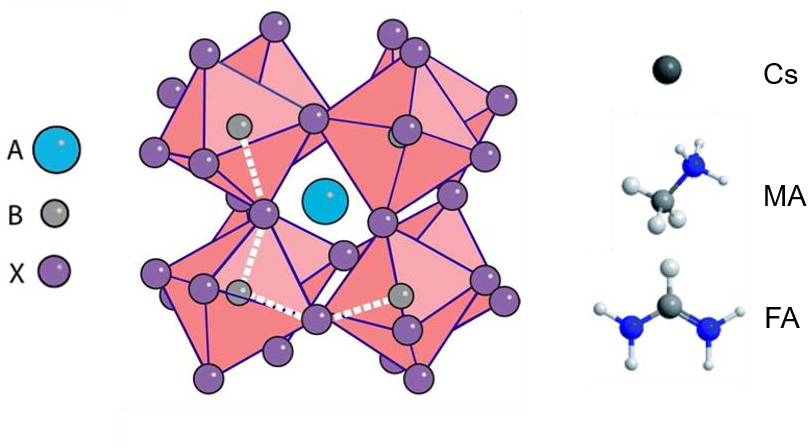

Figure 1-6 Distorted perovskite crystal structures with low temperature orthorhombic symmetry. For the perovskites of photovoltaic interest, A = Cs, MA or FA; B = Pb, and X = Br, I. Reproduced from Green *et al.*[59]

Under external stimuli, such as low temperature or high pressure, successive phase transitions with distorted perovskite structures have been observed.[60,61] The complex symmetry lowering in these phase transitions is commonly described using octahedral tilt notation.[62–64] The octahedral tilts in hybrid halide perovskites are similar to those in found in purely inorganic perovskites, for example, in caesium lead halide perovskites.[65,66] However, the anisotropy of the amine cation allows extra phase transitions resulting from the order–disorder transition of the cations, as seen by neutron diffraction.[67] In contrast to their inorganic counterparts, the MA and FA cations in HOIPs also interact with the framework through hydrogen bonding, which further affects their phase transitions, octahedral tilting and disorder.[68] As shown in Figure 1-6, distorted perovskite structures with an orthorhombic tilt pattern ($a^-b^+a^-$ in Glazer notation) show B-X-B angles deviating from 180°. These structural distortions modify the perovskites' physical properties such as band gaps, mechanical responses, and possible ferroic responses.[69–72]

In addition to phase transitions due to octahedral tilting, the existence of non-perovskite polymorphs of the same composition also contributes to the phase instability of some common hybrid perovskite structures. For example, the structural instability of the black polymorph of $FAPbI_3$ has been a major concern in its device applications because the perovskite crystals transform into its yellow polymorph after in air for a few days. The perovskite-type polymorph of $FAPbI_3$ is metastable at room temperature. The yellow polymorph consists of chains of face sharing octahedra along the <001> direction with FA cations sitting between the inorganic chains. This low dimensional perovskite-like phase is the thermodynamically stable phase under ambient conditions, with electronic properties that are less favourable for photovoltaic applications.[66,73,74]

1.2.2 Optical properties

Hybrid halide perovskites of MA and $FAPbX_3$ show superior semiconducting properties with direct bandgaps, which means that the momentum of electrons and holes is the same in the conduction and valence bands and therefore, an electron can directly emit a photon.[75] The band gaps of this class of hybrid perovskites range from 1.48 eV ($FAPbI_3$),[76] 1.55 eV ($MAPbI_3$),[77] 2.23 eV ($FAPbBr_3$),[29] 2.35 eV ($MAPbBr_3$),[77] to over 3 eV ($MAPbCl_3$).[78] The iodide perovskites' band gaps are close to the optimal value of 1.1–1.5 eV for single-junction photovoltaic devices (Shockley−Queisser limit).[79] The bandgaps of the hybrid halide perovskites are predominantly determined by the inorganic framework due to the strong contribution of the halide *p* orbitals to the optical transition. Considering the effect of the A-site cations, on the other hand, the 2*p* orbitals of carbon and nitrogen as well as the hydrogen 1*s* orbitals do not contribute significantly to the density of states near the Fermi level. However, the steric effect of the A-site cations can cause lattice expansion and hence leads to different B-X bond lengths and bond angles, indirectly varying the band gap.[50] The bandgaps of the halide HOIPs can be tuned by compositional engineering (see Chapter 1.3) and external stimuli. For example, Figure 1-7 shows the change in bandgaps of $MAPbI_3$ and $MAPbBr_3$ with temperature. The sharp absorption edges indicate direct band gaps.

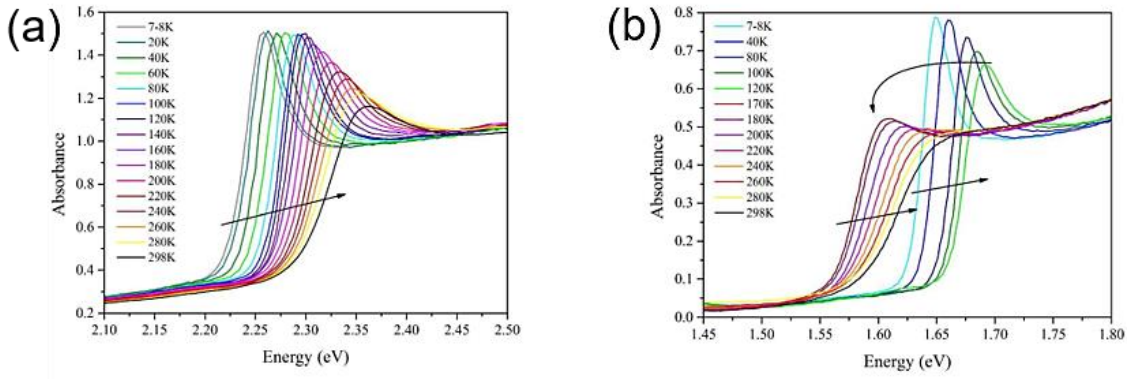

Figure 1-7 Absorbance measurements of (a) $MAPbBr_3$ and (b) $MAPbI_3$ over a wide temperature range. Reproduced from Green *et al.*[59]

1.2.3 Challenges in the application of hybrid perovskites

To date, the majority of hybrid perovskites investigated for optoelectronic applications have been based on lead halides. There are two main challenges faced by researchers in the commercialising of hybrid perovskites:

1) The most popular compositions of hybrid lead halide perovskites lack chemical stability. For instance, $MAPbI_3$ is moisture and temperature sensitive.[56]

2) The toxic lead content in perovskite devices raises environmental concerns and is problematic for their widescale deployment.[80]

In order to overcome these limitations, there has been increasing research on improving stability via compositional engineering such as alloying, [74,81,82] and searching for lead-free perovskites for photovoltaic applications.[83–85] These two aspects are reviewed in the next section.

1.3 Compositional engineering

1.3.1 Substitutions and solid solutions

Structural flexibility in hybrid halide perovskites allows desired properties to be targeted by compositional variation. The aim of the compositional engineering of HOIPs is to tune the materials' properties and to improve their stability. For example, band gap engineering could be achieved by exploring alternative ions on A, B or X-sites as well as introducing solid solutions.

To date, there are only a few 3D hybrid perovskite systems showing outstanding semiconducting properties that can be used in photovoltaic devices. Combinations of the following compositions have been reported in perovskite based solar cells since 2009:

A - Site: MA or FA

B - Site: Pb^{2+}, Sn^{2+} or Ge^{2+}

X - Site: Cl^{-}, Br^{-} or I^{-}

These compositions exhibit orthorhombic, trigonal, tetragonal or cubic symmetry at room temperature and show a range of potential optoelectronic applications in photovoltaics, laser physics, light-emitting diodes, and deformable displays. Note that inorganic halide perovskites, for instance the caesium based systems, are also being studied extensively.[86–90] $CsPbI_3$ undergoes a reconstructive phase transition from a 1-D PbI_6 edge-sharing structure to a 3-D perovskite between 560 and 600 K.[65,91] The ionic radii of monovalent cations follow the trend Cs < MA < FA. It has also been experimentally shown that the bandgap has the reverse trend.[66,79] Furthermore, the band gap follows the trend of $AGeI_3$ < $ASnI_3$ < $APbI_3$, because the angle of X-M-X increasingly diverges from 180° as we go down the periodic table, in addition to the decrease in covalent character of the M-I bonds.[79]

The majority of studies on 3D perovskites are based on Pb and Sn, with a few reports on Ge.[79] However, the preferred oxidation states of Sn^{4+} and Ge^{4+} reduce the stability of the divalent state in these structures in air. A recent report on a Sn based solar cell achieved an efficiency of 6.8%, which is poorer than the performance of Pb perovskite solar cells.[83] The band gaps of halide perovskites have been observed to have the trend AMI_3 < $AMBr_3$

< $AMCl_3$.[57] This is due to the increase in covalent character of anions as we move downwards on the periodic table (the trend is reversed for cations). On the other hand, research on mixed halide perovskites showed that the bandgaps of the solid solutions of Br- and I-based perovskites covered almost the entire visible spectrum.[92]

Interestingly, devices made from mixed halide solid solutions $MAPbI_{3-x}Br_x$. showed that low Br content (<10%) gave the best initial efficiency whereas higher Br content (>20%) gave the best stability.[58,77] With the moisture sensitivity of these cells starting to be widely recognized as a serious problem, compositional engineering also aims to improve their structural stability. Mixed cation and dual site alloying have been recently reported as an efficient way to improve the stability perovskite phase of $FAPbI_3$ by, for example, stress relaxation,.[73,93] The thermal and structural stability of the perovskite modification was recently improved using a solid-solution approach, for example, perovskite solar cells incorporating $FAPbI_3$ in the absorber layer ($(FAPbI_3)_{0.85}(MAPbBr_3)_{0.15}$) have achieved a certified power conversion efficiency of 20.1%.[76]

1.3.2 Double perovskites

In the search for alternatives to $MAPbI_3$, lead-free double perovskites have recently been shown to be a promising approach. As shown in Figure 1-8, in such structures the perovskite formula is essentially doubled and each pair of divalent metal cations, *e.g.* Pb^{2+} cations,is replaced by a combination of one monovalent and one trivalent cation. The inorganic analogues of double perovskites have been well known as elpasolites since the 70s, where structures with the formula of $A_2B^IB^{III}X_6$ (A and B^I = Li, Na, K, Rb, Cs, Tl, Ag, etc.; B^{III} = Al, Bi, Fe, Ga, Ln, etc.; and X = F, Cl, Br, or CN) were reported. [94,95] In 2016, Cs_2AgBiX_6 (X = Cl or Br) was firstly reported in the context of an alternative to the lead perovskites for photovoltaic applications.[96–98] The Cs-based double perovskites crystallize in cubic $Fm\bar{3}m$ symmetry at room temperature and show light absorption in the visible range of the spectrum. In the meantime, efforts to search for hybrid double perovskites were also underway. We recently reported $(MA)_2KBiCl_6$ (band gap of 3.0 eV)[99], $(MA)_2AgBiBr_6$ (band gap of 2.02 eV)[100] and $(MA)_2TlBiBr_6$ (direct band gap of 2.16 eV)[101] with remarkable structural, thermal and mechanical stabilities comparable to

their single perovskite counterparts. The crystal structure of $(MA)_2AgBiBr_6$ is illustrated in Figure 1-8.

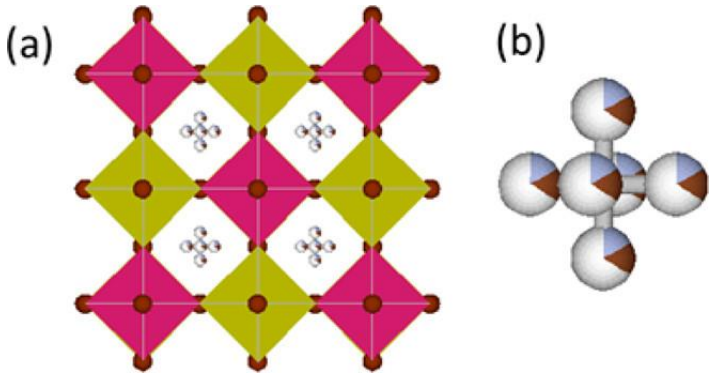

Figure 1-8 (a) Crystal structure of $(MA)_2AgBiBr_6$ with space group $Fm\bar{3}m$ at room temperature. Purple and yellow octahedra represent $BiBr_6$ and $AgBr_6$, respectively. (b) MA cation shown after rotation by 5° clockwise along the *c* axis for better illustration. Partial occupancies were applied to show the disorder of the MA cations. Reproduced from Cheetham *et al.*[100]

1.3.3 Perovskite-related architectures

To form a 3D perovskite structure, the size of the organic cation at A site is limited by the size of the 3D cavity into which it must fit. In 1926, V.M. Goldschmidt introduced the concept of a tolerance factor (*t*), to evaluate the ionic size mismatches a 3D perovskite structure can tolerates until a different structure type is preferentially formed:[102]

$$t = (r_A + r_X)/\sqrt{2}(r_B + r_X)$$

where r_A, r_B, and r_X are the effective ionic radii for the ions in the A, B, and X-sites, respectively.

The tolerance factor has been widely used as a guiding rule to explore the structures of oxide perovskites. For values of *t* close to 1, mostly cubic perovskites are found, whereas values of 0.80 – 0.89 predominantly lead to distorted structures which can be further classified using Glazer's concept of octahedral tilting.[62] Below ~0.80 other structure types such as the ilmenite-type ($FeTiO_3$) are more stable due to the similar sizes of the cations *A* and *B*. Values of *t* larger than 1 commonly lead to low dimensional architectures. For instance, hexagonal layered structures have been observed in oxide perovskites.[103] In the case of halide perovskites, using *t* = 1 as the upper limit and considering the size of cations

in iodoplumbates (R_{Pb} = 1.19, R_I = 2.20 Å), it is shown that only small organic cations, that have sizes smaller than ~2.6 Å (i.e. those consisting of three or less C–C or C–N bonds) are expected to form 3D perovskite frameworks.[15] If larger cations are used instead, lower dimensional perovskite-like structures such as 2D layered, 1D chain or 0D molecular forms are obtained. As shown in Figure 1-9, 3D perovskites can tranform into layered perovskite-like structures along different crystallographic directions, leading to different stoichiometries.[104] For example, iodostannates with the general formulas of $(C_4H_9NH_3)_2$ $(CH_3NH_3)_{n-1}Sn_nI_{3n+1}$ (n=1-5)[4] and $[NH_2C(I)=NH_2]_2(CH_3NH_3)_{n-1}Sn_nI_{3m+2}$ (m = 2 to 4)[16] possess stepwise increases in conductivity with increasing n and m, up to the fully 3-D framework of $CH_3NH_3SnI_3$ which has the highest conductivity.

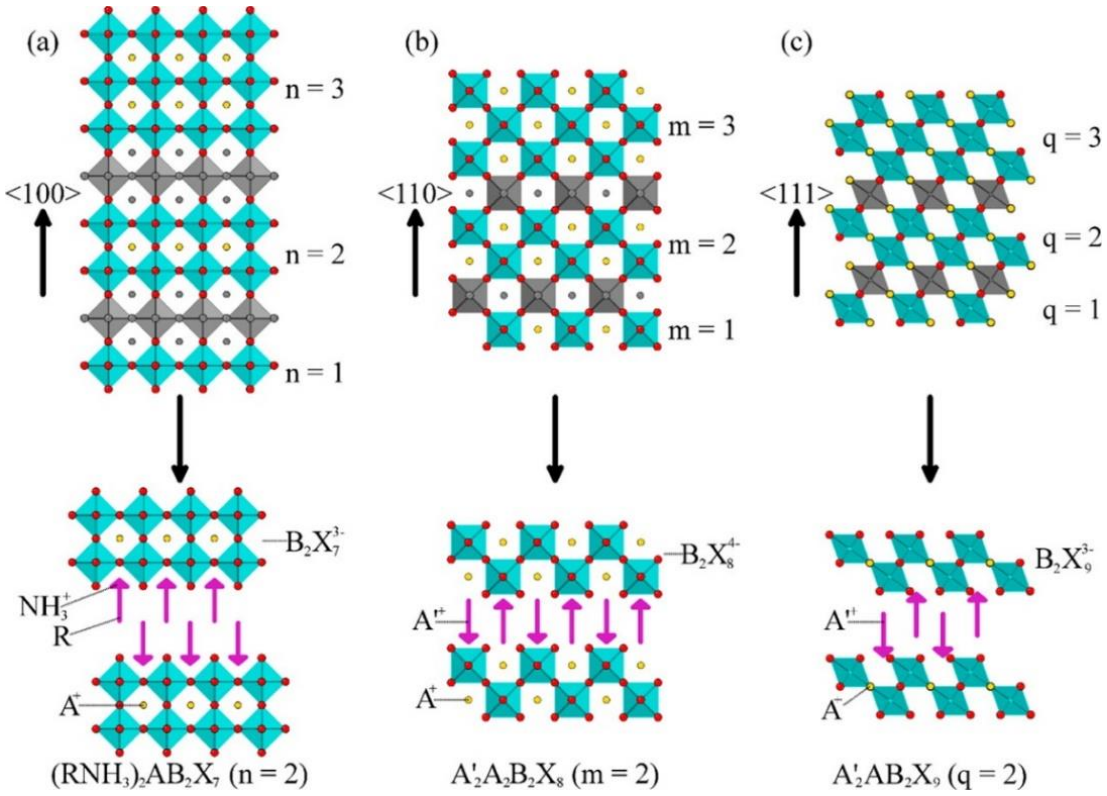

Figure 1-9 Schematic illustration of the lower dimensional HOIPs (lower sections) arising from different cuts of the 3D perovskite structure (top sections). (a) Cuts along the <100> direction of the 3D perovskites forming the family of ⟨100⟩-oriented layered perovskites with a general formula of $(RNH_3)_2A_{n-1}B_nX_{3n+1}$. (b) Cuts along the ⟨110⟩ direction forming the ⟨110⟩-oriented family, $A'_2A_mB_mX_{3m+2}$, which includes 1-D chain (m = 1) and 2-D layered (m > 1) members. (c) Cuts along the <111> direction forming the ⟨111⟩-oriented family, $A'_2A_{q-1}B_qX_{3q+3}$, featuring the 0-

D isolated cluster (q = 1) and 2-D layered (q > 1) members. In each low dimensional structure, the perovskite blocks are separated by a layer of organic cations. Reproduced from Mitzi *et al.*[104]

In the context of the recent emergence of hybrid perovskite solar cells, increasing attention has been drawn to the low dimensional perovskite-like materials due to their improved stability compared to 3D perovskites[105] and the emergence of lead-free perovskite-related systems.[85,106] Recently, layered perovskites have been reported in solar cells devices, demonstrating band gap tuning by changing the sizes of the cations and the dimensionality of the framework. For example, devices using the layered perovskites, $(PEA)_2(MA)_2(Pb_3I_{10})$ (band gap of 2.06 eV, PEA = phenylethylammonium) have achieved a power conversion efficiency of 4.73%,[107] and $(CH_3(CH_2)_3NH_3)_2(CH_3NH_3)_{n-1}Pb_nI_{3n+1}$ (n = 1, 2, 3, and 4) (from band gap of 1.52 eV for n = ∞ to 2.24 eV for n =1) leads to an efficiency of 4.03% for n=3.[108] In addition, the report of the first perovskite based LED, using the layered structure of $(C_6H_5C_2H_4NH_3)_2PbI_4$, has raised interest in the electroluminescent properties of low dimensional perovskites.[109,110] In comparison to the extensive studies starting a few decades ago on 2D layered halide perovskites for their potential applications in optoelectronic devices such as OLEDs and OFETs, there have been relatively few reports dealing with the 1D and 0D materials, with the focus mainly on their optical properties.

Figure 1-10 shows the band gaps and solar cell power conversion efficiencies of the low dimensional halide perovskites, including both lead halide and lead-free systems.[111,112] In general, the bandgaps of low dimensional perovskites are higher than 3D perovskites due to quantum confinement effects.[113] The dimensionality of the inorganic framework and the functionality of the organic cations lead to the unique properties of the halide HOIPs, such as photoconductivity, ionic conductivity, electrical conductivity, photo- and electroluminescence, exciton formation, and phase transitions.[66]

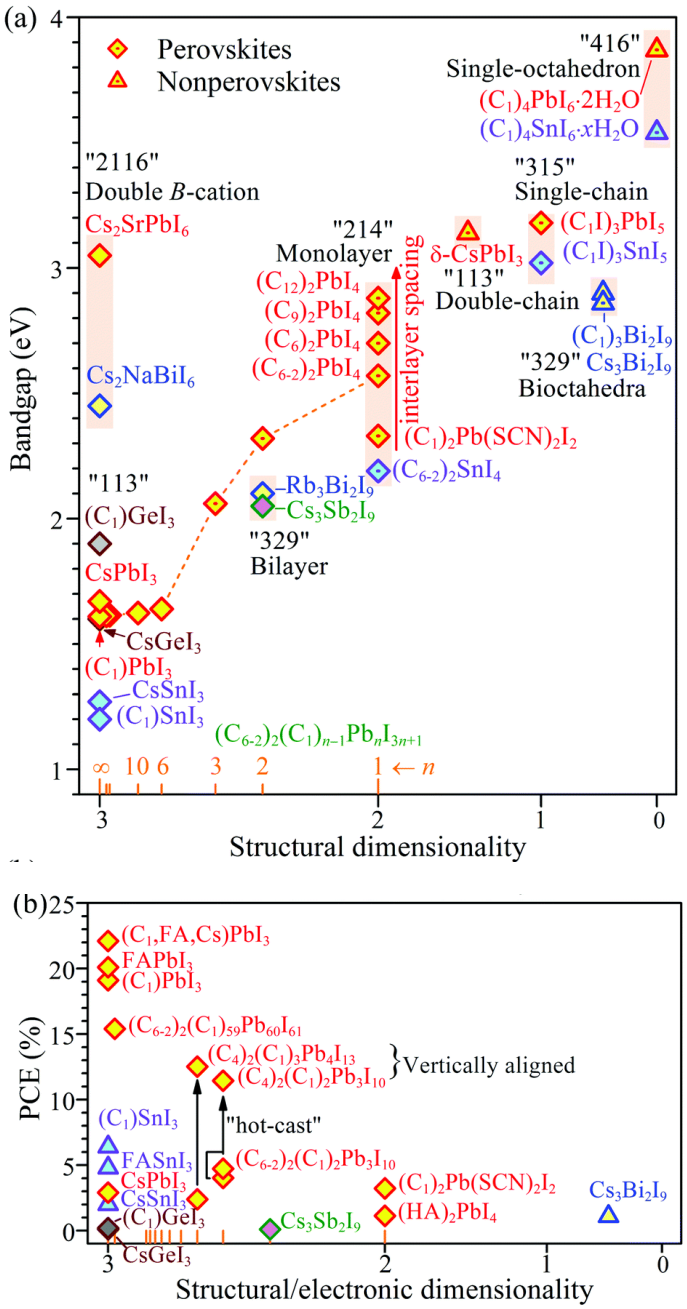

Figure 1-10 (a) Experimental optical bandgaps of 3D iodide perovskites (diamond symbols) and perovskite-related structures (triangle symbols) as a function of crystal dimensionality. (b) Highest recorded power conversion efficiencies for a number of absorption materials with 3D and low dimensional perovskite structures. Reproduced from Yan *et al.*[106]

1.4 Mechanical properties of HOIPs

1.4.1 Hybrid framework materials

Comprehensive studies concerning the mechanical behaviour of hybrid organic-inorganic frameworks started to emerge in 2006.[114,115] In order to examine their elastic and plastic responses under uniaxial pressure, the Young's moduli and hardnesses of a range of hybrid materials were determined.[116–118] The measurement of the mechanical response of organic-inorganic hybrid materials is challenging, since high quality single crystals and an understanding of the complex structure-mechanical relationship are required.[114,117] Therefore, the nanoindentation technique, wherein load and depth of penetration can be measured with a resolution of 1 nN and 0.2 nm, respectively, has been applied in a number of recent reports to facilitate the quantitative characterization of the mechanical properties of single crystals.[114,119] The measured mechanical properties can, in turn, aid understanding of the underlying structural and chemical characteristics of these hybrid materials.

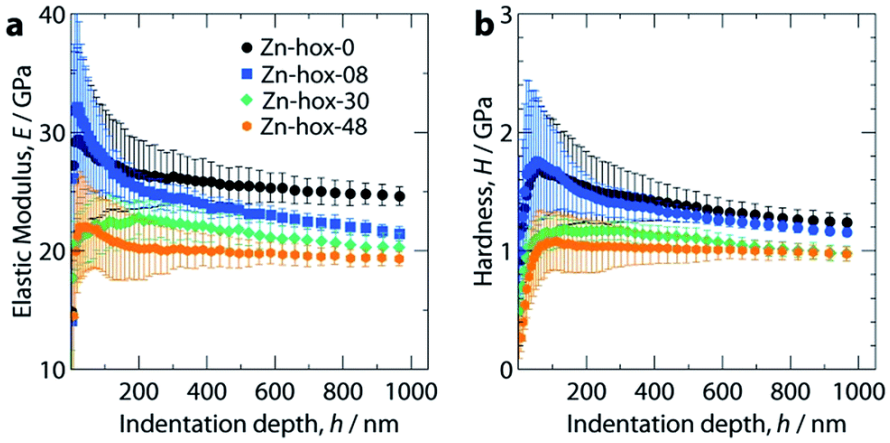

Figure 1-11 Elastic modulus (a) and hardness (b) of $[NH_3NH_2]_{1-x}$ $[NH_3OH]_x$ $Zn(HCOO)_3$, where x = 0, 0.08, 0.30 and 0.48, labelled Zn-hox-0, Zn-hox-08, Zn-hox-30 and Zn-hox-48 respectively. Reproduced from Cheetham *et al.*[13]

For example, a recent study on the amine formate perovskites, $[AmineH^+][Mn(HCOO)_3]$, (Amine= $HNC(NH_2)_2$, $(CH_2)_3NH_2$ and $(CH_3)_2NH_2$) used both X-ray diffraction and nanoindentation.[120,121] The results showed that the elastic modulus is closely linked to

hydrogen bonding energy. Figure 1-11 illustrates the tunable mechanical properties of hydroxylammonium/hydrazinium zinc formate perovskites, $[NH_3NH_2]_{1-x}$ $[NH_3OH]_x$ $Zn(HCOO)_3$. Doping of hydroxylammonium into the hydrazinium framework leads to a decrease in hydrogen bonding, and hence reduced stiffness and hardness.[13]

Using the classification tool of Ashby diagrams,[122] the mechanical properties of hybrid frameworks are summarized in Figure 1-12. Although there were no experimental reports with similar techniques on the mechanical properties of hybrid halide perovskites (halide HOIPs) at the time, mechanical properties of formate HOIPs have recently been studied and marked as ABX_3 hybrids in Figure 1-12.

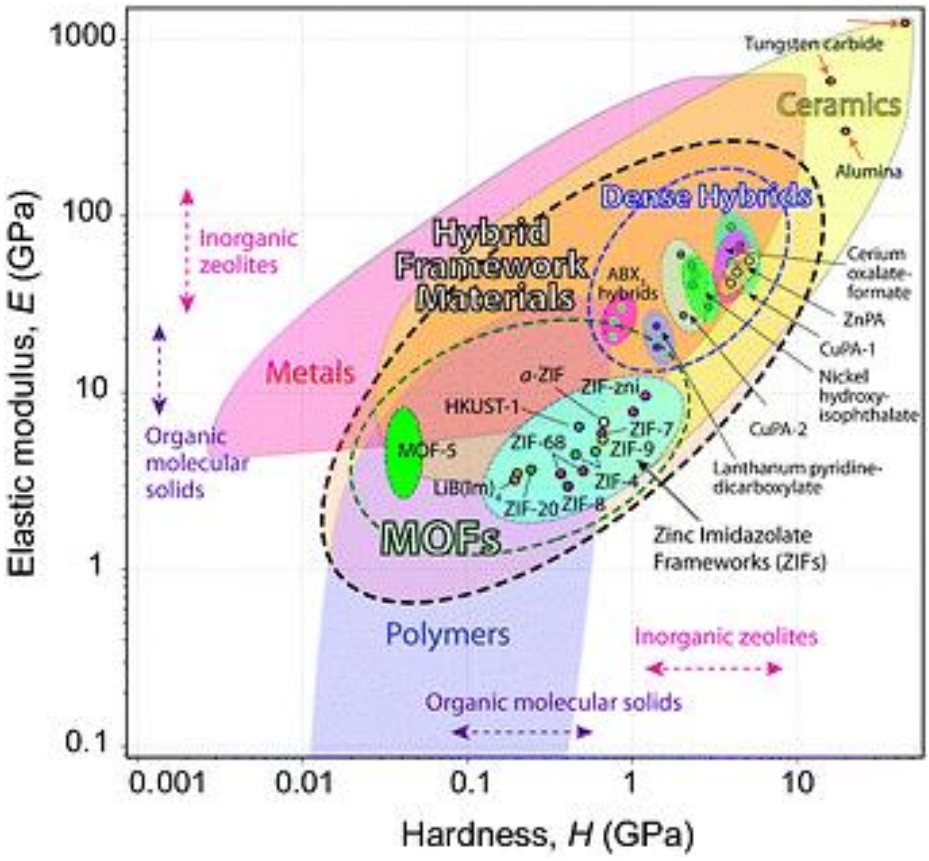

Figure 1-12 Elastic modulus versus hardness materials property map for hybrid framework materials, Reproduced from Cheetham *et al.*[114]

1.4.2 Hybrid halide perovskites

Considering the mechanical properties of the hybrid halide perovskites, there is concern that their application in devices may be limited by their lack of robustness compared to

inorganic materials.[57] In particular, the stress state and the crystallinity of the perovskite-layer have a strong impact on absorption performance.[123] On the other hand, the soft and ductile nature of the halide HOIPs provides the potential for applications in flexible and wearable devices, [124,125] such as the perovskite-based flexible memory device shown in Figure 1-13. It is therefore important to understand the mechanical stability of the halide HOIPs.

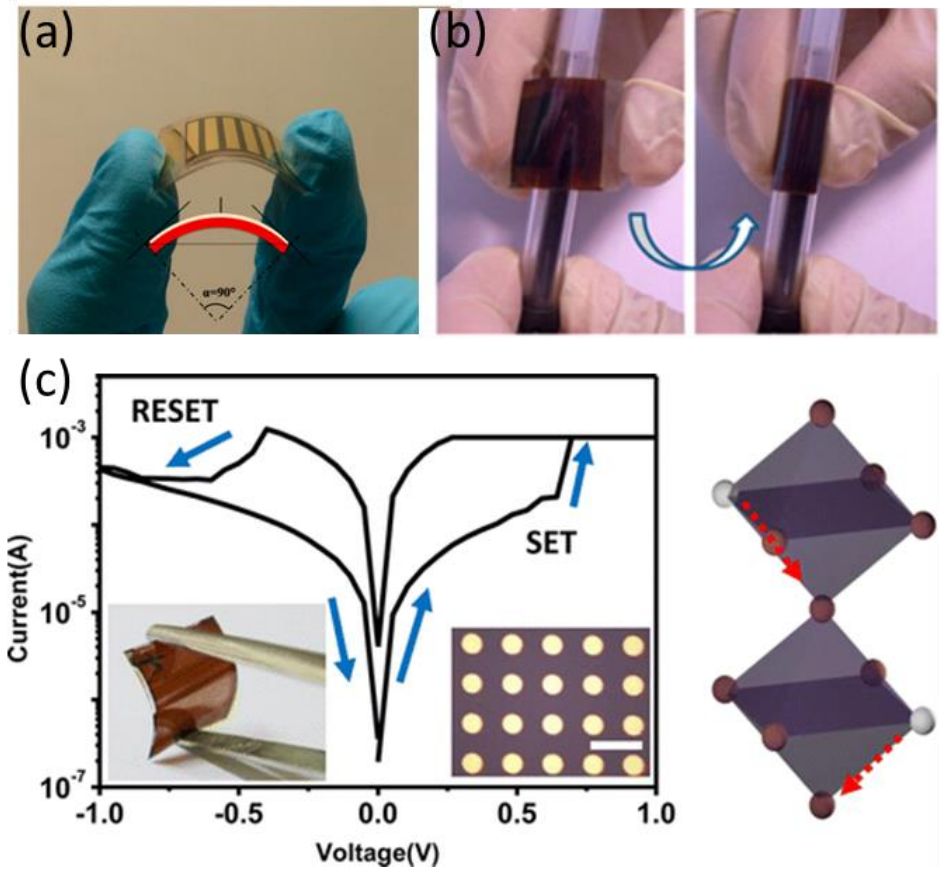

Figure 1-13 Photograph of $MAPbI_3$ based (a) perovskite solar-cell-based flexible glass,[125] and (b) flexible solar cell around one pen with a diameter of 1 cm.[126] (c) Current–Voltage characteristics of flexible $MAPbI_3$ resistive switching memory devices, without and with bending stress (a bending radius of 1.5 cm).[127]

In terms of the mechanical response under volumetric pressure, several studies of the hydrostatic deformation of hybrid halide perovskites including MA and FA lead halide perovskites, have recently been reported, showing phase transitions to lower symmetries due to octahedral tilting of the inorganic framework at pressures less than 1 GPa, resulting in bandgap shifts as the pressures increase. Further increases in pressure lead to amorphization (see Chapter 3.1 for more details).[61,128–130] It is now established that the

lead halide framework is highly dynamic, showing good structural and mechanical flexibility.[131]

Regarding mechanical response under uniaxial pressure, on the other hand, Feng *et al*. reported first-principles calculations on the structural, elastic and anisotropic properties of the lead and tin based bromide and iodide systems.[123] In the present work, Chapter 5 further addresses the measurement of mechanical properties of perovskites and double perovskites. In this case, the elastic modulus and hardness are used to measure the strength and robustness of a framework respectively, and hence they are of interest both for the understanding of the intrinsic properties of the materials and the evaluation of materials behaviour under stress during the processing step of device production.

Chapter 2 Methods

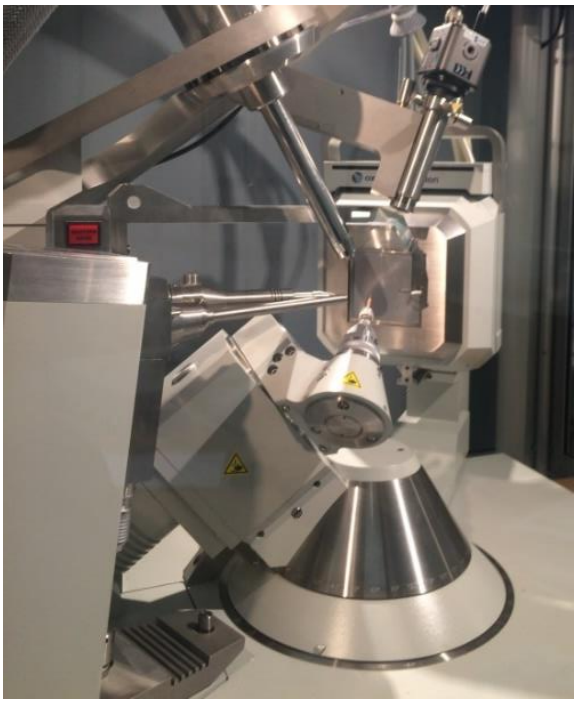

This chapter gives an account of the experimental methods used in this research. First, the synthesis of eight Pb-based, as well as five Bi-based perovskite and related structures, is summarized. The synthesised materials are characterized by a range of techniques and explored by computational studies. The principles and practice of X-ray diffraction used for structural examination and the methodology of the nanoindentation technique used for probing mechanical properties are explained in detail.

2.1 Materials synthesis

2.1.1 Crystallization

2.1.1.1 MA/FAPbX_3 (X = I, Br or Cl)

Microcrystals (< 1 mm) of $MAPbBr_3$ and $FAPbBr_3$ were synthesized by crystallisation on cooling. Homogeneous mixture of 0.104 g formamidine acetate ($HN{=}CHNH_2 \cdot CH_3COOH$) and 0.367 g lead bromide ($PbBr_2$) were put into a 5 ml glass vial, then 0.3 ml hydrobromic (HBr) solution (48wt% in H_2O) was added. The mixture immediately turned red, and single-phase powder product was obtained after stirring the mixture for 1 hour at room temperature. Similar procedures were applied for synthesis of $MAPbBr_3$ with 0.112 g MABr and 0.367 g $PbBr_2$. In order to get single crystals suitable for single crystal X-ray diffraction (0.2 – 0.4 mm), $PbBr_2$ was fully dissolved in HBr solution at 80°C, then a second HBr solution containing a stoichiometric amount of FA acetate (or MABr) was added while stirring on a hotplate, the mixture was slowly cooled to room temperature, and red octahedral single crystals precipitated out. When using lead acetate instead of $PbBr_2$, excess HBr acid was added to avoid secondary phase formation. The synthesis of microcrystals was carried out by Dr. Fengxia Wei and the author, and the crystals were used for the research in Chapter 4.

Single crystals (~ 2 mm) of $MAPbX_3$ (X = I, Br or Cl) were precipitated from hydrochloric, hydrodrobromic and hydroiodic acid solutions following the method of Poglitsch et. al.[53] In this procedure, 2.5 g lead(II) acetate was dissolved in 10 ml of concentrated aqueous HCl (37 wt%)/HBr (48 wt%)/HI (57 wt%) and heated to above 90°C. To this solution, 2 ml of concentrated HX (X = I, Br and Cl) was added together with 0.597 g of CH_3NH_2 (40 wt% aqueous solution, Merck). Crystals were obtained by cooling the solutions from ~ 90°C to 25°C over 72 hours. The products were colourless for the chloride, orange for the bromide and black for the iodide. For $MAPbI_3$, the crystals were separated at above 40°C to avoid the formation of yellow crystalline $(CH_3NH_3)_4PbI_6 \cdot 2H_2O$.[132] The crystals were prepared by Dr. Yanan Fang (Department of Materials and Engineering, Nanyang Technological University of Singapore) and used in Chapter 5.

Single crystals (~3 mm) of $FAPbX_3$ (X = Br or I) were synthesized using inverse temperature crystallisation. Attempts at producing $FAPbCl_3$ yield a two-dimensional layered complex, since the FA cation is too large to fit into the lead chloride perovskite framework.

$FAPbI_3$: 1 M of $FAPbI_3$ solution was prepared in γ-butyrolactone. The solution was filtered into a vial by using a PTFE filter with a pore size of 0.2 μm. The filtrate was then immersed in a silicon oil bath, which was pre-heated to 90 °C. The temperature of the system was slowly increased to 100 °C. Several black $FAPbI_3$ single crystals were collected at this temperature. The solution was then dissolved, filtered, and then immersed again in a silicon oil bath at 90 °C. The resulting single crystals were used as seeds by gently placing them into the perovskite solution. Then, the temperature of the system was gradually increased by 1 °C in every 30 minutes to further increase the crystal size.

$FAPbBr_3$: 1 M of $FAPbBr_3$ was dissolved in a 1/1 (v/v) solution of DMF and GBL. The solution was filtered into a vial, and then the filtrate was immersed in a silicon oil bath at 50 °C. The temperature was slowly increased to 60 °C to initiate the nucleation process. Then, the temperature was gradually increased by 1 °C in every 30 minutes to further enhance growth of the orange single crystals. The FA-based single crystals were prepared by Furkan Isikgor (Department of Materials and Engineering, National University of Singapore).[133] and the crystals were used in Chapter 3 and Chapter 5.

2.1.1.2 GUA_xPbI_{2+x} (x = 1, 2, or 3)

One of the precursors, guanidinium (GuA) iodide ($C(NH_2)_3I$) was firstly prepared by adding equal molar of guanidinium carbonate (8.03 g) to hydriodic acid (HI) (20 g, aqueous solution, 57 wt%). A white solid was obtained after removing water at 50 ^oC using a rotational evaporator. The product was stored in an argon glove box for future use.

Three single crystal phases of of guanidinium iodoplumbates were produced by tuning the concentration of HI. The solution synthesis was followed using the methods described by Poglitsch and Weber[53] and adapted from the synthetic procedures by Kanatzidis *et. al*.[66] Lead acetate trihydrate (379 mg, 1 mmol) was added to the flask and dissolved in HI upon heating the flask to 120 ^oC. An oil bath is used to provide heating with constant

magnetic stirring. Stoichiometric ratios of solid $C(NH_2)_3I$ (1 mmol, 2 mmol and 3 mmols respectively) were added. The solution was then left to cool to 50 ^oC without stirring. Yellow precipitates were formed upon cooling. The resulting crystals were used in the research of Chapter 6.

2.1.1.3 $A_3Bi_2I_9$ (A = NH_4 or MA)

Single crystals of $(NH_4)_3Bi_2I_9$ and $MA_3Bi_2I_9$ were prepared by solution methods. 1 mmol of bismuth iodide (Sigma-Aldrich) was dissolved in 0.3 mL of hydroiodic acid (57% aqueous solution) by heating in an oil bath. At 90 °C, a stoichiometric amount of NH_4I (or MAI) was added to the solution and the mixture was then held for 3 hours at this temperature. Dark red crystals were then filtered out without allowing the solution to cool to room temperature. The crystals were dried under vacuum overnight. Red fine powder could be obtained by grinding at room temperature. The resulting crystals were used in the research in Chapter 6.

2.1.2 Hydrothermal synthesis

Single crystals (~0.5 mm) of double perovskites were synthesized by Dr. Fengxia Wei and used in the research in Chapter 7.

2.1.2.1 $(MA)_2MBiBr_6$ (M=Ag or Tl)

The starting material, MABr, was prepared by mixing stoichiometric amounts of methylamine solution (40wt% in H_2O) and HBr (48wt% in H_2O) in an ice bath, then heating at 333K to dryness, washing with acetone, followed by drying overnight in a vacuum oven. $(MA)_2AgBiBr_6$ was synthesized by adding $AgNO_3$ to KBr solution in H_2O, the precipitates were filtered out, washed with acetone and dried in air. $(MA)_2TlBiBr_6$ was synthesized by the hydrothermal method at 150 °C using 3 mmol MABr, 1.5 mmol $(CH_3COO)Tl$, and 1.5 mmol $BiBr_3$ in 1 ml HBr. The product was a mixture containing significant quantities of yellowish $(MA)_2Bi_3Br_9$.

2.1.2.2 $(MA)_2KBiCl_6$

The starting material, MACl, was prepared by mixing stoichiometric amounts of methylamine solution (40 wt% in H_2O) and HCl (37% in H_2O) at 273 K, then heating at 333 K to dryness, washing with acetone, and drying overnight in a vacuum oven. Crystals of $(MA)_2KBiCl_6$ were synthesised at 423 K by the hydrothermal method in a stainless-steel Parr autoclave using 2.4 mmol MACl, 1.2 mmol KCl and 1.2 mmol $BiCl_3$ in 1 ml HCl acid solution.

2.2 Structural characterization

2.2.1 Single crystal X-ray diffraction (SCXRD)

2.2.1.1 Principle of methods

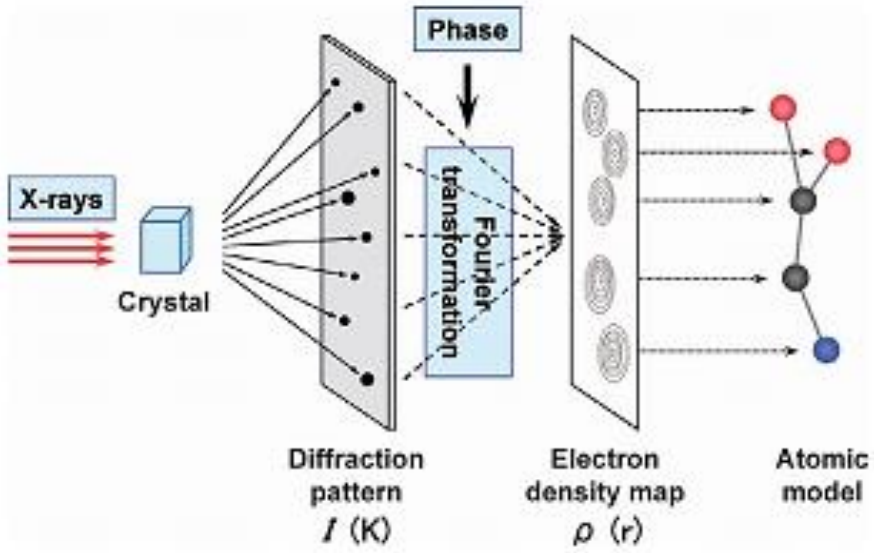

Figure 2-1 Schematic illustration of the SCXRD technique.

Single crystal X-ray diffraction has been used to determine the crystal structure of materials since the early 20th century. The technique allows one to obtain the cell parameters, space group and precise atomic positions. X-ray diffractometers consist of three basic components, an X-ray tube, a goniometer, and a detector. By heating a filament, electrons are produced and X-rays are generated in a cathode ray tube, accelerating the electrons toward a target under applied voltage. The interaction between

the atoms in the crystal and the X-rays results in the formation of a diffraction pattern (Figure 2-1). The diffraction patterns consist of the superposition of scattered waves with varying amplitudes and phases associated with the structure factor, *F (K)*. The intensity *I (K)* of a reflection can be related to the structure factor. [134]

$$|F\ (K)|^2 \propto I\ (K)$$

$$F\ (K) = \int_v \rho\ (r) exp\{2\pi i(K.r)\} dv_r$$

where *K* is the scattering vector and *r* refers to real space position. Electron density, ρ, can then be calculated by reverse Fourier transformation:

$$\rho\ (r) = \frac{1}{V}\int_v F\ (K) exp\{-2\pi i(K.r)\} dv_K$$

2.2.1.2 Instruments and data analysis

Laboratory single crystal X-ray diffraction measurements were performed on an Oxford Diffraction Gemini E Ultra diffractometer with an Eos CCD detector using Mo Kα radiation (λ = 0.7107 Å, operating at 50 kV and 40 mA). Crystals were mounted on a cryoloop using perfluorinated oil. Data were collected using ω scans at temperatures of 100 K – 450 K in a nitrogen stream. Data collection and reduction were performed with CrysAlisPro (Version 1.171.34i, Agilent Technologies). Absorption corrections were applied using analytical methods with face indexing or spherical methods to best suit the crystal shape. The structures were solved with ShelXT and refined with ShelXL-97.[135,136] Using the OLEX^2 platform,[137] all non-hydrogen atoms were refined anisotropically, but the electron density of hydrogen atoms were not able to be determined in the presence of heavy atoms (e.g. Pb, Bi, Br, I) in our samples.

2.2.2 Powder X-ray diffraction (PXRD)

2.2.2.1 Principle of methods

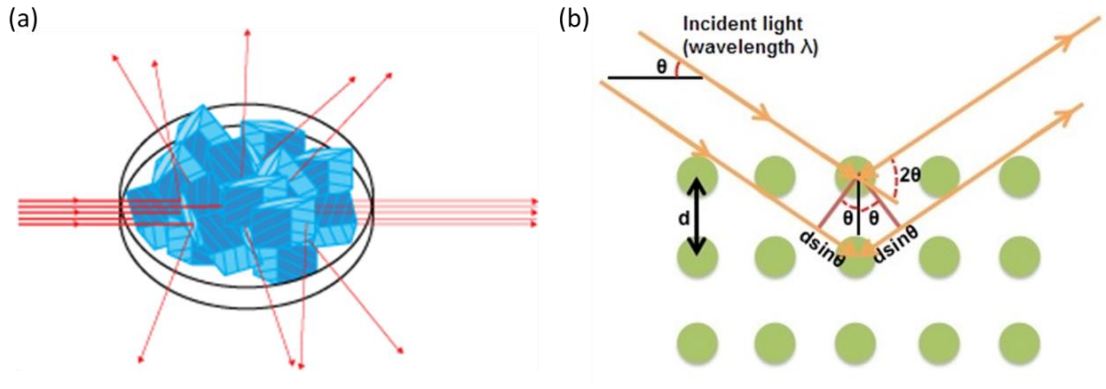

Figure 2-2 Schematic illustration of (a) diffraction of powder sample with a steady X-ray source and (b) lattice diffraction satisfying the Bragg's law.

The PXRD technique is commonly applied for phase identification and to confirm the bulk structure. Diffraction is determined by Bragg's law (Figure 2-2):

$$n\lambda = 2dsin\theta$$

where d is the spacing between diffracting planes, θ is the incident angle, λ is the incident wavelength of the beam and n is an integer. The Bragg equation relates the interplanar spacing, d, to the diffraction angle and the analysis treats X-rays like visible light being reflected by a surface, with the X-rays being reflected at lattice planes following the Bragg equation.[138]

2.2.2.2 Instruments and structure refinement

With Cu Kα X-rays ($\lambda_{average}$ = 1.54187Å), a Bruker D8 Advance theta/theta (i.e. fixed sample) diffractometer with position sensitive detector (LynxEye EX) was used for laboratory PXRD measurement (best instrumental resolution ~ 0.06° in 2θ and ~ 0.03° in omega) (See Appendix, Figure-A 1 for instrumental peak widths). For the $MAPbBr_3$ and $FAPbBr_3$ samples studied in Chapter 4, the powder patterns were collected from 2θ 10 - 135° using a step size of 0.02° with an exposure time of 1.5 s per step. Rietveld refinement of the diffraction patterns was applied with TOPAS V5.1 using the fundamental parameters approach and a full axial divergence model.[139,140] In Rietveld refinement,

parameters in the model such as atomic positions and lattice parameters, as well as experimental factors that affect peak profile, such as peak position, shape and widths, and the background are refined using a least-squares approach, until the agreement between the calculated and measured diffraction profiles is optimized.[138]

For the phase identification of Bi-based perovskites in Chapter 6, room temperature PXRD data were collected over a 2θ range of 10-50° using a Bruker D8 theta/theta (ie fixed sample) with a position sensitive detector (LynxEye) and a standard detector with auto-absorber, a graphite monochromator and sample rotation. The instrument has a best instrumental resolution of ~0.08° in 2θ and ~0.04° in omega.

2.2.3 Synchrotron X-ray diffraction

Synchrotron sources allow us to probe the atomic structure with much higher resolution than with laboratory diffractometers. The synchrotron facilities used in this research were the PXRD beamline I11 and the SCXRD beamline I19 at Diamond Light Source. Oxfordshire, UK.

2.2.3.1 Powder diffraction

Samples of finely ground $FAPbBr_3$ were coated on 0.3 mm glass capillaries by using cream to ensure a thin coating of the powder, thereby minimising absorption effects. The position sensitive detector Mythen strip was used with a mean X-ray wavelength of 0.82609(1) Å, calibrated using a NIST Si 640c standard.[141] Data were collected at 290 K over the range 2θ 2° - 92° in the Debye-Scherrer geometry with the monochromatic synchrotron X-ray radiation (15 keV) (Figure 2-3).

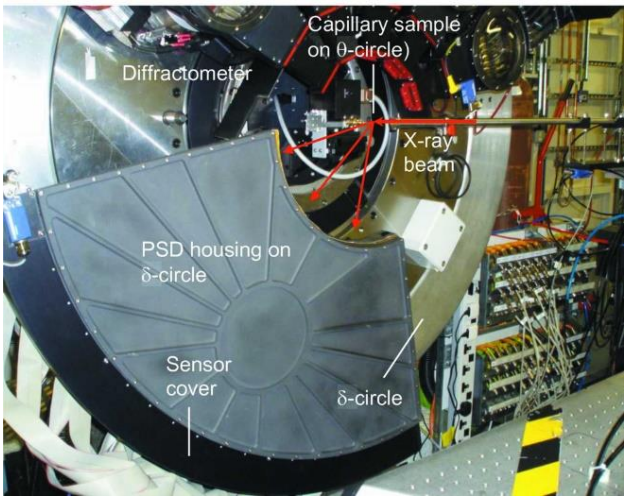

Figure 2-3 Photograph of the PSD detector at I11.Reproduced from Tang *et al.*[141]

2.2.3.2 High pressure single crystal diffraction

High-pressure single crystal diffraction experiments were performed using a diamond anvil cell setup (Figure 2-4) at the Diamond Light Source (I19, λ = 0.4895 Å), with Fluorinert FC-70 as an inert pressure transmitting medium. The fluorescence of ruby was used for pressure calibration. The diffractometer consists of three main part: the crystal logic goniometer, a Rigaku Saturn 724+ detector and a Rigaku ACTOR robotic sample changer.[142] Before the experiment, a $FAPbI_3$ single crystal (~150 µm) was mounted in the diamond anvil cell and data was collected at ambient pressure, 0.247 GPa, 0.494 GPa and 0.742 GPa, respectively.

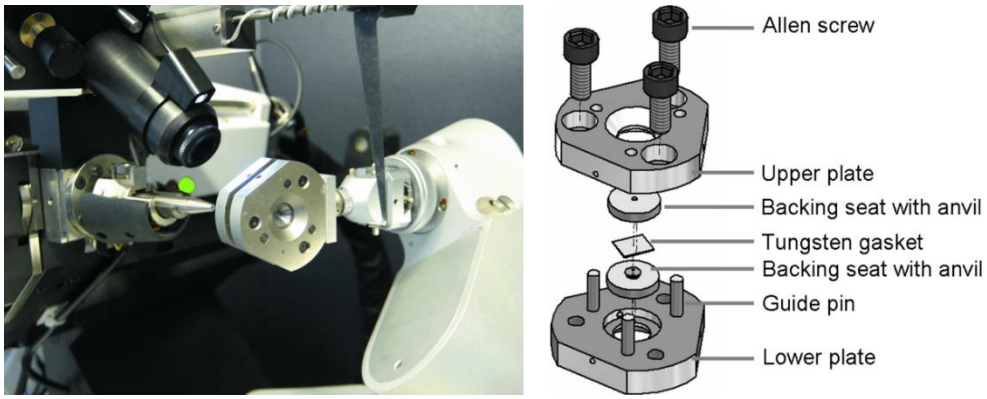

Figure 2-4 Merrill–Bassett diamond anvil cell mounted on a Bruker Kappa APEX II diffractometer and (right) an exploded view of a Merrill–Bassett diamond anvil cell. Reproduced from Warren *et al.*[143]

2.3 Nanoindentation

2.3.1 Sample preparation

Prior to nanoindentation, individual untwinned crystals with well-defined shapes were selected and face indexed using single crystal X-ray diffraction. The X-ray diffraction patterns were collected on an Oxford Diffraction Gemini Ultra diffractometer with graphite monochromated Mo K_α radiation (λ= 0.71073 Å) at room temperature and the structures were solved with CrysAlis^{Pro} using the program SHELX.[144] The program Olex2 was used as an interface for the SHELXS and SHELXL executables.[136]

The crystals were then glued on to small flat aluminum chips using a thin layer of cyanoacrylate glue, with the facets of interests in contact with the aluminum chips. The samples were then firmly cold-mounted using Epofix resin (Struers Ltd.) and ground to remove the chips, followed by careful polishing using increasingly fine diamond suspensions.[33] A diamond suspension with a particle size of 0.25 μm was used in the final step to minimise the surface roughness.

2.3.2 Instrument and methods

Nanoindentation experiments were performed at room temperature using an MTS NanoIndenter® XP (MTS Corp., Eden Prairie, MN), with the indenter aligned normal to the facets of interests (Figure 2-5).[114] A fused silica standard, with an elastic modulus of 72 GPa and hardness of 9 GPa, was used for calibration and the instrument was kept in an isolation cabinet to minimise thermal instability and acoustic interference.

Applying the continuous stiffness measurement (CSM) mode, indentation experiments were conducted using a pyramidal sharp Berkovich tip (radius ~100 nm) and were controlled by displacement with a strain rate of 0.05 s^{-1}. The load (P) and the displacement (h) were monitored continuously, until a maximum displacement of 1000 nm was reached, at which point the indenter was held for 30 s before unloading at the same strain rate.

In order to determine the Young's modulus and hardness of the crystals, *P* was plotted as a function of indentation depth, and the elastic contact stiffness, *S*, was determined by *dP*/*dh*. Using the standard Oliver-Pharr Method,[145,146] the reduced modulus, E_r, was obtained by:

$$E_r = \frac{\sqrt{\pi}}{2\beta}\frac{S}{\sqrt{A_c}}$$

where A_c is the contact area under load based on the calibrated tip function and β is a constant that depends on the geometry of the indenter (for a Berkovich tip β = 1.034). The anisotropic elastic moduli along different crystal facets were then according to:

$$\frac{1}{E_r} = \frac{1-\nu_i^{\,2}}{E_i} + \frac{1-\nu_s^{\,2}}{E_s}$$

where ν and E are Poisson's ratio and elastic modulus, respectively, and the subscripts *i* and *s* refer to the indenter and the sample respectively. The diamond indenter used in this thesis has an elastic modulus of 1141 GPa and a Poisson's ratio of 0.07. The elastic moduli of the sample determined in the three orthogonal orientations were calculated assuming a Poisson's ratio of the sample of 0.3.

As a measure of materials' ability to resist local plastic deformation, indentation hardness (*H*) is determined by: [146]

$$H = \frac{P_{\max}}{A_c}$$

Where $P_{\max}$ is the maximum indentation load and A_c is the contact area between the indenter tip and the sample. In this case, A_c is calculated from the contact depth, h_c, governed by the following equation: [145]

$$h_c = h_{\max} - 0.75\frac{P_{\max}}{S}$$

Where $P_{\max}$ refers to the maximum indentation depth and the extent of elastic recovery is represented by $0.75(P_{max}/S)$.

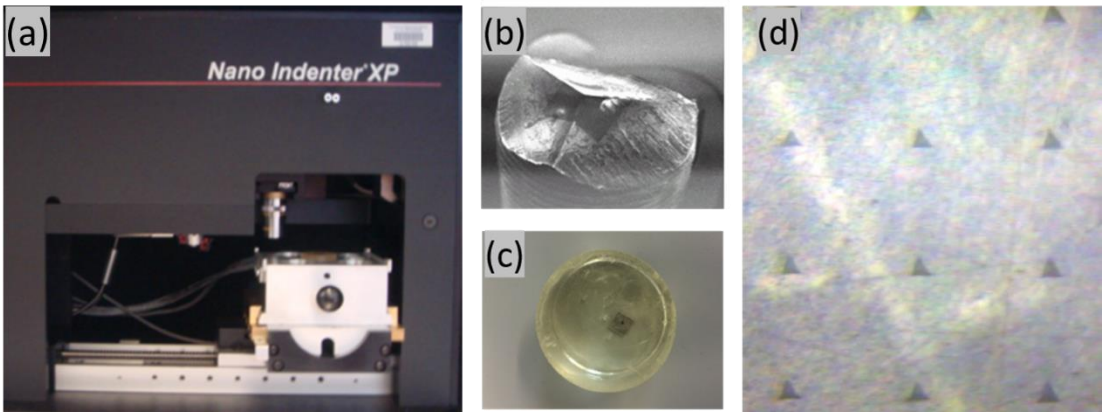

Figure 2-5 Photographs of (a) the MTS nano indenter, (b) the Berkovich tip, (c) a crystal mounted in the resin before polishing and (d) an array of indents conducted on the (100) surface of $MAPbBr_3$.

2.4 Computational methods

2.4.1 DFT calculations

2.4.1.1 Electronic structures

For the Pb-based halide perovskites and double perovskites, DFT calculations were performed using the VASP code.[147] Projected augmented wave (PAW)[148] potentials were used for Pb ($5d^{10}6s^26p^2$) and I ($5s^25p^5$), and PBE functional[149] was used to model the exchange-correlation. A planewave kinetic energy cutoff of 500 eV was used for all calculations. For the density of states (DOS), a $10 \times 10 \times 12$ K-point mesh was used for DOS calculation instead. Relativistic spin-orbit coupling (SOC) is important in the lead system and was considered for both band structure and DOS calculation.[150] Because the electronic structure near the band gap mostly depends on inorganic elements, i.e. Pb and I (or Br), the experimental lattice parameters and ionic positions of Pb and I (or Br) were fixed throughout the calculations, and the organic cations were replaced by the background charges to get rid of the disorder.

The electronic band structure and DOS were calculated using the experimental inorganic framework of $FAPbI_3$ at different pressures: 0 GPa, 0.247 GPa, 0.494 GPa and 0.741 GPa structure, respectively and at different temperatures: 250 K and 200 K. DFT was also

used to calculate electronic band structures and projected DOS of $FAPbBr_3$ at 120 K and 300 K. The above DFT calculations were performed by Zeyu Deng in the author's department.

For the Bi-based layered perovskite, $(NH4)_3Bi_2I_9$, the DFT calculations employed the generalised gradient approximation (GGA) implemented with PAW[148,151] pseudopotentials as supplied in the Vienna *ab initio* Simulation Package (VASP).[147,152–154] The effect of spin-orbit coupling was only included during band structure and density of states calculations. The effects of van der Waals dispersion interactions were included during structural and electronic relaxation.[155] The following parameters were adopted: (i) a 3×5×2 Monkhorst-Pack k-point mesh[156] and (ii) a 500 eV plane-wave cutoff energy. The numbers of valence electrons treated explicitly were as follows: 15 for Bi ($5d^{10}6s^26p^3$), 7 for I ($5s^25p^5$), 6 for O ($2s^22p^4$), 5 for N ($2s^22p^3$), and 1 for H ($1s^1$). All structural relaxations were performed with a Gaussian broadening of 0.05 eV.[157] The ions were relaxed until the forces on them were less than 0.01 $eV \cdot A^{-1}$. This DFT calculation was performed by Dr. Jung-Hoon Lee in the author's department.

2.4.1.2 Cation dynamics

The presence of the organic cations in HOIPs results in a complex potential energy surface (PES) with many shallow local minima. We exploit this aspect to partially explore the dependence on the PES on the initial orientations of the cation in Chapter 4. We considered an ideal cubic cage with different orientations of the FA cation obtained rotating the molecule along two of the main axes of the molecule. In particular we focused on the rotation along the axis parallel to the N-N line that passes on the C atom. This axis is particular interesting because it does not change significantly the distance between the H group and the halide.

The different orientation of the molecule induces different tiltings of the inorganic cage with a consequent variation in the inter-planes distance along different crystallographic directions. The deviation (σ) is obtained as the square root of the variance of the inter-planar distance with respect to the experimental observed cubic structure according to:

$$\sigma^2 = \left(\sum \frac{(\mathrm{d} - d_0)^2}{N}\right)$$

where d is the interplanar distance at local minima, d_0 is the interplanar distance of an ideal cubic perovskite structure and N is the multiplicity of the planes in cubic symmetry.

The calculations have been performed with the code VASP using a plane wave basis set with a 700 eV cut-off and 6x6x6 k-points grid. The geometry optimization has been performed to reduce the forces below a threshold of 1 mev. This calculation was performed by Dr. Federico Brivio in the author's department.

2.4.2 Ab initio molecular dynamics (AIMD)

AIMD calculations were performed using PAW pseudopotentials[148,151] as implemented in the VASP code[147,154], with the following electrons treated explicitly: H ($1s^1$), C ($2s^2 2p^2$), N ($2s^2 2p^3$), Pb ($5d^{10} 6s^2 6p^2$) and Br ($4s^2 4p^5$). A 400 eV planewave kinetic energy cutoff and gamma point K-point mesh were used throughout the calculations. Van der Waals interactions were included[158]. SOC was not considered for the AIMD since it does not affect structural properties significantly.[159] An NVT ensemble (canonical ensemble) was used and the experimental lattice parameters were applied and kept fixed ($2 \times 2 \times 2$ supercell).

For the tetragonal $FAPbI_3$ structure at 200 K (Chapter 3), the experimental lattice parameters and positions of the inorganic elements (Pb and I) were all kept fixed during the simulations which were first performed for 10 ps to equilibrate the structure and then these data were discarded. Following this a further simulation of 50 ps was performed to collect data for analysis. The trajectories were sampled every 10 fs to determine the preferred orientations of the FA ion.

For the room temperature structures of $MA/FAPbBr_3$ (Chapter 6), the temperature was set at 300 K. The data from the first 10 ps was discarded for equilibrium and then we ran calculations for 100 ps for data collection. The radial distribution function (RDF) was analysed using VMD[160] with a bin size of 0.05 Å. The AIMD calculations were performed by Zeyu Deng in the author's department.

2.5 Other characterization

2.5.1 UV-visible spectrometry

Reflectance measurements were carried out using a PerkinElmer Lambda 750 UV-Visible spectrometer. Measurement was carried out in the reflectance mode with a 2 nm slit width. The scan interval was 1 nm and the scan range covered the absorption edge. The sample used was ground into fine powder with a particle size of ~10 μm, and pressed to a pellet thickness of ~1 mm to satisfy the sample requirement for Kubelka-Munk theory, i.e. particle sizes must be much smaller than sample thickness to avoid geometrical effect. Reflectance data were converted to absorbance spectrum by the Kubelka-Munk equation:

$$F(R) = \frac{A}{S} = \frac{(1-R)^2}{2R}$$

where *A* and *S* are the absorption and scattering coefficients, respectively, and *R* is the reflectance. *S* is assumed to be constant with wavelength for the same sample conditions, i.e. particle size, sample thickness and moisture, which can be controlled during data collection.[161] A Tauc plot of $(h\nu A)^2$ against hν was carried out and the linear part was fitted and extrapolated to zero to obtain the band gap value, where *h* is Plank constant and *v* is the frequency of the photon.[162] The measurements were conducted by Fei Xie and the author.

2.5.2 Thermal analysis

Thermogravimetric analysis (TGA) was carried out under a continuous nitrogen flow using a TA Instruments Q-500 series thermal gravimetric analyser between 25 and 800 °C.

2.5.3 Impedance spectrometry

The conductivities were measured using the single crystal conductivity method.[163–165] In brief, single crystal samples were filtered and dried in a vacuum oven overnight. The dried crystals were mounted on two Au microelectrodes which were designed to have a

20 micro meter gap by lithography. The electrode was placed in a dark chamber with dry nitrogen flow. The conductivities were measured by the AC impedance method using a Gamry Interface electrochemical instrument at 10 mV amplitude from 1 MHz to 0.1 Hz at 20°C. We also performed powder conductivity measurements on a pellet sample. The pellet was formed at 0.1 GPa from dry powder, and then, before measuring conductivities, the pellet was kept in dry nitrogen for a week in order to remove adsorbed water which can cause ionic conduction, probably due to hydrated interparticle spaces.[163] The conductivity measurements were conducted by Dr. Satoshi Tominaka.

Chapter 3 Crystal chemistry of formamidinium lead halide perovskites

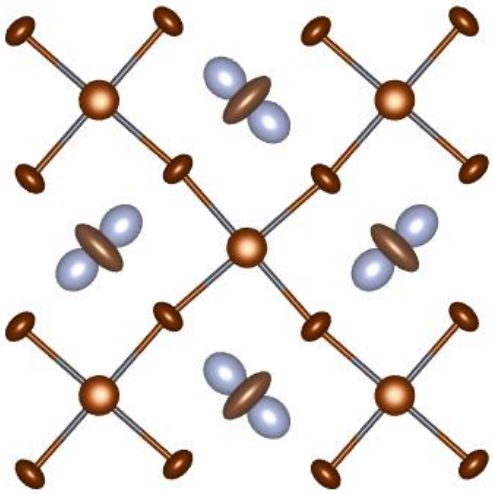

This chapter describes the crystal chemistry of FA-based hybrid perovskites. Variable temperature X-ray diffraction was applied to study the phase transition of $FAPbI_3$ and $FAPbBr_3$ single crystals. The low temperature dynamics of the FA cations were studied with both experimental and computational approaches. In addition, high pressure X-ray diffraction was employed to study the phase stability of single crystal $FAPbI_3$ under hydrostatic pressure and density functional theory (DFT) calculations were carried out to examine the effects of external stimuli on band structures.

Some of the results in this chapter have been published in:

- **S. Sun**, Z. Deng, Y. Wu, F. Wei, F. H. Isikgor, F. Brivio, M. W. Gaultois, J. Ouyang, P. D. Bristowe, A. K. Cheetham and G. Kieslich, "Variable temperature and high-pressure crystal chemistry of perovskite formamidinium lead iodide: a single crystal X-ray diffraction and computational study", *Chem. Comm.,* 2017, 017, **53**, 7537-7540 .

3.1 Overview

Understanding of the crystal chemistry of the prototypical three-dimensional hybrid perovskites, $APbX_3$ (A = MA or FA and X = I, Br or Cl) is essential for optimizing device stability.[66,104,166] Recent research highlights include neutron scattering studies tracking the dynamics of methylammonium ions as well as computational studies describing the lattice dynamics of these materials.[167,168] While many studies have mainly focused on MA based perovskites,[169] there still remain many open questions regarding the general crystal chemistry of FA based perovskites and their responses to external stimuli, such as temperature and pressure.

3.1.1 Phase transitions in MA/FA lead halides

Like solid-state perovskites, MA lead iodide perovskites show an increase of symmetry with increasing temperature.[53,56,67,170] $MAPbI_3$ undergoes a phase transition from orthorhombic ($Pnma$) to a tetragonal ($I4/mcm$) modification at 161 K and further to cubic ($Pm\bar{3}m$) at 327 K, as determined by neutron diffraction (Figure 3-1). The MA ions are ordered in the orthorhombic phase, and turn into disordered orientations in the tetragonal and cubic phases.[53,56,67] $MAPbBr_3$ and $MAPbCl_3$ behave in a similar fashion with phase transition temperatures generally a bit lower.[171] We should note here that the room temperature symmetry of $MAPbI_3$ is currently still under debate from XRD data, arguably in $I4/mcm$ [56], $I4cm$ [72] or $Fmmm$.[170] Cahen *et al.* recently reported ferroelectricity in room temperature $MAPbI_3$, which crystallises in the polar space group of $I4cm$.[72] In comparison to the inorganic analogues, the structural characterization of hybrid halide perovskites is complicated by the floppy PbX_3^- network, the disorder of organic cations as well as the large electron contrast of MA and the lead halide cavity in XRD.[67]

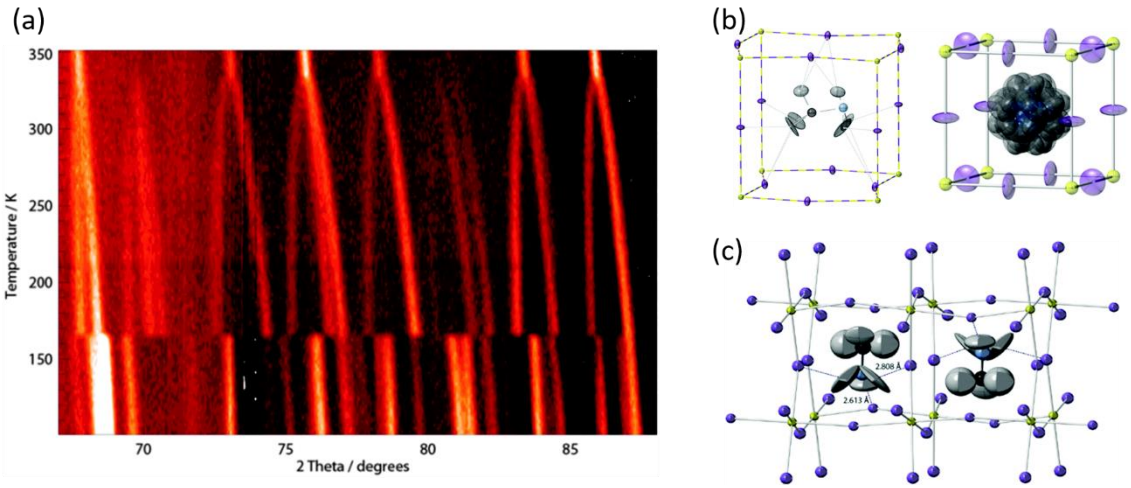

Figure 3-1 (a) Stack plot of $MAPbI_3$from neutron diffraction data (67–88°) over the temperature range of 100 to 352 K. Phase transitions at 165 K and 327 K are observed as is the overall unit cell expansion. (b) Left: one orientation of the MA^+ cation in the tetragonal phase of $MAPbI_3$ at 180 K; the cation is four-fold orientationally disordered around the vertical *c*-axis. Right: orientationally disorder modelled in the cubic phase at 352 K. Thermal ellipsoids at 50% probability. (c) The unit cell of $MAPbI_3$ at 100 K viewed close to *a*-axis with atomic displacement parameters (ADPs) showing as 90% probability ellipsoids; Key: lead yellow, iodine purple, carbon black, nitrogen blue and hydrogen grey. Reproduced from Weller *et al*.[67]

Looking at the FA based hybrid perovskites, on the other hand, there was no reported structural information at the time when the present study started. The $FAPbI_3$ perovskite polymorph slowly converts to the low dimensional structure over time under ambient conditions. The room temperature structure of the metastable perovskite $FAPbI_3$ was firstly published in trigonal space group $P3m_1$by Stoumpos *et al.* in 2013,[66] and was revisited by Weller *et al.* in 2015, where neutron powder diffraction was applied, modelling the cubic structure with the space-group $Pm\bar{3}m$ at room temperature.[172] Seshadri *et al*. recently applied variable temperature powder X-ray diffraction (PXRD) on $FAPbI_3$, finding two phase transitions at low temperatures in the tetragonal space group of $P4/mbm$.[173] The work of this chapter follows on from their important findings and further examines the crystal chemistry of $FAPbX_3$ (X = Br and I).

3.1.2 Responses under pressure

A few high-pressure studies on lead halides perovskites have been reported in the literature, most of them show similar octahedral tilting and induce phase transitions. Swainson *et al.*[174] and Zhao *et al.*[175] studied the high-pressure behaviour of $MAPbBr_3$ using neutron diffraction and powder X-ray diffraction, respectively, observing a phase transition from $Pm\bar{3}m$ to $Im\bar{3}$ below 1 GPa. Shortly after, Karunadasa *et al*. and Szafranski *et al*. investigated the high pressure behaviour of $MAPbI_3$ and concluded similar phase transitions.[61,170] There is a current debate about the existence of an orthorhombic modification of $MAPbBr_3$ and $MAPbI_3$ for pressures larger than $p > 1.8$ GPa. Regarding the high pressure work on FA perovskites, Zou *et al*. reported a high pressure PXRD study on $FAPbBr_3$, where two phase transitions were observed: from $Pm\bar{3}m$ to $Im\bar{3}$ at $p = 0.53$ GPa and the second transition to $Pnma$ at $p = 2.2$ GPa.[129] However, the deformation of $FAPbI_3$ is currently still controversial. $FAPbI_3$ was recently studied at high pressures using PXRD, however, the authors report the absence of any phase transition, despite the occurrence of an abrupt change of lattice parameters a function of pressure.[176] In another recent high-pressure study using PXRD, a transition to an orthorhombic structure in *Imm2* was reported at 0.34 GPa.[177] Our single crystal results do not support their findings, as discussed in Chapter 3.4.

3.1.3 The purpose of present study

It is now established that lead halide perovskites are very dynamic materials, with local symmetry breaking processes present.[131] Therefore, the structural transitions in hybrid perovskites, either triggered by variation of temperature or pressure, are very subtle. It is challenging to examine the small tilting transitions of the already highly dynamic Pb-X-Pb framework. In this context, it is no surprise that there is a current debate about the low temperature and high-pressure structures of lead halide perovskites, especially $MAPbI_3$ and $FAPbI_3$. In their recent review on high-pressure studies of MA-based lead halide perovskites, Szafrański *et al.* summarized the pitfalls and discrepancies in the structural determination of systems under pressure and illustrated that applying pressure is an efficient way to tune the band structures.[178]

The work in this chapter follows on from the current debate, clarifying the structural evolution of FA-based lead halide perovskites as a function of temperature and pressure. The crystal chemistry of the FA lead halide perovskites was explored by single crystal XRD (SCXRD) to understand the phase stability under external stimuli. The responses of $FAPbI_3$ perovskite single crystals under variable temperature (VT) (100 – 450 K) and high pressure (p = ambient – 0.742 GPa) were studied. The experimental results combined with AIMD simulations to examine the cation dynamics in the tetragonal phase, shed light into the nature of the phase transition in $FAPbI_3$. To further understand the effects of FA cations, the thermal response of $FAPbBr_3$ was also studied by VT SCXRD in the similar fashion as $FAPbI_3$, where the octahedral tilting mechanisms and cation dynamics in the tetragonal phase were analyzed. High-pressure XRD of $FAPbBr_3$ were not performed in this research as its phase transition under hydrostatic pressure was reported during the preparation of our experiment.[129] DFT calculations were employed in both systems to study the effect of structural changes on electronic properties.

3.2 Crystal chemistry of $FAPbI_3$

3.2.1 Structural solution and refinement

At T = 300 K, $FAPbI_3$ crystallizes in the expected perovskite structure, with PbI_3^- forming a ReO_3-type cavity and FA cation in the open void for charge balance. A cubic phase with a = 6.3566(2) Å and space group $Pm\bar{3}m$ was determined (R_1 =3.27 %), which was consistent with the observations by Weller *et al.* [18] (See Appendix Figure-A 2). In this $Pm\bar{3}m$ phase the Pb-I-Pb angles are 180°, which enables good mixing of Pb 6s orbitals and I 5p orbitals.[69] We note, however, that the thermal motion of the iodide ions is strongly perpendicular to the Pb-Pb bonding direction (Figure 3-2), as observed previously.[179]

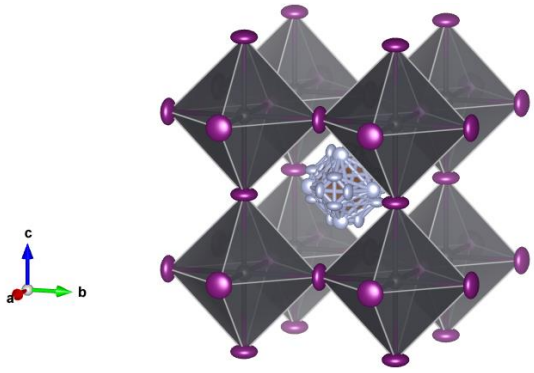

Figure 3-2 Crystal structure of $FAPbI_3$ at 300 K, iodide ions form ellipsoids (shown with 50% probability) that are perpendicular to the Pb-Pb vector in the cubic plane. Grey spheres represent lead, purple represent iodide, carbon (brown) and nitrogen (blue) are modelled with disorder inside the perovskite cage.

The cubic (black, 3D) to hexagonal (yellow, 1D) phase transition was recently reported to be closely related to the entropy of the system and kinetic trapping of the cubic phase could be achieved by thermal quenching.[180] In the present study, starting at T = 300 K, single crystals of the perovskite polymorph of $FAPbI_3$ were heated to T = 450 K and SCXRD data were collected during stepwise cooling to 100 K (cooling rate ≈5 K/min). On cooling $FAPbI_3$ from 450 K, a phase transition from cubic to tetragonal is observed between 300 K and 250 K.

Table 3-1 Details of change in lattice parameters with temperature.

	Temperature (K)	*a*(Å)	c (Å)	Unit Cell Volume (Å^3)
1	300	6.3566(2)		256.84(1)
2	450	6.4009(5)		262.25(4)
3	400	6.3936(4)		261.36(3)
4	350	6.3806(3)		259.77(2)
5	300	6.3667(2)		258.07((2)
6	250	8.9710(7)	6.3427(8)	510.45(9)
7	200	8.9491(6)	6.3283(6)	506.80(7)
8	150	8.9267(6)	6.3126(6)	503.03(7)
9	120	8.8869(3)	6.2854(5)	496.40(5)
10	100	8.8750(20)	6.2820(30)	494.90(3)

In order to solve the low temperature structure from SCXRD, we should mention that the observed systematic absences are not in agreement with a body-centered lattice, which was initially suggested by the indexing routine of CrysAlisPro[144] After carefully examining the systematic absences in the precession images, we solved the low temperature phase in tetragonal symmetry with space group *P4/mbm* (see Appendix Figure-A 3 and Figure-A 4 for precession images with structural solution in the space group and $Im\bar{3}$ and $P4/mbm$, respectively).

In addition, although un-twinned single crystals were selected for X-ray diffraction, structure solution was complicated by crystal twinning which took place upon cooling during the cubic to tetragonal phase transition. The majority of the diffraction spots for the twin components overlap (>70%), hence final structural solutions were refined with one component of the twins to study organic cation orientations, allowing analytical absorption corrections, except at T =100 K where the twinning become severe at low temperatures and the structure were not able to be deduced without a twin model. At T = 250 K, structure solution in $P4/mbm$ (R_1 = 4.45 %) leads to a tetragonal unit cell with a = 8.9710(7) Å and c = 6.3427(8) Å. The atomic coordinates and twining matrix at T = 250 K are listed in Table 3-2 and

Table 3-3 respectively.

Table 3-2 Fractional atomic coordinates and equivalent isotropic displacement parameters (Å^2) for low temperature phases. U_{eq} is defined as 1/3 of the trace of the orthogonalized U_{IJ} tensor.

T (K)		Atom	x	Y	z	Occupancy	U_{eq} (Å^2)	Symmetry
250K	1	Pb	0.000	0.000	0.500	1	0.034(1)	4/m
	2	I1	0.000	0.000	0.000	1	0.094(1)	4/m
	3	I2	0.236(1)	0.736(1)	0.500	1	0.087(1)	m2m
	4	N	0.600(2)	0.100(1)	0.000	1	0.37(4)	m2m
	5	C	0.000	0.500	0.118(7)	0.5	0.17(5)	m2m

Table 3-3 Twinning matrix of $FAPbI_3$ at 250 K.

T (K)	Twin	Twin Ratio	Isolated reflection	Over-lapped reflections	U_{11}	U_{12}	U_{13}	U_{21}	U_{22}	U_{23}	U_{31}	U_{32}	U_{33}
250	1	40.4%	862	738	1	0	0	0	1	0	0	0	1
	2	33.3%	852	731	-0.5	0.5	1.0	0.5	-0.5	1.0	0.5	0.5	0.0
	3	26.4%	841	716	-0.5	-0.5	-1.0	0.5	-0.5	1.0	-0.5	-0.5	0.0

With respect to the ambient temperature cubic cell, the tetragonal cell at low temperatures is 45° tilted within the *ab*-plane, leading to the square root relationship of the lattice parameters *a* and *b*. Such phase transition is related to a change of the octahedral tilting system from $a^0a^0a^0$ for $Pm\bar{3}m$ (zero-tilt system) to $a^0a^0c^+$ (one-tilt system) for $P4/mbm$. The octahedral tilt about the *c*-direction is associated with a reduction of the Pb-I-Pb angles within the *ab*-plane to 173.6°. Interestingly, differential scanning calorimetry (DSC) does not show clear evidence for a phase transition. However, by measuring SCXRD on a different crystal and applying a smaller temperature interval, the phase transition temperature was narrowed down to 260-280 K (see Appendix, Table-A 1 for details of change in lattice parameters), which is in good agreement with the results by Seshadri *et al.*[173] Reducing the temperature to T = 200 K further decreased the lattice parameters and Pb-I-Pb angle to a = 8.9491(6) Å, c = 6.3283(6) Å and 170.6(1)°. The SCXRD datasets collected at T = 250, 200, and 150 K were satisfactorily solved in $P4/mbm$ (Table 3-4, see next page).

Table 3-4 Details of structural solution and refinement of $FAPbI_3$ using VT SCXRD.

Empirical formula	CN_2PbI_3[1]			
Formula weight	632.96			
Crystal size/mm^3	0.24 × 0.14 × 0.06			
Radiation	MoKα (λ = 0.71073Å)			
Crystal system	Cubic	Tetragonal		
Space group	$Pm\bar{3}m$	$P4/mbm$		
Z	1	2		
F(000)	261	522		
Temperature (K)	299.95(10)	150.00 (14)	200.00 (14)	249.95 (10)
a/Å	6.3667(2)	8.9267(6)	8.9491(6)	8.9710(7)
b/Å	6.3667(2)	8.9267(6)	8.9491(6)	8.9710(7)
c/Å	6.3667(2)	6.3126(6)	6.3283(6)	6.3427(8)
α/°	90	90	90	90
β/°	90	90	90	90
γ/°	90	90	90	90
Volume/$Å^3$	258.07(2)	503.03(8)	506.81(8)	510.45(10)
Density (calculated) /gcm^{-1}	4.073	4.146	4.115	4.092
μ/mm^{-1}	25.241	25.9	25.706	25.523
2Θ range for data collection/°	6.4 to 55.678	6.454 to 56.202	6.438 to 56.048	6.422 to 55.902
Index ranges	$-3 \le h \le 8$, $-8 \le k \le 1$, $-3 \le l \le 8$	$-9 \le h \le 10$, $-3 \le k \le 11$, $-8 \le l \le 1$	$-11 \le h \le 3$, $-10 \le k \le 9$, $-1 \le l \le 8$	$-10 \le h \le 9$, $-11 \le k \le 3$, $-8 \le l \le 1$
Reflections collected	584	1051	1064	1089
Independent reflections	90 [R_{int} = 0.0771, R_{sigma} = 0.0439]	337 [R_{int} = 0.0445, R_{sigma} = 0.0423]	343 [R_{int} = 0.0445, R_{sigma} = 0.0472]	346 [R_{int} = 0.0420, R_{sigma} = 0.0403]
Data/restraints/parameters	90/1/12	337/14/14	343/3/14	346/3/18
Goodness-of-fit on F^2	1.274	1.128	1.293	1.055
Final R indexes [I>=2σ (I)]	R_1 = 0.0327, wR_2 = 0.0741	R_1 = 0.0648, wR_2 = 0.1579	R_1 = 0.0629, wR_2 = 0.1948	R_1 = 0.0445, wR_2 = 0.1159
Final R indexes [all data]	R_1 = 0.0419, wR_2 = 0.0909	R_1 = 0.0781, wR_2 = 0.1677	R_1 = 0.0776, wR_2 = 0.2072	R_1 = 0.0655, wR_2 = 0.1323
Largest diff. peak/hole / e $Å^{-3}$	0.95/-1.37	4.11/-3.02	3.00/-2.31	2.31/-1.46

[1]H positions were not considered in the structural solution due to the difficulty of detecting light H in the presence of heavy Pb and I by X-ray diffraction.

Using SCXRD, additional twinning at $T < 150$ K provided an indirect evidence of a phase transition due to the change in cation dynamics. However, it also complicated the structural solutions and a precise crystal structure was not obtained. The experimental SCXRD datasets collected at T = 120 K and T = 100 K were indexed in a primitive tetragonal unit cell for comparative purposes. The observed lattice parameters and volume of the pseudocubic unit cell V' as a function of temperature show clear evidence for a second phase transition below 150 K (Figure 3-3 and Figure 3-4), which is consistent with low temperature PXRD results previously reported.[173] At T = 100 K, three twins were modelled to deduce the unit cell in $P4/mbm$. Further analysis on the data set of T = 120 K and T = 100 K of $FAPbI_3$ by Dr. Fengxia Wei showed that the structure is not incommensurately modulated, since the modulation vectors are (0.33, 0.33, 0), (-0.33, 0.33, 0) and (0, 0, 0.167) respectively, which are special positions.

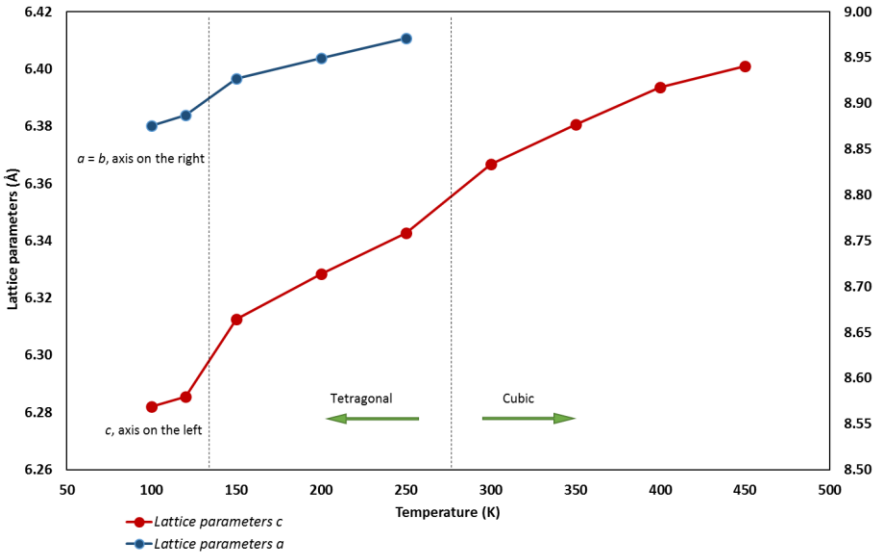

Figure 3-3 Change in lattice parameters as a function of temperature. A cubic to tetragonal phase transition was observed on cooling from 300 K to 250 K and a second phase transition was observed below 150 K.

As shown in Figure 3-3, positive thermal expansion was observed along the principal axes. The deduced thermal expansion coefficients are: 250 K – 450 K (10^{-5}/K): α_a = 3.2, α_v = 9.6 and 150 K – 250 K (10^{-5}/K): α_a = 4.9, α_c = 4.8, α_v = 14.8. $FAPbI_3$, especially the tetragonal phase structure, showed relatively large thermoelastic responses in comparison to its inorganic analogues. Our findings on the thermal expansion parameters are in good

agreement with the measurement from PXRD by Seshadri *et al*.[173] We also note that the thermal expansion coefficients of $FAPbI_3$ are comparable to $MAPbI_3$,[181] and are lower than the values in MA/$FAPbI_3$ alloy, $FA_{0.5}MA_{0.5}PbI_3$..[52]

3.2.2 Cation dynamics

From the SCXRD data, it was possible to locate the orientations of the FA cations, which have hitherto been unresolved. Electron densities of the nitrogen atoms lying on the *ab*-plane were observed, as shown in Figure 3-4 (a). Two possible carbon positions were observed in this dataset at 250 K with C-H bonds aligned parallel to the *c*-axis, which have been modelled using partial occupancies. The closest N···I distances are 3.7017(3) Å and 3.7966(4) Å, and the C···I distance is 3.8512(3) Å. For $MAPbI_3$, where the cation positions were well defined at 100 K, the N···I distances in the orthorhombic phase are 3.611 Å and 3.681 Å, and the closest C···I distance is 4.090 Å [67,68]. The longer N···I distance in the FA perovskite indicate weaker hydrogen bonding.

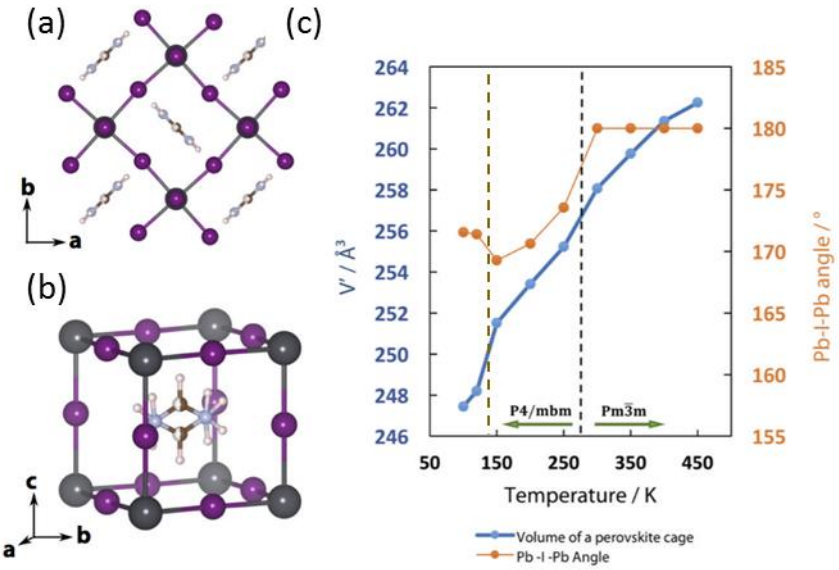

Figure 3-4 (a) $FAPbI_3$ unit cell in P4/mbm at 250 K shows the alignment of FA cations observed by X-ray diffraction. View is along the *c*-axis where tilting of the octahedra is seen and the N-N axis lies along <110> in the *ab*-plane. (b) Illustration of two disordered formamidinium cations superimposed inside a pseudocubic cage. (c) Volume of the pseudocubic perovskite cell, V', for $FAPbI_3$ (blue), and the Pb-I-Pb angle (orange) as a function of temperature.

AIMD simulations was conducted for $FAPbBr_3$ in tetragonal space group at T = 200 K. In agreement with the experimental observations, the calculations showed that the FA cation rotates around the N-N axis, with fixed positions of NH_2 groups. Hydrogen bonding interactions between the NH_2 groups and the PbI_3^- cage presumably control the energy barrier for the motion of FA.[182,183] Our results showed that NH_2 groups were locked, leaving the CH group free to rotate. Statistical analysis of the AIMD simulations revealed that FA cations had two preferred orientations (Figure 3-5). In the first and statistically more probable orientation, the C-H bond of FA cation lied within the *ab* plane (θ = 0) and pointed at the open face of the lead iodide framework. In the second orientation, the C-H bond was parallel to the *c*-axis (θ = 90°), similarly pointing at an open face. This observation agreed with the tetragonal symmetry where the *c*-axis depicts the unique axis of the unit cell.

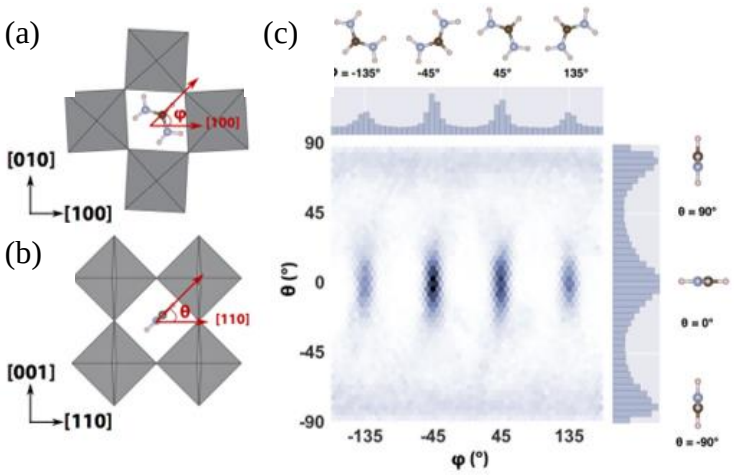

Figure 3-5 Statistical sampling of the FA cation orientation in the low temperature tetragonal phase is modelled by AIMD. The orientation is defined by (a) φ (the angle between the C-H vector and the *a*-axis) and (b) θ (the angle between the C-H vector and *ab*-plane). The statistical distributions of θ and φ are shown in (c).

3.3 Crystal chemistry of $FAPbBr_3$

$FAPbBr_3$ crystallizes in a similar fashion as $MAPbBr_3$, with a = 5.9820(2) Å in a cubic space group of $Pm\bar{3}m$ at room temperature. Upon cooling, cubic-tetragonal phase transition occurs at around 250 K for $FAPbBr_3$. Space group of $P4/mbm$ was suggested by the indexing routine of CrysAlisPro.[144] Similar to $FAPbI_3$, octahedral tilting of the

inorganic framework from $a^0a^0a^0$ to $a^0a^0c^+$ was observed in the cubic-tetragonal phase transition, as shown in Figure 3-6.

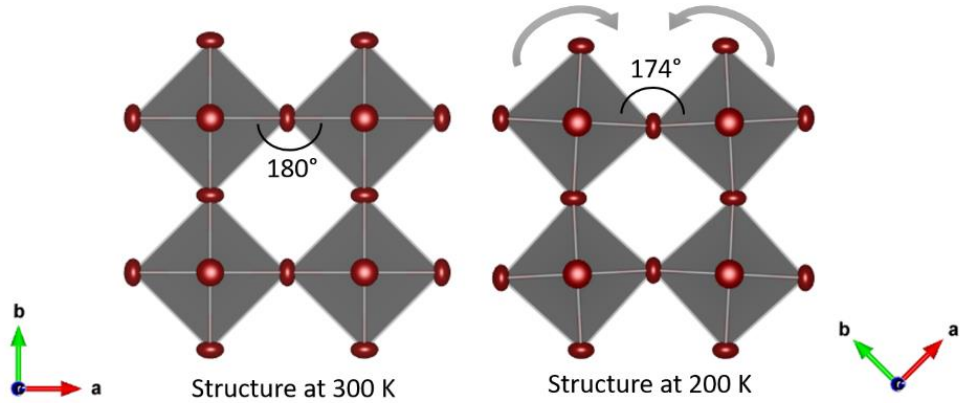

Figure 3-6 Inorganic perovskite framework of the cubic $FAPbBr_3$ and the octahedral tiling in tetragonal phase.

The low temperature crystal chemistry of $FAPbBr_3$ follows a similar trend to $FAPbI_3$. Phase transitions were evident from the discontinuity of the volume change, as shown in Figure 3-7 (a), where α phase refers to the cubic phase $FAPbBr_3$, β and γ phase are assigned to the two tetragonal phases in $P4/mbm$. Such discontinuities are also observed in the changes in Pb – Br angles and lattice parameters (Figure 3-7 (b)), Pb – Br distances (Figure 3-7 (c) and the thermal parameters of Pb, the heaviest X-ray scatterer in this system (Figure 3-7 (d)). The thermal expansions of $FAPbBr_3$ are: 250K – 400 K (10^{-5}/K): $\alpha_a = 5.2$, $\alpha_v = 15.9$ and 150 K – 240 K (10^{-5}/K): $\alpha_a = 5.4$, $\alpha_c = 5.9$, $\alpha_v = 17.3$.

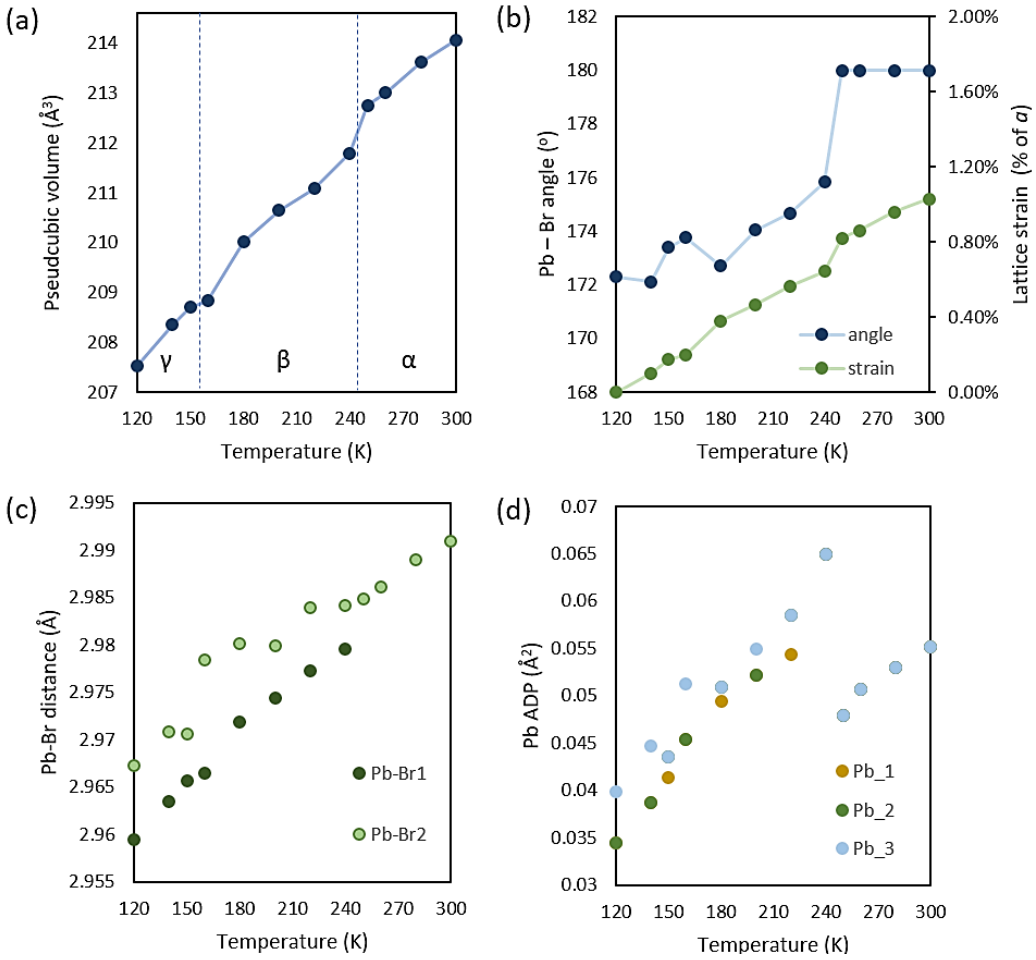

Figure 3-7 (a) Pseudocubic unit cell volume, (b) Pb-Br-Pb angles and % changes in lattice parameters, (c) Pb-Br distances and (d) the Pb anisotropic thermal parameters of $FAPbBr_3$ as a function of temperature.

Unlike the clear indication of phase transition from cubic to tetragonal symmetry, the crystallographic changes below 160 K are subtler and hard to detect due to the increasing twinning on cooling. The Pb – Br – Pb angle on the *ab* plane reduces monotonically as the temperature decreases from 240 K, reflecting on the emergence of tetragonality. However, an increase in this angle was observed at 150 – 160 K (Figure 2 (b)), which reflects on the reentrant cubic pseudosymmetry. The non-linear decrease in the Pb – Br distance (Figure 2(c) and the slight increase in Pb ADPs (Figure 2(d)) in the same temperature range also suggests that the system undergoes subtle crystallographic changes that are not fully captured in the β phase model.

Although twining occurred on cooling since the α to β transition at 240 K, structural solutions of T < 150 K exhibited a different twining matrix to higher temperatures. Within the same crystal, SCXRD data at 200 K and 120 K, which are before and after the β to γ transition temperature, respectively, showed different orientation relationships between the two twins, as shown in Table 3-5.

Table 3-5 Twining matrices of $FAPbBr_3$.

T (K)	Twin	Twin Ratio	Isolated reflection	Over-lapped	U_{11}	U_{12}	U_{13}	U_{21}	U_{22}	U_{23}	U_{31}	U_{32}	U_{33}
200	1	43.4%	402	256	1	0	0	0	1	0	0	0	1
	2	56.6%	403	256	0.5	-0.5	1.0	-0.5	0.5	1.0	-0.5	-0.5	0.0
120	1	58.1%	355	288	1	0	0	0	1	0	0	0	1
	2	42.0%	349	288	-0.5	-0.5	1.0	-0.5	-0.5	-1.0	0.5	-0.5	0.0

FA cations are fully disordered in the cubic α phase at room temperature. However, it is expected that due to the large size and asymmetric shape, there is a higher energy barrier for cation dynamics in $FAPbBr_3$ than $MAPbBr_3$.[184] As the temperature decreases, although the FA cation is still disordered in the tetragonal phase, the overall thermal motion of the FA cation forms a "disc" $P4/mbm$ than a "sphere" in $Pm\bar{3}m$. From SCXRD we could locate the positions of the nitrogen atoms from their electron densities, since the N – N axis of the FA cation lies parallel to the *ab* plane along the <110> directions in the tetragonal matrix. As shown in Figure 3-8, $FAPbBr_3$ crystal structure at 200 K (β phase) and 120 K (γ phases) show similar unit cells. Both structures were solved in the space group of $P4/mbm$ with reasonable R_1 values (around 5% modelling as 2 twins and 7% as 1 single crystal). In addition, at T = 120 K, the structure could also be modelled in $P4bm$, which is a polar sub-space group of $P4/mbm$. Both $P4/mbm$ and $P4bm$ gave reasonable refinement parameters and were not distinguishable due to the

insensitivity of light atoms in the presence of the heavy Pb as well as the additional twining on cooling.

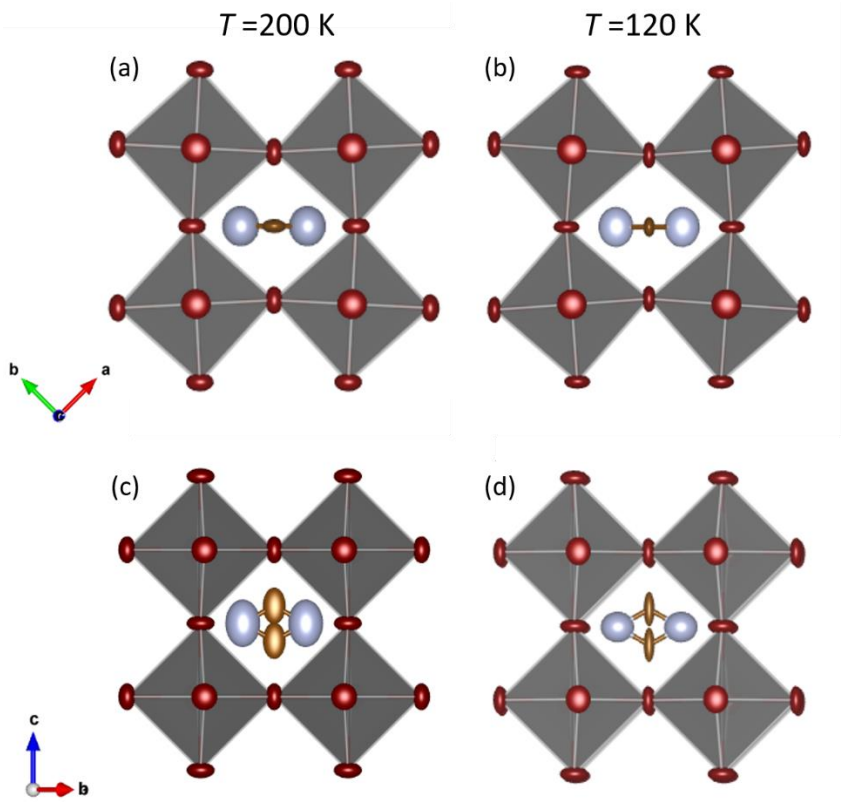

Figure 3-8 Pseudocubic perovskite cells of $FAPbBr_3$ at 200 K (a) and (c), and 120K (b) and (d), respectively shown in thermal ellipsoids (50%). Red spheres represent bromine, blue represents nitrogen and brown represents carbon atoms. Hydrogen atoms were not assigned due to X-ray insensitivity in the presence of heavy scatters such as Pb and Br. Carbon atoms are modelled with partial occupies.

Interestingly, thermal ellipsoids of cation and nitrogen showed different shapes at 200 K and 120K in addition to the reduction in sizes at the lower temperature. At 200 K, the favored orientation of the FA cation is that the N – N axis sits pointing the face of the *ab* plane, leaving the CH group free to rotate about the N – N axis (Figure 3-8 (a)). From the elongated shapes of the thermal ellipsoids of the organic cations shown in (b), in particular the carbon atoms, we can see there are also some disorders associated with rotations normal to the N – C – N plane. However, this rotation was significantly quenched at 120 K (Figure 3-8 (c) and (d)), with more defined distance between nitrogen and its nearest bromine. Such lock-in may be due to the stronger NH-Br hydrogen bonding. On the other hand, the disorder of the carbon atom rotating about the N-N axis

is remained at 120 K in the structural model of $P4/mbm$. The quenched rotational disorder of the FA cation normal to its N – C – N plane may be the mechanism underlying the β to γ phase transition. The distortions of the cavity due to reduced lattice parameters, bond distances and different octahedral tilting modes can quench the dynamics of FA cations, thereby affect the symmetry of the system.[185] Like the MA based perovskite systems, one explanation of the initiation of the phase transitions is that the induced tilting acts as a response to the reduced temperature, and hence the reduced entropy gain from disorder of FA cations. [186] The atomic positions of $FAPbBr_3$ cubic and tetragonal space group are listed in Table 3-6 and structural solution and refinement is summarized in Table 3-7.

Table 3-6 Atomic positions of the inorganic framework in $FAPbBr_3$ (solved in tetragonal space group $P4/mbm$).

T (K)				x	y	z	Occ.	U_{iso}	Site	Sym.
300	1	Pb	Pb1	0.500	0.500	0.500	1	0.057(1)	1b	m3m
	2	Br	Br2	0.000	0.500	0.500	1	0.17(3)	3c	4/mmm
200	1	Pb	Pb1	0.000	0.000	0.500	1	0.053(1)	2b	4/m
	2	Br	Br2	0.238(1)	0.738(1)	0.500	1	0.098(2)	4h	m2m
	3	Br	Br1	0.000	0.000	0.000	1	0.106(3)	2a	4/m
	4	N	N6	0.607(1)	0.107(1)	0.000	1	0.28(3)	4g	m2m
	5	C	C5	0.000	0.500	0.119(8)	0.5	0.12(4)	4f	2.m
120	1	Pb	Pb1	0.000	0.000	0.500	1	0.039(1)	2b	4/m
	2	Br	Br2	0.233(1)	0.733(1)	0.500	1	0.093(5)	4h	m2m
	3	Br	Br1	0.000	0.000	0.000	1	0.106(7)	2a	4/m
	4	N	N1	0.607(1)	0.107(1)	0.000	1	0.22(7)	4g	m2m
	5	C	C2	0.000	0.500	0.121(1)	0.5	0.10(1)	4f	2m

Table 3-7 Crystallographic data and refinement of $FAPbBr_3$.

Empirical formula	Br_3C_2NPb		
Formula weight	491.99		
Crystal size/mm^3	0.18 × 0.16 × 0.13		
Radiation	MoK_α (λ = 0.71073)		
Crystal system	Cubic	Tetragonal	
Space group	$Pm\bar{3}m$	$P4/mbm$	
Z	1	2	
F(000)	212	414	
Temperature (k)	300.1(5)	120.10 (14) K	200.00 (14) K
a/Å	5.9820(2)	8.3738(3)	8.4179(3)
b/Å	5.9820(2)	8.3738(3)	8.4179(3)
c/Å	5.9820(2)	5.9189(4)	5.9488(4)
α/°	90	90	90
β/°	90	90	90
γ/°	90	90	90
Volume/$Å^3$	214.063(19)	415.04(4)	421.54(4)
Density (calculated) /gcm^{-1}	3.777	3.897	3.836
μ/mm^{-1}	33.612	34.672	34.137
2Θ range for data collection/°	6.812 to 55.778	6.882 to 56.406	6.846 to 56.11
Index ranges	$-2 \le h \le 7$, $-1 \le k \le 7$, $-7 \le l \le 3$	$-10 \le h \le 3$, $-7 \le k \le 7$, $-7 \le l \le 2$	$-7 \le h \le 8$, $-2 \le k \le 10$, $-3 \le l \le 7$
Reflections collected	380	687	703
Independent reflections	75 [R_{int} = 0.0376, R_{sigma} = 0.0215]	272 [R_{int} = 0.0197, R_{sigma} = 0.0260]	254 [R_{int} = 0.0204, R_{sigma} = 0.0184]
Data/restraints/parameters	75/0/9	272/3/17	254/3/17
Goodness-of-fit on F^2	1.018	1.216	1.169
Final R indexes [I>=2σ (I)]	R_1 = 0.0269, wR_2 = 0.0599	R_1 = 0.0751, wR_2 = 0.2000	R_1 = 0.0698, wR_2 = 0.1786
Final R indexes [all data]	R_1 = 0.0275, wR_2 = 0.0586	R_1 = 0.0822, wR_2 = 0.2096	R_1 = 0.0795, wR_2 = 0.1924
Largest diff. peak/hole / e $Å^{-3}$	0.76/-0.85	4.46/-1.30	2.87/-0.98

*H positions were not considered in the structural solution due to the difficulty of detecting light H in the presence of heavy Pb and Br in X-ray diffraction.

3.4 High pressure crystallography of $FAPbI_3$

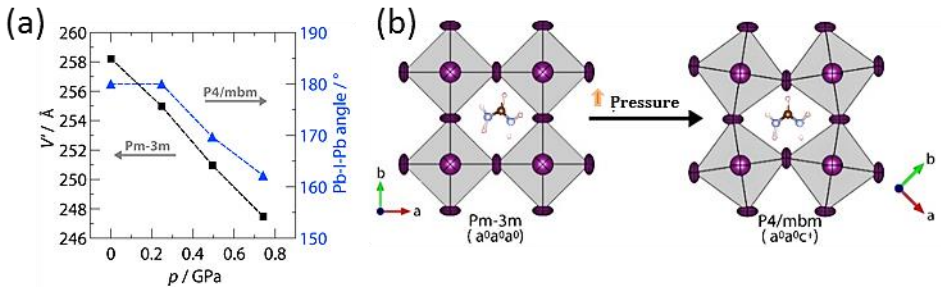

Figure 3-9 (a) Experimentally measured volume of the pseudocubic cell, V', for $FAPbI_3$ (black points) and the Pb-I-Pb angle (blue points), (b) illustration of phase transition under hydrostatic pressure.

Increasing the pressure from the ambient condition led to a reduction of the lattice parameters and Pb – I bond lengths, *e.g.* a = 6.3413(2) Å at p = 0.247 GPa. When p = 0.494 GPa, a phase transition was observed. In analogy with the VT SCXRD study, the indexing routine implemented in CrysAlisPro suggested body-centered cubic as the lattice type. However, close inspection of the (hk0) precession image indicates systematic absences contradicting the assignment of $Im\bar{3}$. Following Glazer tilt notations, and thereby eliminating many space group possibilities, a structure solution in $P4/mbm$ was attempted. The tetragonal solution gives improved refinement values with respect to solution in a cubic: R_1 = 6.50 % with a = 8.9148(6) Å and c = 6.3138(7) Å. Similar to the VT study, twinning of the crystal over the phase transition challenges structure solution.[178] The diffraction intensities that would indicate doubling of the unit cell could be explained by twinning. Twinning was explicitly taken into account during structure solution and refinement for datasets with p > 0.25 GPa.The phase transition was signaled by a reduction of the Pb –I –Pb angles within the *ab* – plane to 169.5° at p = 0.494 GPa. Increasing the pressure to p = 0.741 GPa further reduces the Pb – I – Pb angle to 162.0° and simultaneously the lattice parameters to a = 8.8430(6) Å and c = 6.27090(6) Å. The unit cell volume of the pseudocubic perovskite cell (V') as a function of pressure is given in Figure 3-9 (a). This structural model did not include the formamidinium cation, which is not well-defined in the high-pressure experiments, the octahedral tilting is shown in Figure 3-9 (b). High-pressure single crystal diffraction experiments were performed by the author, Dr. Fengxia Wei and Dr. Gregor Kislech at I15 Diamond Light Source to further investigate the crystal chemistry of $FAPbI_3$. Structural solutions were deduced by Dr. Gregor Kieslich.

3.5 Electronic structures

To understand the effect of phase transition on electronic structures, ground state DFT calculations were performed by Zeyu Deng using the experimental lattice parameters to analyse the impact of the phase transition on the electronic properties. Since the band edges in $APbX_3$ materials solely exhibit contributions from the inorganic framework, the cage was considered, with charge balance maintained by adding a positive background charge in the calculations.[69] We note that DFT calculations with spin-orbit coupling generally underestimate the band gap; however, as we are only interested in relative changes of the band gap, this is not of further concern (see Fig. 2 in Ref. [187]). As expected, the calculated band gap decreases by 0.017 eV from T = 300 K (0.148 eV) to T = 250 K (0.131 eV), because of reduced lattice parameters and Pb – I bond lengths. After the phase transition to the tetragonal phase, a Pb – I – Pb angle smaller than 180° is expected to increase the band gap due to a weaker orbital overlap[69] and therefore counteracts the effect of reduced cell dimensions and bond lengths on the band gap. For $FAPbBr_3$, the calculated electronic band gaps also show a decrease from cubic to tetragonal space group, with 0.557 eV and 0.504 eV for 300 K and 120 K structure, respectively.

With increasing pressure, on the other hand, at p = 0.247 GPa, the reduced lattice parameters and concomitantly the Pb – I bond lengths in the cubic $FAPbI_3$ phase leads to a slight reduction of the band gap. This reduction is caused by increased hybridization of the Pb – I antibonding states near the band edges leading to a shift in their energy. Further increase in pressure leads to the reduction in the Pb– I – Pb angle within the *ab* plane. When p = 0.494 GPa, the reduced lattice parameters and Pb – I bond lengths still have a larger lowering effect on the band gap than the reduction in Pb – I – Pb angle to about 170°. However, when the angle decreases to 162.27° at p = 0.741 GPa, the significant tilting leads to more pronounced influence on the bonding. At this pressure, the Pb – I – Pb angle governs the band gap, which now exceeds the initial band gap at ambient pressure by 0.05 eV.

3.6 Conclusions and future work

In summary, variable temperature and high-pressure crystal structure and chemistry of the FA lead halides were investigated using SCXRD in order to understand the structural response of hybrid perovskites to an external stimulus such as pressure or temperature. Two phase transitions from a cubic modification to lower symmetry were found at low temperatures on both $FAPbI_3$ and $FAPbBr_3$. The cubic-tetragonal phase transition temperatures are 260 K – 280 K for iodide and 240 – 250 K for bromide perovskites respectively. $P4/mbm$ is a possible space group for low temperature FA lead halide structures. Further cooling to around 150 K, a second phase transition was observed for both iodide and bromide perovskites, which could be also solved in both $P4/mbm$ and *P4bm* with reasonable refinement.

Cation dynamics was found to be hindered at the low temperatures, and hence the different degrees of the rotational disorder lead to observed order-disorder phase transitions. In addition, hydrostatic deformations of the $FAPbI_3$ were studied by high pressure SCXRD. Similar to the low temperature study, octahedral tilting could be used to describe behavior of $FAPbI_3$ under hydrostatic pressure and the crystal structure at p = 0.494 GPa could be solved in $P4/mbm$. Importantly, the present study established for the first time the orientations of the formamidinium cations in the low temperature phase. In the tetragonal phase with $a^0a^0c^+$ octahedral tiling system, rotational disorder of the cation dynamics is hindered, with the N – N axis of the FA cation found aligning parallel to <110> in $P4/mbm$.

Our study emphasizes that a thorough analysis of single crystal X-ray data is important as twinning challenges the standard indexing routines. By employing *ab initio* MD simulations, the dynamics of the FA cation in the tetragonal phase was studied. Two preferred orientations were found, with C-H bond rotating along the N – N axis, which were in good agreement with the experimental data. For phase transitions below 150 K, further neutron diffraction studies could be applied to distinguish $P4/mbm$ and $P4bm$ and determine the crystal structure at extremely low temperatures with fully ordered cations. As anticipated, the DFT calculations show that the low temperature and high-pressure electronic structures are governed by the interplay between reduced lattice

dimensions and octahedral tilting. We show these are the dominant factors in determining the bandgap, which can be tuned through pressure.

Chapter 4 Intrinsic strain in lead bromide perovskites

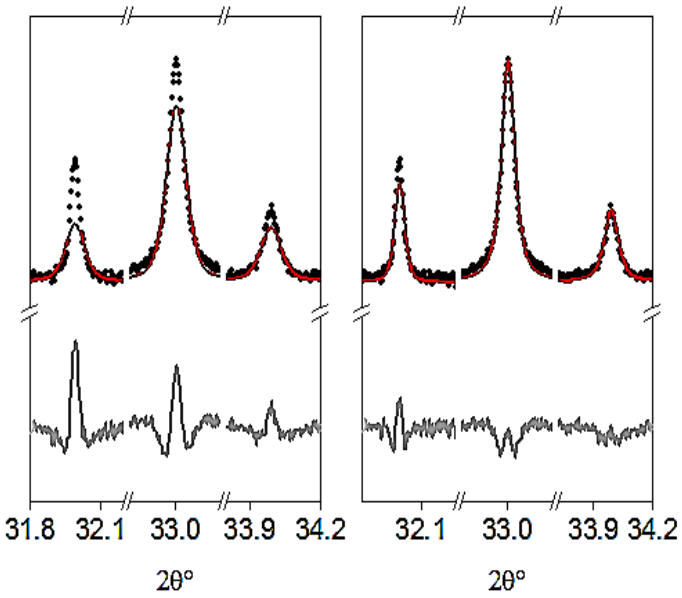

In this chapter, the intrinsic strain in the cubic hybrid bromide perovskites was studied systematically by powder X-ray diffraction. Comparative studies on $FAPbBr_3$ and $MAPbBr_3$ were first conducted and the results showed that the cubic $FAPbBr_3$ lattice was more strained. To better model this large strain effect quantitively, synchrotron PXRD of $FAPbBr_3$ was collected at 290 K and modelled using Rietveld refinement. The origins of the anisotropic strain effects were explored by density functional theory (DFT) and high-resolution transmission electron microscopy (HRTEM). Our study reveals the interplay between the A-site cations and the inorganic framework.

Results in this chapter are currently in preparation and will be submitted for publication in the near future.

4.1 Overview

$FAPbBr_3$ was recently reported to show a superior carrier lifetime and diffusion length compared to $MAPbBr_3$ in both single crystals[46] and solution processed thin films.[188] Furthermore, although the bandgap of $FAPbBr_3$ is 2.3 eV, Meng *et al*. reported that it also displays a sub-bandgap emission at 1.7 eV, which makes it a promising candidate for light-emitting diodes.[39] These observations have raised interest in the intrinsic properties of these perovskites, in particular the defects, cation disorder, and lattice distortions that can influence their exceptional properties. However, despite their outstanding device performances, little is known about the intrinsic structural differences between FA and MA bromide perovskites. The links between the A cation sizes and their lattice distortions, for example, remain unresolved.

4.1.1 Strain and device performances

In terms of crystal chemistry, both $MAPbBr_3$ and $FAPbBr_3$ adopt a cubic perovskite structure at room temperature with the space group $Pm\bar{3}m$.[46] From rocking curve analysis on the (100) planes, the full width at half maximum (FWHM) of $FAPbBr_3$ is only very slightly higher than its MA counterpart.[46] It has been recently shown that lattice relaxation by annealing leads to improved photovoltaic performance in MA based perovskites. The highest efficiency was achieved at the annealing temperatures that led to the least lattice strains.[189] Here we note that by replacing MA with FA, the crystal chemistry becomes more complicated, as discussed in Chapter 3. Although in both cases the cations are disordered, computational studies show that the larger size and anisotropic shape of the FA cations create a higher rotational energy barrier.[182,184] $FAPbI_3$, also a cubic perovskite, was recently reported to exhibit improved phase stability when alloyed with MA and Br as a result of strain relaxation along [111].[73] This observation encouraged us to perform systematic studies on the intrinsic strains of the hybrid perovskites, which should provide a solid platform for designing perovskite alloys and improving their device performance.

4.1.2 Lattice distortions in perovskites

Lattice distortions and inhomogeneous strain fields have been observed in inorganic perovskite structures. For example, lead zinc niobium oxide (PZN), known as an excellent relaxor ferroelectric with space group of $R3m$, exhibits anisotropic strain broadening in its neutron diffraction pattern.[190,190] Similar anisotropic line broadening was also observed in lead zirconate titanate (PZT); this was attributed to the size mismatch from Zr doping on Nb or Ti sites as well as the resultant shifts of the Pb ions.[191] Noteworthy, although there has been no systematic modelling of the anisotropic peak broadening reported on HOIPs, Vogt *et al*. observed different pressure dependent strains along <100>, <110> and <111> on the cubic $MASnI_3$ with high pressure X-ray powder diffraction.[130] In particular, the study argued that the symmetry allowed octahedral tilting displaces the Sn-I-Sn linkages away from <100>, which stabilized the lattice strains along <100>, while strains in non-<100> directions increases with pressure.

4.1.3 Purpose of the present study

Motivated by the recent interest in improving the perovskite stability by strain relaxation, the present work was focused on the intrinsic strain in the lead bromide perovskites. It becomes important to understand how much the perovskite framework is distorted and in which directions. In their recent study, Seshadri *et al.* reported a key aspect of the inorganic framework of HOIPs potentially impacting the electronic, thermal, and dielectric properties, which is the off-centering of the Pb and Sn at room temperature due to lone pair stereochemistry.[192] Such local off-centering is expected to be unobservable in the traditional X-ray diffraction technique based on Bragg crystallography.[131] However, in this study, we were able to model this intrinsic anisotropy of based upon Rietveld analysis of powder X-ray diffraction (PXRD) data. Using laboratory X-ray diffraction, we examined the strained nature of the perovskites on the entire powder pattern of $MAPbBr_3$ and $FAPbBr_3$, instead of analysing individual Bragg reflections. We then focused on $FAPbBr_3$, which exhibited large anisotropic strains, by analysing the synchrotron PXRD pattern. To further understand the dynamics in the $FAPbBr_3$, DFT calculations were employed, which shed light on the A-cation behaviour and its effect on the inorganic cage. To confirm that the observed strain effect in X-ray diffraction is an intrinsic characteristic, HRTEM was applied using the as-synthesised sample with no

mechanical grinding or post-synthetic treatment and direct evidence of lattice distortions was observed.

4.2 Theoretical background

4.2.1 Origin of Line broadening in PXRD

The powder diffraction pattern obtained from X-ray diffraction contains a wealth of information in addition to the crystal phase identification, as shown in Figure 4-1.

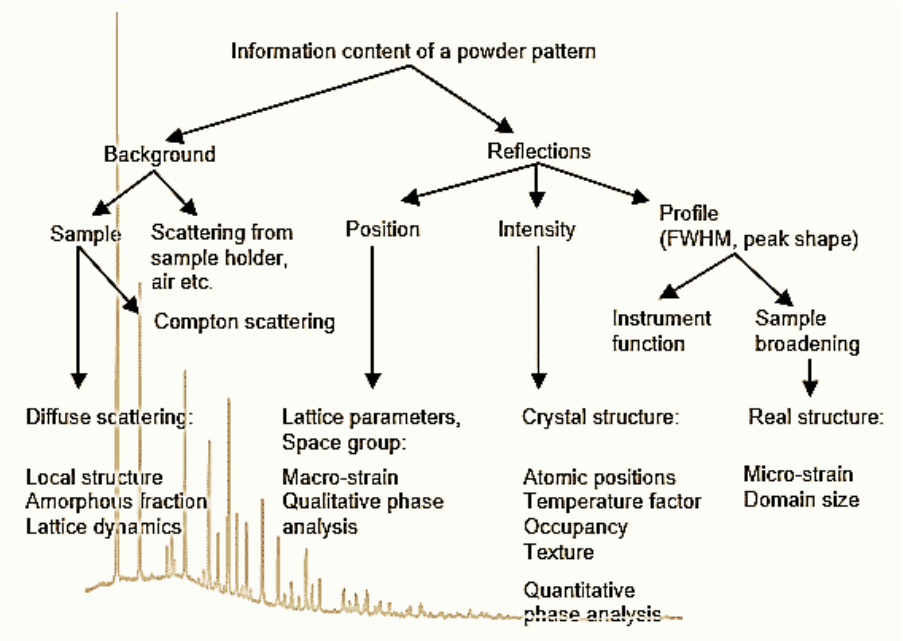

Figure 4-1 Information content of PXRD pattern, reproduced from *Powder diffraction: theory and practice* (edited by Dinnebier and Billinge).[193]

Considering the peak profile, line broadening in PXRD consists of the contribution from an imperfect instrument and an imperfect sample. Mathematically, it forms a convolution of the two effects. The instrumental contribution can rise from the finite size of the radiation source and diffracting volume of the sample, axial divergence, the configuration of the slits used in the diffractometer, any misalignment of the diffractometer and so on.[194] In Gaussian and Lorentzian peak functions, the instrumental function convolve in different ways, shown as the following:

Gaussian:

$$B_{total}{}^2 = B_{instrument}{}^2 + B_{sample}{}^2$$

Lorentzian:

$$B_{total} = B_{instrument} + B_{sample}$$

where B is the integral breath of individual peaks. [194] The instrumental broadening is commonly measured using a material such as LaB_6 (NIST standard) which shows little broadening and it can be neglected if $B_{instrument} << B_{sample}$.

The observed sample broadening, B_{sample} can be related to the major two sources from the crystal structure: limited crystallite size (coherence length) or strain (inhomogeneous variation in d-spacing), as discussed in the next section. Size broadening is diffraction order independent, but, strain broadening increases with diffraction order. The former tends to be more dominant at lower angles.[195]

4.2.2 Sample broadening

4.2.2.1 Crystallite size

In 1918, Scherrer related the volume-averaged crystallite size, L, of a powder to the broadening, B, of its powder diffraction peaks as the following:

$$B_L = \frac{K\lambda}{Lcos\theta}$$

where θ is the Bragg reflection angle, λ is the radiation wavelength, and K is a constant close to unity depending on the crystallite shapes. The use of peak broadening to determine crystallite size is normally limited to cases where the average crystallite size is ≤ 1 μm.

4.2.2.2 Strain

The presence of lattice strain alters the *d* spacings, as shown in Figure 4-2.

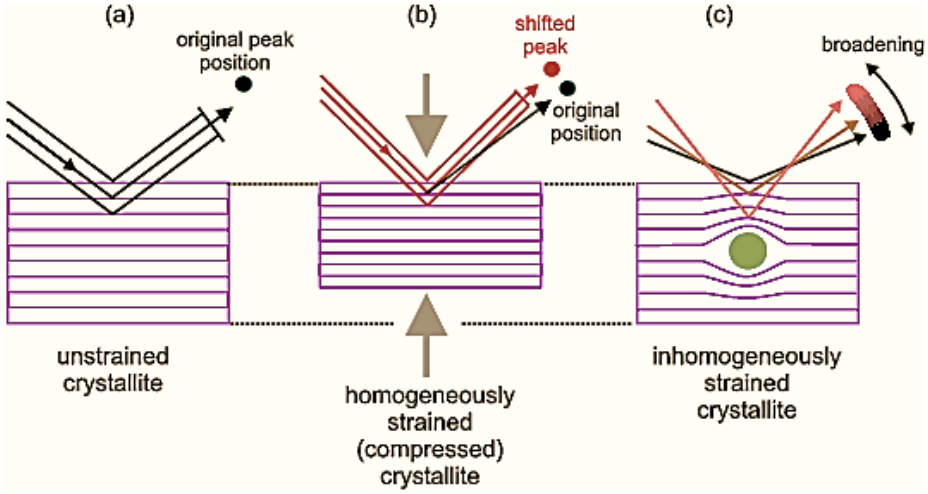

Figure 4-2 Schematic illustration of the effects of strain on peak profile.[194]

If crystallites were all strained by the same amount, a peak shift from 2θ°to 2(θ + δθ)° would be observed, as seen in Figure 4-2 (b). However, under inhomogeneous strain, for example a lattice defect shown in Figure 4-2(c), different crystallites are strained by different amounts and hence result in different peak shifts. The overall effect of such strain is peak broadening and it follows the relationship to the Bragg angle as the following:

$$B_\varepsilon = C\varepsilon \tan\theta$$

where ε is the strain and *C* is a constant depending on the nature of the strain.[194]

Peak shifts and broadening in X-ray diffraction refers to the crystal imperfection and microstructure shows the extent and quality of the crystal imperfection. Considering the microstructural origin of the strain, the most common sources of strain include dislocations (density > 5×10^{12} m^{-2}), stacking faults, twinning, microstresses and internal stresses, grain boundaries, chemical heterogeneities, interstitials and vacancies etc.[195] In addition, the disorder along the direction of stacking of atomic planes can change the coherency of diffraction along that direction, and hence such "faults" in the crystal lattice, for example anti-phase domain boundaries, can also lead to *hkl*-dependent peak broadening.[138]

4.2.3 Peak analysis

4.2.3.1 Williamson-Hall Plot

The Williamson and Hall plot is a classical method developed by G. K. Williamson and his student, W. H. Hall, to obtain qualitative information of anisotropy in broadening.[196] The method separates the size and strain contributions to X-ray peak profile (integral breadth) based on the different angular dependencies of the two effects, since the size contribution varies as $1/cos\theta$ and the strain as $tan\theta$. Assuming the peak shape is Lorentzian, the peak broadening can be described as:

$$B_{sample} = B_L + B_\varepsilon = \frac{K\lambda}{Lcos\theta} + C\varepsilon\, tan\theta$$

Rearranging the equation we obtain:

$$B_{sample}cos\theta = \frac{K\lambda}{L} + C\varepsilon\, sin\theta$$

By plotting $B_{sample}cos\theta$ versus $sin\theta$, the strain component from the slope ($C\varepsilon$) and the size component from the intercept ($K\lambda/L$) can be obtained.

4.2.3.2 Anisotropic peak broadening model

In 1998, Stephens developed a phenomenological fit for peak widths which are not monotonic functions of the diffraction angle, known as anisotropic strain broadening.[197] The model considers the distribution of lattice metric parameters within the powder diffraction sample and each crystallite is regarded as having its own lattice parameters, with a distribution throughout the powder sample.[198] This model doesn't include size effects and microstructural defects such as stacking faults.

The Stephens model defines the variance in $(1/d)^2$, (written as M_{hkl}) according to the following relationship:

$$\sigma^2(M_{hkl}) = \sum S_{HKL}\, h^H k^K l^L, \text{ where } H + K + L = 4.$$[197]

In a crystal lattice with cubic symmetry, for example, $S_{400} = S_{040} = S_{004}$ and $S_{220} = S_{202} = S_{022}$. Hence the two independent anisotropic strain parameters, S_{400} and S_{220}, can be refined to achieve optimal fits. In this case,

$$\sigma^2(M_{hkl}) = S_{400}(h^4 + k^4 + l^4) + S_{220}(h^2k^2 + k^2l^2 + h^2l^2)$$

4.3 Comparative studies of $FAPbBr_3$ and $MAPbBr_3$

In terms of crystal chemistry, both $MAPbBr_3$ and $FAPbBr_3$ adopt a cubic perovskite structure at room temperature with space group $Pm\bar{3}m$.[46] $FAPbBr_3$ has a slightly larger unit cell (the Pb-Br bond is 1.1% longer than in MA) and a higher tolerance factor (1.01 versus 0.93).[6,133] Although the structure and phase stability of $MAPbBr_3$ perovskites have been widely studied,[57,60,171,199] fewer reports have focused on $FAPbBr_3$.[129,200]

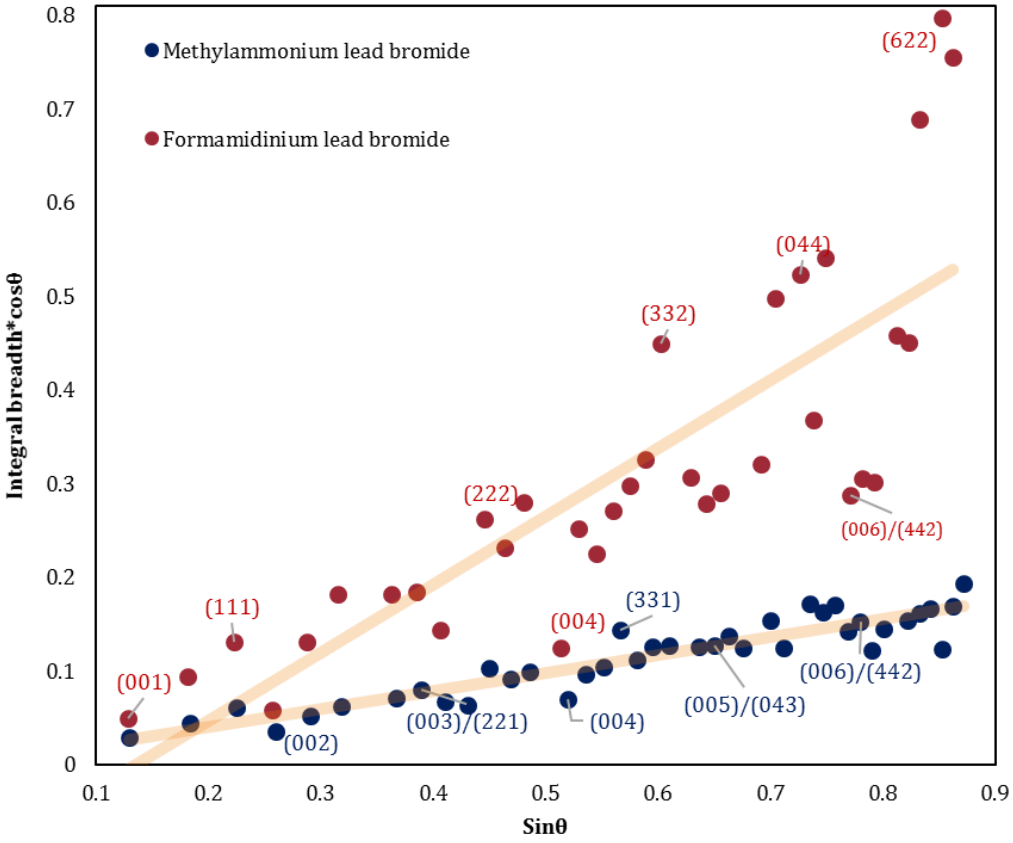

Figure 4-3 Williamson-Hall plot of $FAPbBr_3$ and $MAPbBr_3$ at room temperature; the slopes are a measure of the relative strains in the two systems. The integral breadth is defined as the ratio of the peak area and peak height.

From the Williamson-Hall plots obtained from laboratory PXRD patterns of $MAPbBr_3$ and $FAPbBr_3$ collected under ambient conditions up to 135° 2θ (Figure 4-3 (a)), peak broadening ascribed to microstrain is clearly the dominant factor in well-ground samples of these materials. Broadening due to size effects is very small (note the small intercept on y-axis) and hybrid lead bromide perovskites tend to form cubic crystallites with no significant size anisotropy. A higher average strain level was observed in $FAPbBr_3$ than its MA counterpart. This may be attributed to the large size of FA cation, since the high tolerance factor of $FAPbBr_3$ suggests that it sits at the edge of perovskite structural stability range. Interestingly, we observed that peaks are sharper for the (h00) peaks in both MA and FA samples. For example, the (002) and (004) peaks clearly lie below the line of best fit shown in Figure 4-3. Post-synthetic treatment was tested as a method to minimize the effects of strain. After annealing the samples at 100 °C for 4 hours, some isotropic thermal strains are induced but the observed anisotropic peak broadening features remained essentially the same, as shown in Figure 4-4. The consistent peak profile after temperature cycling suggests that the observed strains are due to intrinsic structural features.

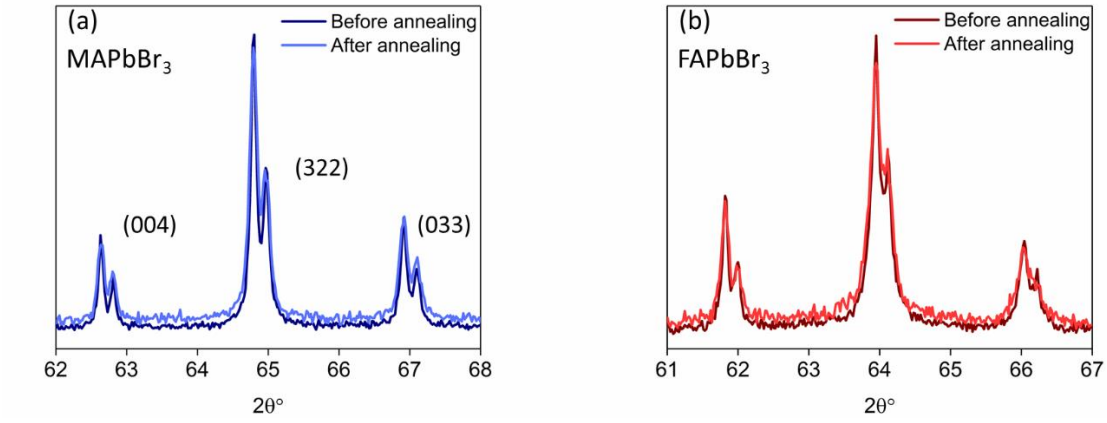

Figure 4-4 A representative section of the experimental PXRD pattern, starting from (004), of (a) $MAPbBr_3$ and (b) $FAPbBr_3$ before and after annealing at 100 °C for 4 hours. Consistent peak characteristics are observed after annealing. The peak splitting arises from Cu $K\alpha_1$ and α_2 radiation.

Rietveld refinement was carried out on both $MAPbBr_3$ and $FAPbBr_3$ using Topas using using the fundamental parameters approach and a full axial divergence model[139,140] and the refinement parameters were improved in both samples using the anisotropic peak broadening model, as shown in Figure 4-5. Improvements in refinement parameters were

observed, with the R_{wp} dropped from 9.85% to 4.95% for $FAPbBr_3$ and from 8.82% to 6.63% for $MAPbBr_3$ (excluding low angles below 20°).

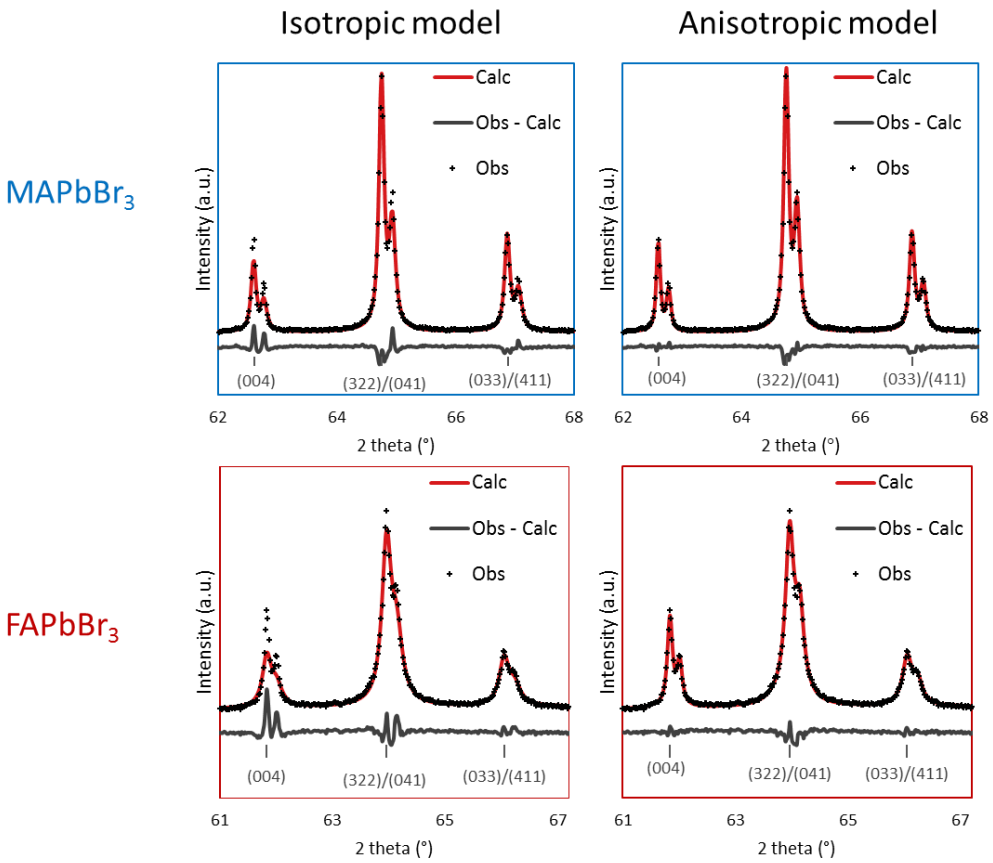

Figure 4-5 A representative section of Rietveld refinement of $MAPbBr_3$ and $FAPbBr_3$ with isotropic refinement and anisotropic strain broadening refinement. In both samples, observed peak profile of (004) is much sharper than the adjacent (041) and (033) peaks.

4.4 More quantitative analysis on $FAPbBr_3$

$FAPbBr_3$ exhibits large anisotropic strain and in order to better quantify its strain contribution to the peak profiles, synchrotron PXRD data ($\lambda = 0.80603$ Å) were collected for $FAPbBr_3$ at 290 K on beamline I11 at the Diamond Light Source (see Chapter 2 for experimental details). Rietveld refinements were carried out using Topas Academic Version 5.1[139] with both isotropic and anisotropic broadening models, as shown in Table 4-1.

Table 4-1 Rietveld refinement details of $FAPbBr_3$.

Formula	$CH_5Br_3N_2Pb$	
Strain model	Isotropic	Anisotropic
a (Å)	5.99248(10)	5.99193(8)
V (Å³)	215.189(11)	213.130(9)
R_p, R_{wp}	1.23%, 2.03%	1.00%, 1.37%
R_{Bragg}	2.24%	1.83%
Space group	$Pm\bar{3}m$	
Z	1	
$p_{cal.}$	3.76	
2θ range	6 to 60	
Diffractometer	I11, Diamond Light Source, Mythen	
Pb, xyz	0, 0, 0	
Br, xyz	-0.5, 0, 0	
Pb, $U_{11} = U_{22} = U_{33}$	0.0391(5)	0294(3)
Br, U_{11}, $U_{22}=U_{33}$	0.0090(15),0.1109(13)	0105(9),0.1139(9)

Note: the disordered organic cations are modelled as C (x =-0.5,y =-0.5, z =-0.5, occupancy 1) and N (x =-0.5, y =-0.656,z =-0.5, occupancy 0.33), according to the single crystal diffraction electron densities in Chapter 3 and refined with a maximum B_{iso} of 20.[201]

The model with isotropic broadening gave a reasonable refinement, but, it was a relatively poor fit compared to that obtained using Stephens' phenomenological model of anisotropic peak broadening,[197] as shown in the reduced differences between observed and calculated pattern (dark grey lines) in Figure 4-6 (a), (b) and (c). This is particularly noticeable at higher angles. For example, the isotropic refinement clearly underestimates the sharpness of the (004) peaks in Figure 4-6 (c). The observation that peaks for the (h00) were sharper than the (hh0) and (hhh) peaks indicates the presence of anisotropic broadening.

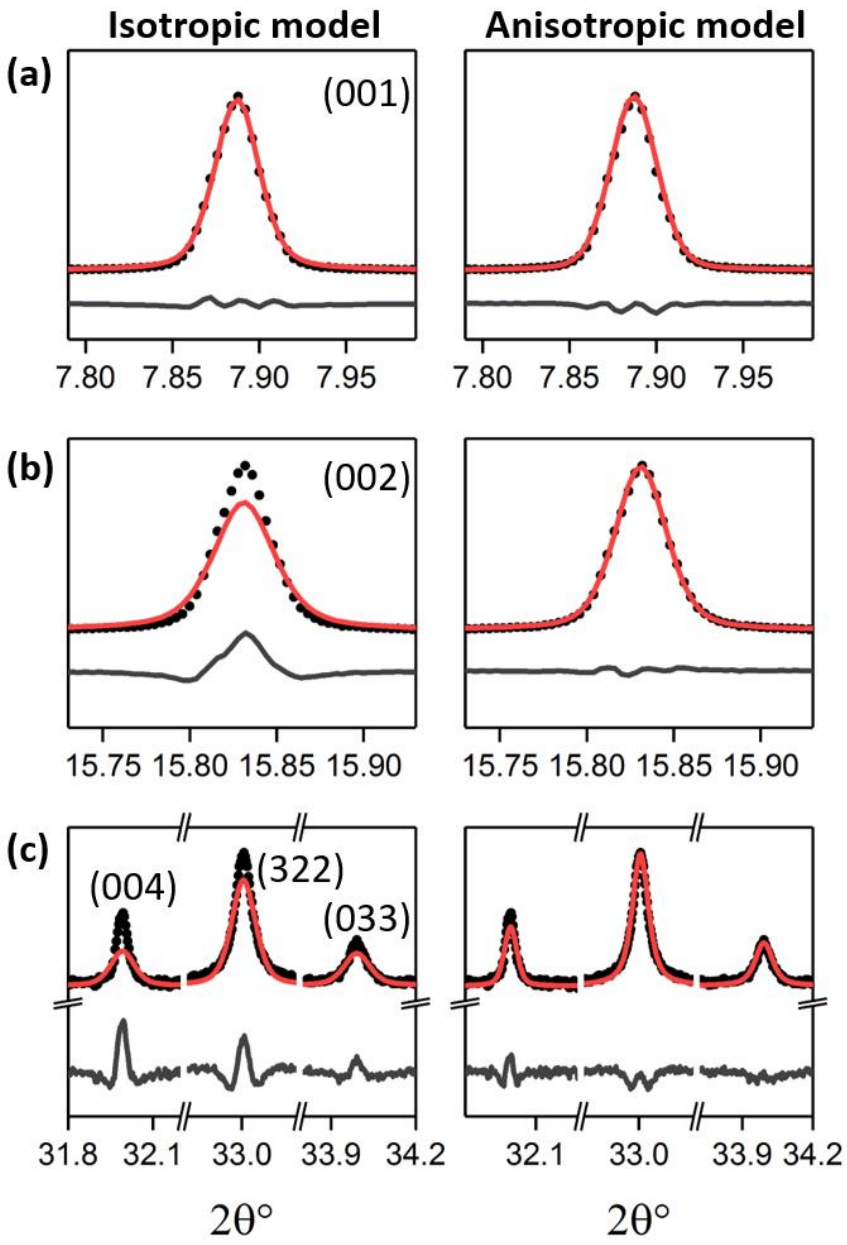

Figure 4-6 Rietveld refinement of $FAPbBr_3$ at 290 K was carried out using both isotropic and anisotropic broadening models, as shown in the left and right-hand columns in the figure. Representative sections of the refinements are shown for (a) (001), (b) (002) and (c) (004), (322)/(041) and (033)/(411) reflections, respectively. The black lines show the differences between the observed and calculated patterns.

In Stephens' formalism, anisotropic strain parameters, S_{HKL}, were introduced to measure the covariance of the distribution of peak widths.[197] Leineweber *et al*. further expanded the Stephens model with a physical meaning and an increase in S_{HKL} parameters can be interpreted as a broadening of the distribution of the lattice parameters.[202] The unscaled anisotropic strain parameters obtained from Topas for cubic symmetry, S_{400} and S_{220}

showed that S_{400} was around 26 time smaller than S_{220} at 290 K, which quantified the anisotropic strain broadening in the cubic phase of $FAPbBr_3$ (see Appendix Table-A 2). Figure 4-7 shows the full anisotropic Rietveld refinement of $FAPbBr_3$ with the Stephens model. Refinement for high angle reflections are shown in the inset.

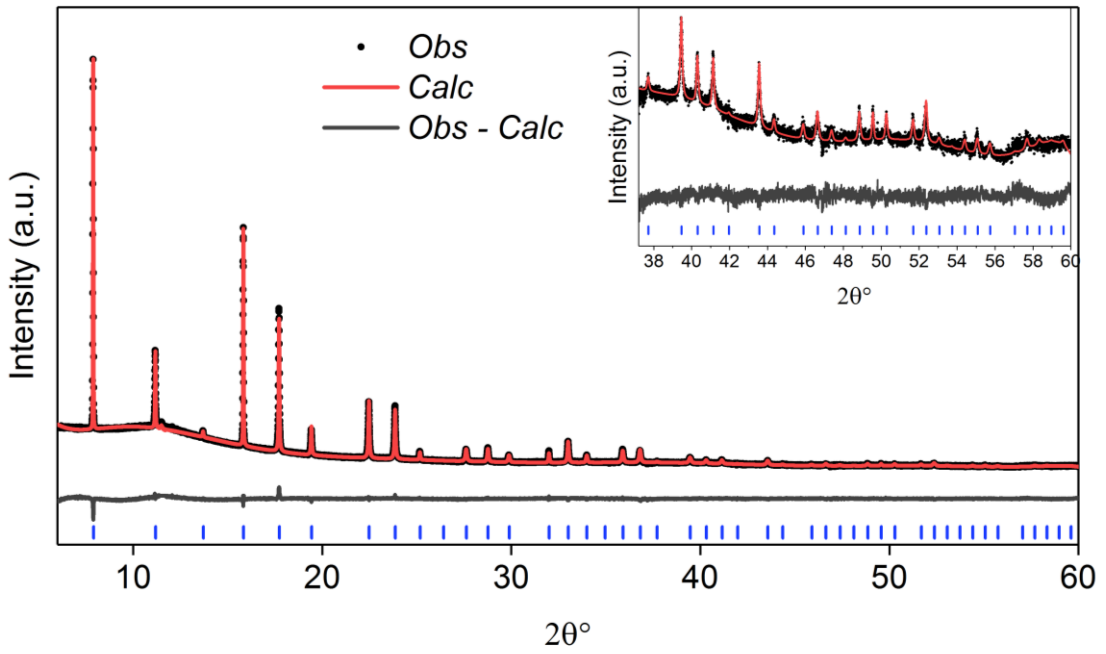

Figure 4-7 Full range of Rietveld refinement with anisotropic peak broadening, R_{wp} = 1.37% (the hump at low angle arises from the cream used to mount the sample).

The experimentally observed FWHMs of $FAPbBr_3$ are plotted as a function of 2θ° in Figure 4-8 (a). The data was extracted from Topas using the implemented Pseudo-Voigt profile function.[139,140] The monotonic increase in peak width with the diffraction angle refers to isotropic lattice strain and the sharper (h00) peaks in comparison to other peaks indicate the presence of the anisotropically strained lattice. This anisotropy and the

resultant variations in FWHMs are well captured in the Stephens' model, as shown in Figure 4-8 (b).

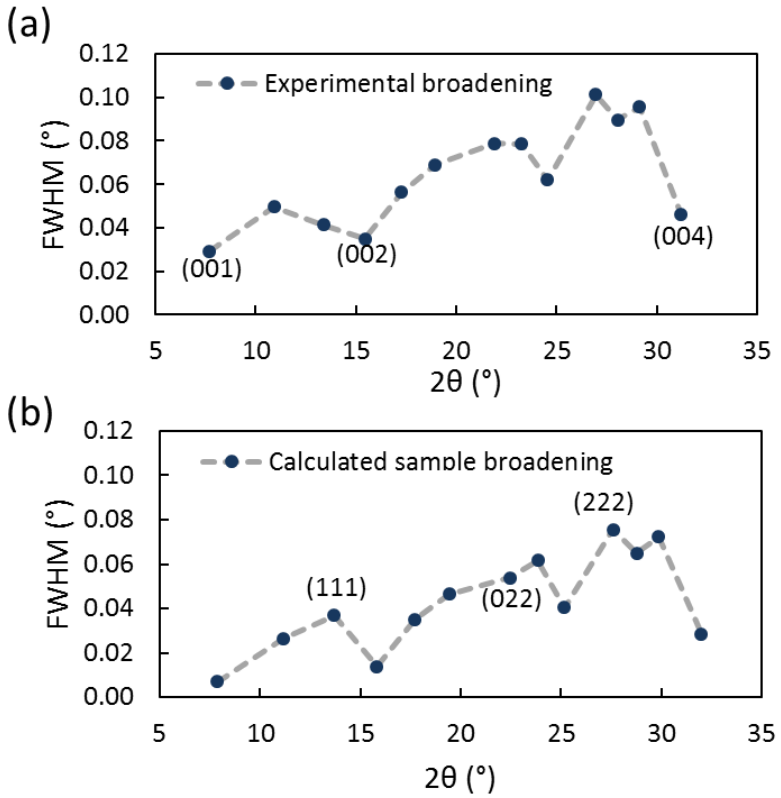

Figure 4-8 (a) Experimental observed FWHM of the synchrotron PXRD data on $FAPbBr_3$, revealing the sharper (h00) peaks. (b) Calculated sample peak profile assuming Lorentzian peak shape using Stephens' anisotropic strain broadening model.

Figure 4-8 (b) presents the calculated sample broadening, where anisotropic strain parameters were applied to the Lorentzian component of the peak function without the instrumental broadening (~0.02° from the 0.3 mm capillary used and ~0.004° from the detector).[141] The trend shown in the calculated peak widths are qualitatively comparable to the experimentally observed FWHMs. The Stephens model indicates that <hhh> is most strained direction while <h00> being the least strained. Interestingly, in our dataset collected at 290 K, the experimental peak profiles show that the FWHM of (011) > (111), whereas (022) < (222). This difference may be due to axial divergence at low angles or sample imperfections. The modelled three-dimensional strain field is visualised in Figure 4-9 using GSAS software by Dr. Yue Wu from the author's research group, showing the most strain along the <hhh> directions.[203] We were not able to obtain the strain field diagrams from the laboratory PXRDs, due to the instrumental influences. Interestingly,

our finding is supported by the recent PDF study by Seshadri *et al.*, where a local off-centering of Pb along <111> were observed.[192]

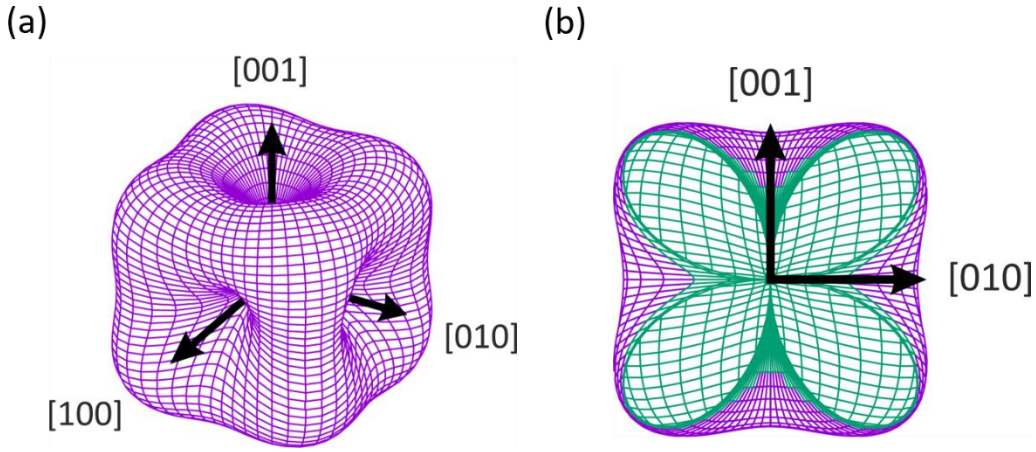

Figure 4-9 (a) The three-dimensional strain field plotted using GSAS and (b) its contour plot on (100) plane.

4.5 Origin of the strain

4.5.1 Lattice dynamics

A variety of factors could be responsible for the observed anisotropic features in the X-ray patterns of lead halide perovskites, but we shall argue that they are primarily a result of the interplay between the cation rotations at room temperature and the tilting of the inorganic framework due to the local off-centering instabilities of Pb and Br.

We first discuss the dynamics of the inorganic framework. Local distortions is common in halide HOIPs due to the soft and dynamic nature of the lead halide framework.[170] Using high energy resolution inelastic X-ray (HERIX) scattering, Beecher *et al.* recently reported the rotational instabilities of the PbI_6 octahedra in single crystal $MAPbI_3$, which were present at room temperature and above. The observed non-centrosymmetric, instantaneous symmetry-broken local structure was attributed to the combined effects of octahedral tilting, MA cation orientations and Pb off-centering.[131] Furthermore, recent PDF study on ABX_3 (A = MA or FA, B = Sn or Pb and X = Br or I) attributed these symmetry-lowering distortion phenomena to the dynamic off-centering of the lone pairbearing group IV metal.[192]

Regarding the structure of $FAPbBr_3$, as discussed in Chapter 3, Br anion shows anisotropic thermal parameters, forming highly oblate thermal ellipsoids that lie normal to the Pb-Br bonds seen in the SCXRD at room temperature (Figure 4-10). The local distortions of the Br anions and octahedral tilting, leading to local deviation of the Pb – Br – Pb angles away from 180° by up to 15°,[201] contributes to the local strains and hence the hkl-dependent peak broadening. Similar disc-shaped thermal ellipsoids have also been observed previously in $MAPbBr_3$.[170]

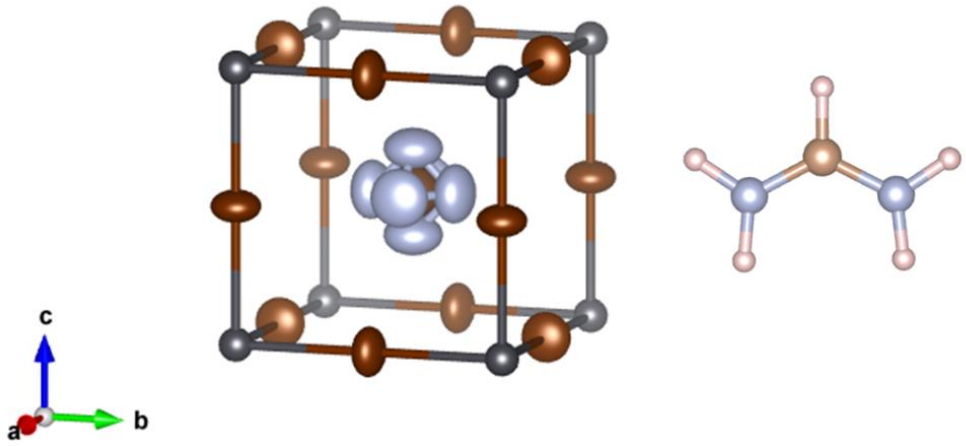

Figure 4-10 Crystal structure of the cubic lead bromide framework at room temperature with the disordered A-site cation in the middle of the cavity obtained from SCXRD (left). The structure of a FA ion is shown on the right. Key: dark brown spheres represent bromine, grey lead, blue nitrogen and light brown represent carbon. ADPs are shown with 50% probability.

The dynamics of the inorganic framework discussed above is closely related to the nature of the organic cations. Recent NMR study revealed that due to weaker hydrogen bonding, FA cations reorient faster than MA cations in both pure and mixed hybrid lead iodide phases.[204] To understand the role of the organic cation rotation underlying the anisotropic strain, we then explored the effect of cation dynamics on the $FAPbBr_3$ perovskite framework. It is believed that the Br positions are dynamic and distorted; however, Pb is the heaviest X-ray scatterer in the system. We therefore studied the effect of cation rotation on the Pb – Pb distance via DFT calculations (performed by Dr. Federico Brivio in the author's department).

In an ideal cubic cage, the FA cation can rotate freely, along three orthogonal axes oriented along the <h00> axes. In particular, we focused on the rotation along the axis parallel to the N-N direction of the FA cation. Rotation around this axis has the lowest

energy barrier because it does not significantly change the distance between the NH_2 groups and the halide,[184] and it is consisted with the proposed structural model for the tetragonal phase at lower temperatures (as discussed in Chapter 3). Starting from the cubic inorganic framework with the N – N axis of the FA cation lying along the <100> direction, we rotate the N-C-N plane along the N-N axis by 15°, 30° and 45°**,** respectively, as shown in Figure 4-11 (a). At each step, completely optimized structures were obtained (Figure 4-11 (b)). The different orientations of the molecule induce different tilting in the inorganic cage with a consequent variation in the inter-plane distances along different crystallographic directions. We can consider the final structures as representative of the local distortions that occur in the crystal. Deviations from the mean *d*-spacings along <001>, <011> and <111> are shown in Figure 4-11 (c) (computational methods are described in Chapter 2).

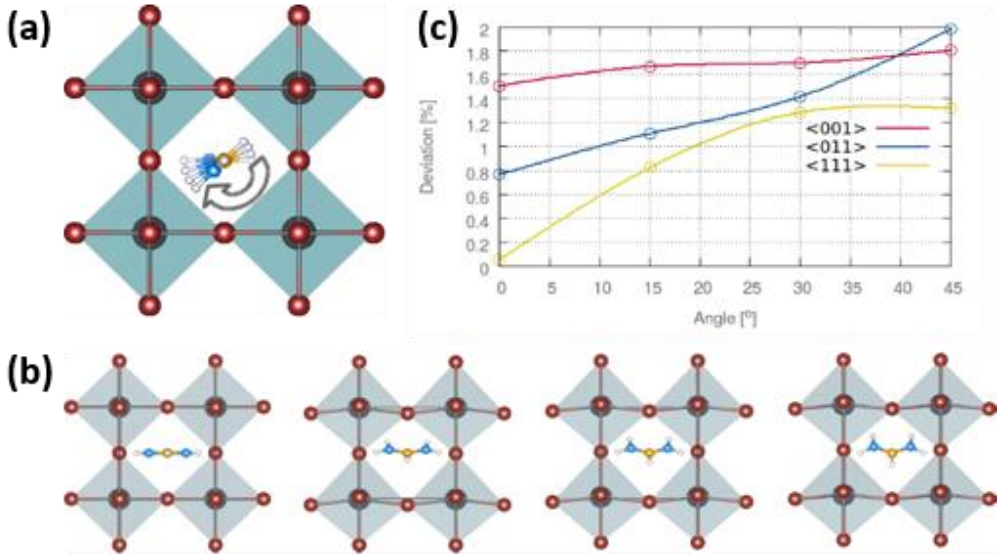

Figure 4-11 (a) Rotation of the molecule in the ideal cubic cage along N-N axis of the FA cation. (b) Optimized structure as a in function of the molecule rotations. It is possible to observe the rearrangement of the bromine atoms as a function of the molecule position and the distortion of the cell. (c) Standard deviation of the interplanar spacings with specific cation orientations from the mean d-spacing along the three directions <001>, <011> and <111>.

As seen in Figure 4-11 (c), interplanar spacings along <001> show the least changes as the rotation angle increases, consistent with the observations in the X-ray patterns. Although on average the cation is fully disordered and Pb vibrates in all directions, since

the molecule is not symmetric, neither is the local deformation of the octahedra and the local displacements of Br and Pb. The interplay between the disordered FA cation dynamics and the deformation of the Pb-Br perovskite cage leads to the breaking of local symmetry and hence contributes to the anisotropic broadening observed experimentally.

Following the observations of local symmetry breaking, it is necessary to understand the locations of the Pb and Br without crystallographic symmetry constraints. AIMD simulations were performed on $FAPbBr_3$ at 300 K based on experimental lattice parameters from SCXRD (simulations conducted by Zeyu Deng). The deviations of the Pb···Br bond distances away from their crystallographic average in the cubic symmetry confirmed the dynamic nature in $FAPbBr_3$. The computed interatomic distances of Pb···Br were compared with $MAPbBr_3$ using radial distribution function, as shown in Figure 4-12.

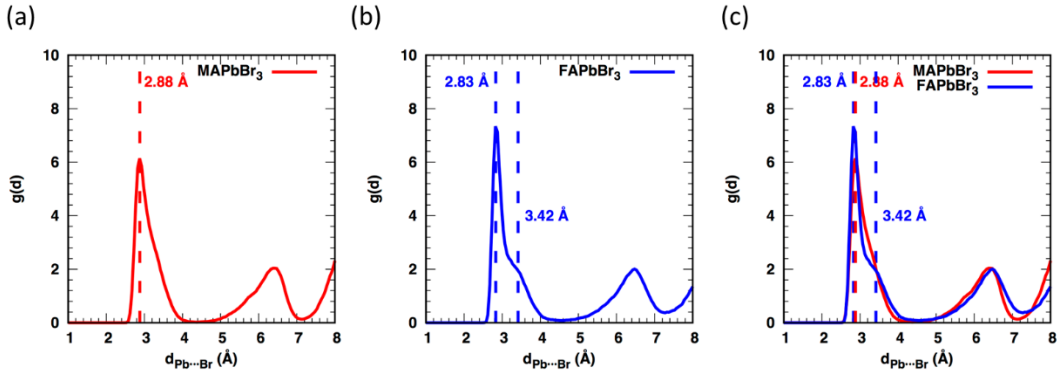

Figure 4-12 Computed radial distribution functions (g(d)) of (a) $MAPbBr_3$, (b) $FAPbBr_3$ and (c) their comparison for Pb···Br interatomic distances.

Interestingly, despite the fact that $FAPbBr_3$ has a larger unit cell, our computational study revealed that the closest Pb···Br interatomic distances are at around 2.88 Å for $MAPbBr_3$ and 2.83 Å for $FAPbBr_3$ respectively. It seems likely that lone pair effects associated with dynamical distortion of the $PbBr_6$ octahedra lead to a combination of shorter and longer Pb – Br bond lengths, as seen statically in tin halides.[205,206] The larger deviation between the crystallographic Pb – Br bond lengths and the computed closest Pb···Br interatomic distances in $FAPbBr_3$ indicate more structural distortions compared with its MA counterpart.

4.5.2 Microstructural defects

In addition to the modelled anisotropic strain field shown in the X-ray patterns, we observed direct evidence of lattice distortions in $FAPbBr_3$ using transmission electron microscopy (TEM). To confirm the presence of intrinsic lattice strain, as-synthesised polycrystalline samples were used at room temperature without any mechanical grinding or post synthetic treatment. Figure 4-13 (a) shows a representative lattice-resolved image of $FAPbBr_3$, seen along the along the <100> zone axis (credit to the Electron Microscopy Group, Department of Materials Science. The TEM images taken by Dr. Caterina Ducati, Stefania Cacovich and Christopher Magazzeni). The strong contrast modulation in the image can be interpreted as being associated with lattice distortions.

Moreover, several dislocations are visible (along <100>), one of which is highlighted by marking individual atomic planes in Figure 4-13 (b) and (d). Dislocations in halide HOIPs were previously observed in $MAPbBr_3$ using low-temperature scanning tunnelling microscopy, where the local structural defects were ascribed to the interplay of MA positions and Br anions.[199] We expect that microstructural defects also contribute to the strain field in $FAPbBr_3$. Due to the lack of stability of $FAPbBr_3$ under the electron beam, however, we were not able to obtain a full analysis of the dislocation type and density. The contribution of dislocations was not modelled in the X-ray peak profile discussed in this chapter, since the observed anisotropic characteristic was not altered by annealing (as previously discussed) and the Stephens' model of anisotropic strain broadening excludes the effects of microstructural defects. A separate model to quantify the effect of dislocations on X-ray peak broadening and to further understand the defect-induced strain in HOIPs will be interesting for future studies.

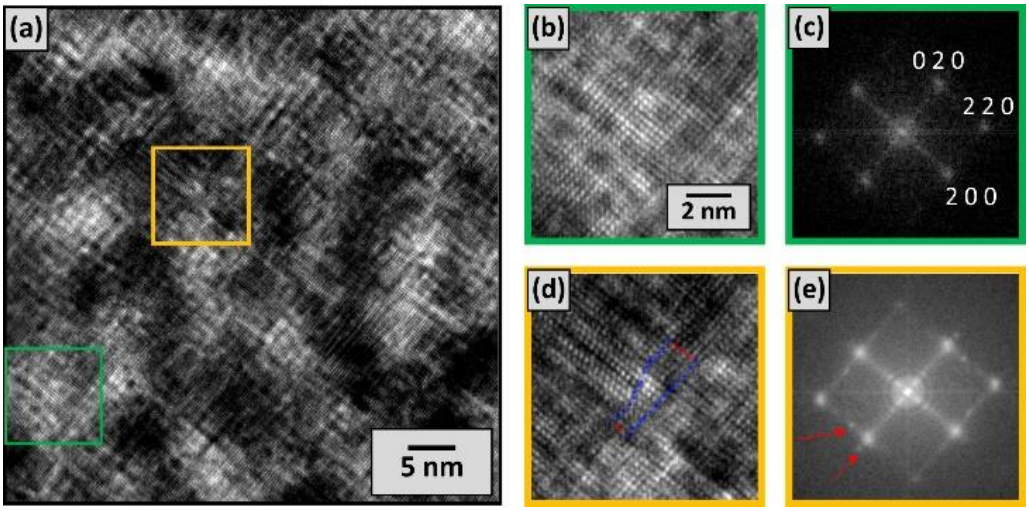

Figure 4-13 (a) Bright Field HRTEM image of FAPbBr3 acquired along the <100> zone axis. The high magnification images in (b) and (d) show a crystalline region with no visible line defects, and one where a dislocation is present (highlighted in (d)). c) and e) show the corresponding FFTs. In the presence of lattice distortions, extra diffraction spots (red arrows) are visible.

4.6 Conclusions and future work

PXRD profile analysis was used in this study to examine the anisotropic features of hybrid lead bromide perovskites in a quantitative manner. Comparative studies on MA- and FA-based lead bromide reveal relatively large intrinsic strains in $FAPbBr_3$. Synchrotron PXRD was performed on $FAPbBr_3$ to examine its strain field and <100> was shown to be the least strained direction. We rationalize the intrinsic strain from the perspective of the dynamic off-centering of Pb and Br as well as their interactions with the organic cation. These differences contribute to the differences in device performance.

It is shown in this work that HOIPs exhibit a complex relationship between the lattice symmetry and the atomic coordinates. One future possibility for the anisotropic strain model is to analyse the mixed cation and halide systems. A recent study on MA based perovskites showed the partial immobilization of organic cations in mixed halide alloys, highlighting the importance of local symmetry breaking.[207] With anisotropic strain parameters, our proposed methods can be used to investigate the structural effects of lattice distortions, since it has been difficult to perform quantitative structural analysis for mixed cation and halide perovskites with traditional materials characterisation techniques.

Chapter 5 Mechanical properties of single and double perovskites

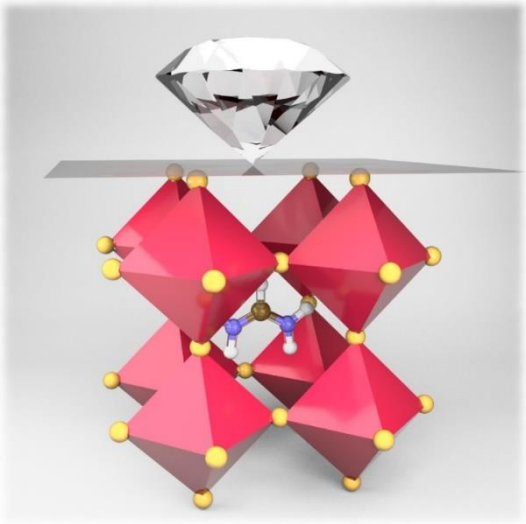

In this chapter, the mechanical properties of single crystal Pb-based halide perovskites and Bi-based double perovskites were probed by nanoindentation. The measured Young's moduli (10–20 GPa) and hardnesses (0.26 -0.52 GPa) were related to the underlying crystal structures in which the influences of inorganic bond strengths, packing density and hydrogen bonding were discussed respectively with the support of DFT calculations. The systematic study of the mechanical behaviour allows us to explore the effect of compositional engineering on the elastic and plastic response of the halide HOIPs.

Some of the results in this chapter have been published in:

- **S. Sun**, Y. Fang, G. Kieslich, T. J. White and A. K. Cheetham, "Mechanical properties of organic-Inorganic halide perovskites, $CH_3NH_3PbX_3$ (X=I, Br and Cl), by nanoindentation", *J. Mater. Chem. A*, 2015, **3**, 18450-18455.
- F. Wei, Z. Deng, **S. Sun**, F. Xie, G. Kieslich, D. M. Evans, M. A. Carpenter, P.D. Bristowe, and A. K. Cheetham, "The synthesis, structure and electronic properties of a lead-free hybrid inorganic–organic double perovskite $(MA)_2KBiCl_6$ (MA= methylammonium)", *Mater. Horiz.*, 2016, **3**, 328-332.
- Z. Deng, F. Wei, **S. Sun**, G. Kieslich, A. K. Cheetham and P.D. Bristowe, "Exploring the properties of lead-free hybrid double perovskites using a combined computational-experimental approach", *J. Mater. Chem. A*, 2016, **4** 12025-12029

- F. Wei, Z. Deng, **S. Sun**, F. Zhang, D. M. Evans, G. Kieslich, D. M. Evans, S. Tominaka, M. A. Carpenter, J. Zhang, P.D. Bristowe, and A. K. Cheetham, "The synthesis and properties of a lead-free hybrid inorganic–organic double perovskite $(CH_3NH_3)_2AgBiBr_6$", *Chem. Mater.*, 2017, **29**, 1089-1094.
- **S. Sun**, F. H. Isikgor, Z. Deng, F. Wei, G. Kieslich, P. D. Bristowe, J. Ouyang and A. K. Cheetham, "Factors influencing the mechanical properties of formamidinium lead halides and related hybrid perovskites", *ChemSusChem*, 2017, accepted manuscript.

5.1 Overview

One of the advantages of the HOIPs compared to their inorganic counterparts is that the dynamical and soft nature of the hybrid framework provides further possible applications in flexible and wearable functional devices.[125,127,208] As a consequence, the mechanical stability and deformation behavior of hybrid perovskites are attracting increasing attention.[124] However, despite the rapid progress in the study of the physical properties and electronic structures,[21,37,45,209,210] few theoretical and experimental investigations of their mechanical properties of lead halide hybird perovskites were reported.

5.1.1 Recent reports on mechanical stability of halide perovskites

A recent computational study on the fracture of $MAPbI_3$ revealed that it is more compressible and ductile than inorganic perovskites, indicating its potential suitability for wearable devices.[124] Some DFT calculations on $MABX_3$ (B = Pb, Sn and X = I or Br) were firstly conducted in 2014.[123] Shortly after, we reported the first experimental study of the mechanical property measurements on similar compositions $MAPbX_3$ (X = I, Br or Cl) and since then, several reports on the mechanical properties of Cs/MA-based lead halide were published, revealing Young's moduli of 10 – 20 GPa.[211–213] To the best of our knowledge, however, there have not been any systematic studies on the elastic properties or deformation behaviour of FA-based halide perovskites.

The measurement of the elastic and plastic responses of hybrid framework materials is challenging since high sample quality and novel characterization techniques are required.[114,117,214,215] Nanoindentation provides a reliable way of probing the anisotropic mechanical behaviour since the measured stiffness is strongly dependent on the elastic response along the indenter axis and only weakly affected transversely.[115] Quantitative characterization of the mechanical properties for a range of crystalline hybrid frameworks has been made in the last decade employing the nanoindentation technique on single crystals. For example, recent work on the formate perovskites with different A-site organic cations suggested that the hydrogen-bonding interactions between the protonated amine and the formate framework crucially influence the elastic responses.[121]

5.1.2 Purpose of the present study

In this study, we aimed to determine the mechanical properties of the hybrid perovskite systems and to understand the effects of compositional engineering on their mechanical response. By comparing our results of nanoindentation studies on $MAPbX_3$ (X = I, Br or Cl) and $FAPbX_3$ (X = I or Br) single perovskites,[211–213] as well as on $(MA)_2MBiX_6$ (M = K, Tl or Ag and X = Br or Cl) double perovskites,[99–101] we were able to assess the mechanical effects of making substitutions on the A, B and X sites. The underlying reasoning of the different elastic and plastic responses were rationalised with the support from DFT and AIMD calculations.

5.2 Mechanical properties of $MAPbX_3$ (X = I, Br or Cl)

At the room temperature, $MAPbCl_3$ and $MAPbBr_3$ adapt the cubic space group of $Pm\bar{3}m$, whereas $MAPbI_3$ is tetragonal in the space group of $I4/mcm$. The phase transition temperature from tetragonal to cubic is 57 °C for $MAPbI_3$. Figure 5-1 shows the typical $MAPbX_3$ crystals under the camera of single crystal diffractometer after face indexing.

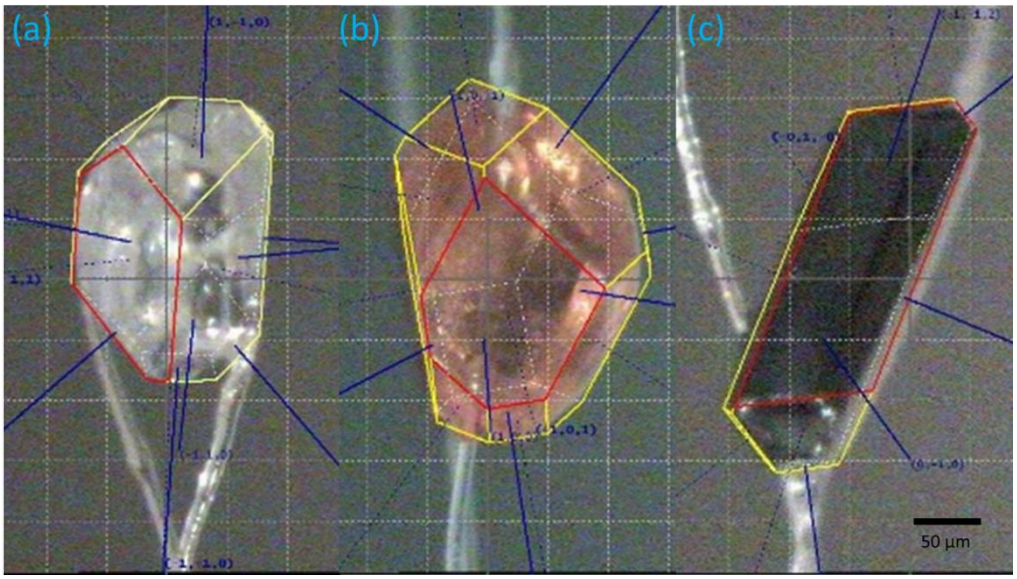

Figure 5-1 Photographs of representative face-indexed single crystals, (a) $MAPbCl_3$, (b) $MAPbBr_3$ and (c) $MAPbI_3$.

5.2.1 Elastic and plastic response

Young's moduli and hardness values of the $MAPbX_3$ crystals averaged from surface penetration depths between 200 nm and 980 nm are presented in Table 5-1. The overall results reveal that, at room temperature, the elastic moduli of $MAPbX_3$ (X=I, Br and Cl) single crystals vary in the range 10.4 – 19.8 GPa and a general trend of $E_{Cl} > E_{Br} > E_I$ is observed. In addition, E_{100} is greater than E_{110} for the cubic bromide and chloride cases.

Table 5-1 Experimental and theoretical values of the elastic modulus and hardness anisotropy of the $MAPbX_3$ (X=I, Br and Cl) perovskites.

Crystal	Orientation	Young's Modulus(*E*) (GPa)**	Theoretical Modulus (*E*) (GPa)[123]	Hardness (*H*) (GPa)
$MAPbI_3$	(100)*	10.4 ± 0.8	Tetragonal: 12.8	0.42 ± 0.04
Tetragonal	(112)*	10.7 ± 0.5	Cubic: 22.2	0.46 ± 0.06
$MAPbBr_3$	(100)	17.7 ± 0.6	Tetragonal: 15.1	0.31 ± 0.02
Cubic	(110)	15.6 ± 0.6	Cubic: 29.1	0.26 ± 0.02
$MAPbCl_3$	(100)	19.8 ± 0.7	No values reported	0.29 ± 0.02
Cubic	(110)	17.4 ± 0.7		0.25 ± 0.02

* The (100) and (112) planes in a tetragonal lattice are parallel to (110) and (101) planes, respectively, in the case of a cubic lattice.

** Values are obtained as average of more than 10 indents in each indentation experiment and errors are the calculated standard deviations. The variations between each measurement include the systematic error of the indenter and random errors from sample preparation procedures.

The Young's moduli were averaged over 10-20 indentations on each crystal it was plotted as a function of indentation depths using the Oliver-Pharr method,[146] as shown in Figure 5-2 (a). The experimental results were in reasonable agreement with the theoretical calculations on the mechanical properties (Table 5-1).[123] $MAPbI_3$ showed very good consistency with calculations for the tetragonal system. For $MAPbBr_3$, however, although the crystals were cubic, the measured Young's Modulus was closer to the theoretical predictions for the tetragonal phase.

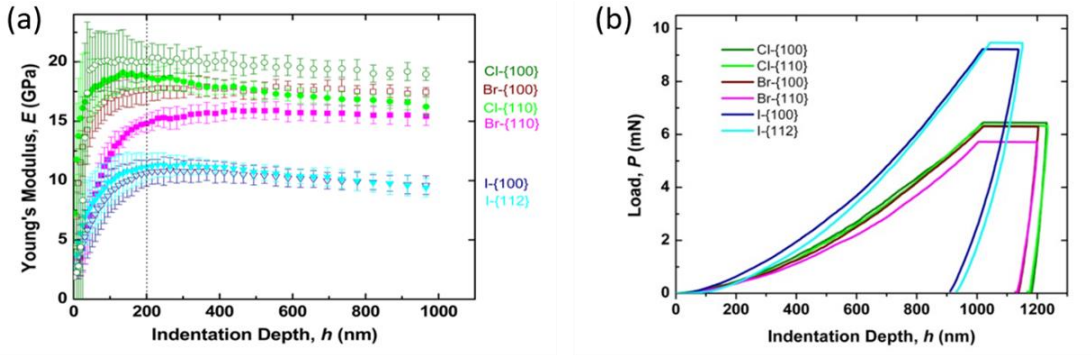

Figure 5-2 (a) Elastic moduli averaged over at least 10 indents on each crystal as a function of the indentation depth. (b) Typical load-displacement curves of different facets of $MAPbX_3$ (X = I, Br and Cl). Key: $MAPbCl_3$: light and dark green, $MAPbBr_3$: pink and brown, $MAPbI_3$: light and dark blue.

Typical load-displacement (*P-h*) curves illustrates the stress states of $MAPbX_3$ (X = I, Br, or Cl) as the indenter penetrates the sample surfaces (Figure 5-2 (b)). The gradient of the initial unloading sections of the *P-h* curves provides an indication of the elastic moduli. During unloading, an elastically strained material relaxes back to its original shape; however, the presence of the plastic zone leads to a residual impression on the sample surface after the load is completely removed.[121,216] All the *P-h* plots, especially $MAPbBr_3$ and $MAPbCl_3$, exhibit large residual depths from unloading, indicating that significant plastic deformation occurred underneath the Berkovich tip. The halide HOIPs may therefore potentially be able to facilitate applications in compliant devices that demand plastic deformations. $MAPbI_3$, however, show better elastic recovery, indicated by the smaller residue displacement after unloading.

The measured mechanical anisotropy within each halide system can be linked to the underlying crystal structure. As illustrated in Figure 5-3, along <100> directions of the cubic perovskite crystals, the indentation was aligned with the Pb-X-Pb inorganic direction, hence there is a strong resistance from the inorganic bonds. When the uniaxial pressure pushes along the <110> direction in the cubic system, the indenter moves against the face diagonal of the inorganic lattice, which is less rigid and generates more displacement, in agreement with the experimental results of lower moduli. Since the iodide perovskite is tetragonal at the room temperature, the indented (100) and (112) facets are are equivalent to (101) and (110) in a cubic cell. These two facets reveal similar values for the Young's modulus, as shown in Table 5-1. No other facets were found

suitable for the nanoindentation experiment. In the tetragonal structure, a tilting of the PbI_6 octahedra of 16.4° at 293K, as well as a ferroelectric off-centering along the *c*-axis, have been observed.[66] The tilting of the octohedra might lead us to expect less anisotropy in the Young's modulus than for the chloride and bromide because the Pb-I-Pb chains are no longer linear. Unfortunately, we were unable to observe this effect due to the absence of suitable crystal facets.

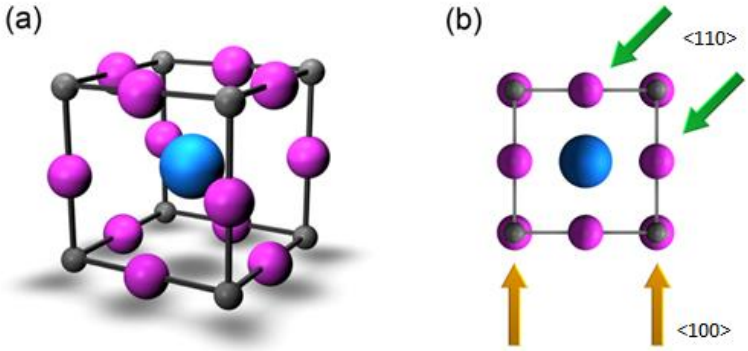

Figure 5-3 (a) Idealised representation of the perovskite crystal structure of $MAPbX_3$ (X=I, Br and Cl), (b) Illustration of nanoindentation along <100> (yellow arrows) and <110> (green arrows) directions in a cubic phase crystal. Grey: lead, purple: halide, blue: MA cation.

In addition to the elastic response, plastic deformation plays an important part in understanding the behaviour of materials under stress. Another physical property, hardness, which is crucial for any industrial applications that might involve the $MAPbX_3$ perovskites, was therefore investigated. The hardness results from the combination of elastic and plastic deformations taking place in the vicinity of the nanoindenter tip.[217] Based on the Oliver and Pharr method, the hardness value was calculated by dividing the applied load (P) by the surface contact area developed under that load (A_c). It can clearly be seen in Figure 5-4 that I-based perovskites require a much higher load to achieve the same displacement as their Br and Cl counterparts. Rather surprisingly, a trend of $H_I > H_{Br} > H_{Cl}$ has been observed, as shown in Table 5-1, with $MAPbBr_3$ and $MAPbCl_3$ perovskites showing rather similar values. Since hardness is a measure of the dislocation interactions in the plastic zone in response to the induced pressure from the tip, $MAPbI_3$ perovskites may show a higher hardness as a result of the lower symmetry of the structure. Multiple slip systems can be activated simultaneously to accommodate plastic flow for high-symmetry cubic crystals, whereas fewer dislocation systems may be active in tetragonal systems.[114] Similar conclusions on the activation of dislocations were made by

Reyes-Martinez *et al.* in the recent studies of the time-dependent mechanical response of Cs- and MA-based halide perovskites.[213] The high hardness and low elastic modulus of the $MAPbI_3$ perovskites mean that, although it is the least resistant to elastic deformation, it is superior to its Br- and Cl-based counterparts in resisting plastic deformation. Regarding the hardness anisotropy between different crystallographic orientations of the Cl and Br systems, it is less significant than the elastic anisotropy. However, it was observed that the facets having higher stiffness also tend to show greater hardness, reflecting the stronger bonding along particular crystallographic orientations.

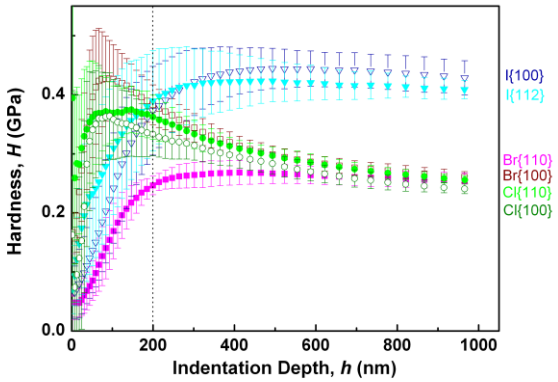

Figure 5-4 Hardness as a function of the indentation depth (Each curve was obtained from one representative crystal).

5.2.2 Effect of X-site halide on mechanical response

In order to understand the trend in mechanical response in terms of the bonding within the different structures, we now discuss three chemical factors that might influence the mechanical behaviour of these hybrid perovskites: (i) the Pb-X bond strengths, (ii) the packing density, and (iii) hydrogen-bonding between the MA cations and the halide anions. The Pb-X chemical bonding is believed to be an important factor in determining the physical properties of the lead halides.[218] As shown in Figure 5-5 (a),[219] the increasing Pb-X bond strengths in the sequence $E_I < E_{Br} < E_{Cl}$ correlates well with the increasing Young's moduli. Secondly, the relative packing densities should also influence the mechanical properties, and here we use the Goldschmidt's tolerance factor $t = (r_A + r_X)/\sqrt{2}(r_B + r_X)$, where r is the radius of the ion, to reflect the trend in packing densities.[102,220] The tolerance factors for $MAPbX_3$ (X = I, Br, Cl) are estimated as, I: 0.91, Br: 0.93, and Cl: 0.94, respectively.[6]

Figure 5-5 (b) reveals that the packing densities, as represented by the tolerance factors, correlate nicely with the Young's moduli, suggesting that the more densely packed structures are more resilient to elastic deformation. Hydrogen-bonding interactions between the A-site cation and the framework are known to have a strong influence on the mechanical properties of metal-organic formate perovskites,[120,121] and recent DFT calculations on the orthorhombic phase of $MAPbI_3$ emphasised the effect of the strength of the hydrogen-bonding on the octahedral tilting.[68] Since it is well known that strong hydrogen bonding correlates with greater electronegativity of the acceptor atom, it is not surprising to find that the Young's modulus increases with anion electronegativity in the sequence $E_I < E_{Br} < E_{Cl}$ (Figure 5-5 (c)).[221]

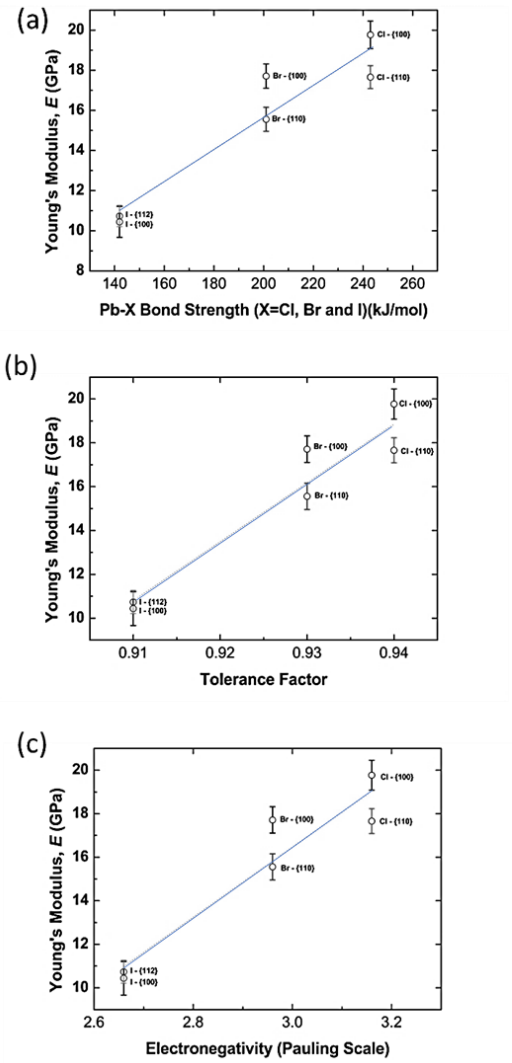

Figure 5-5 Young's Modulus as a function of (a) bond Strength[219] (b) Tolerance factor[6] (c) Electronegativity.[221] All the three chemical factors point to the same direction, although it is challenging to estimate their relative importance (the dotted blue lines are to guide the eye) .

The trend in the Young's moduli of the $MAPbX_3$ phases correlates well with all the chemical factors that are expected to influence it. At the same time, however, this leads to an ambiguity because we are unable to ascertain which of the three factors has the greatest effect on the stiffness of the system. Although being distinct, the three factors are also to some extent interrelated (for example, they are all influenced by the anion size).

5.3 Mechanical Properties of $FAPbX_3$ (X = I or Br)

Both $FAPbI_3$ and $FAPbBr_3$ adopt the cubic ABX_3 perovskite architecture at room temperature with space group $Pm\bar{3}m$ (Figure 5-6). Initially, the crystal structure of $FAPbI_3$ was thought to be trigonal (space group $P3m_1$[66]), but this view was recently revised to cubic based on neutron diffraction measurements.[172] As discussed in Chapter 3, the perovskite frameworks consist of corner sharing $[PbX_6]$ octahedra, forming a three-dimensional inorganic network with the organic cation located in the A-site cavities. When the symmetry is cubic, the Pb-X-Pb bond angle is 180°.

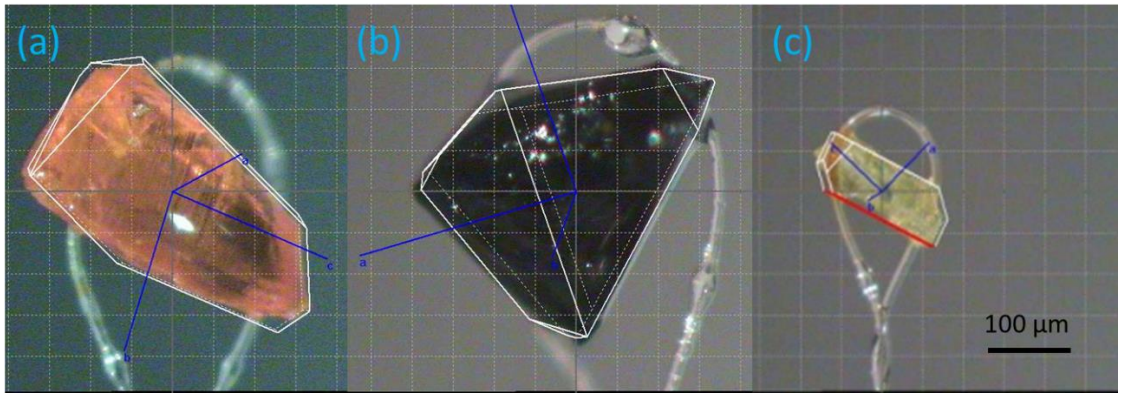

Figure 5-6 Photographs of representative face-indexed single crystals, (a) $FAPbBr_3$, (b) $FAPbI_3$ – perovskite (α phase) and (c) $FAPbI_3$ – one dimensional chain (δ phase).

5.3.1 Elastic and plastic response

The nanoindentation experiments were conducted on the X-ray detectable facets of $FAPbI_3$ and $FAPbBr_3$ single crystals up to an indentation depth of 1000 nm, as shown in Figure 5-7 (a) and (b). Both $FAPbI_3$ and $FAPbBr_3$ show anisotropy in their stiffness with the overall Young's moduli ranging between 9 GPa and 13 GPa. The perovskite structures

are stiffest along the inorganic Pb-X-Pb chains, which are aligned along <100>. Unlike our previous findings with the MA analogues, where $MAPbBr_3$ is significantly stiffer than $MAPbI_3$, the Young's moduli and hardnesses of $FAPbI_3$ and $FAPbBr_3$ are not significantly different.

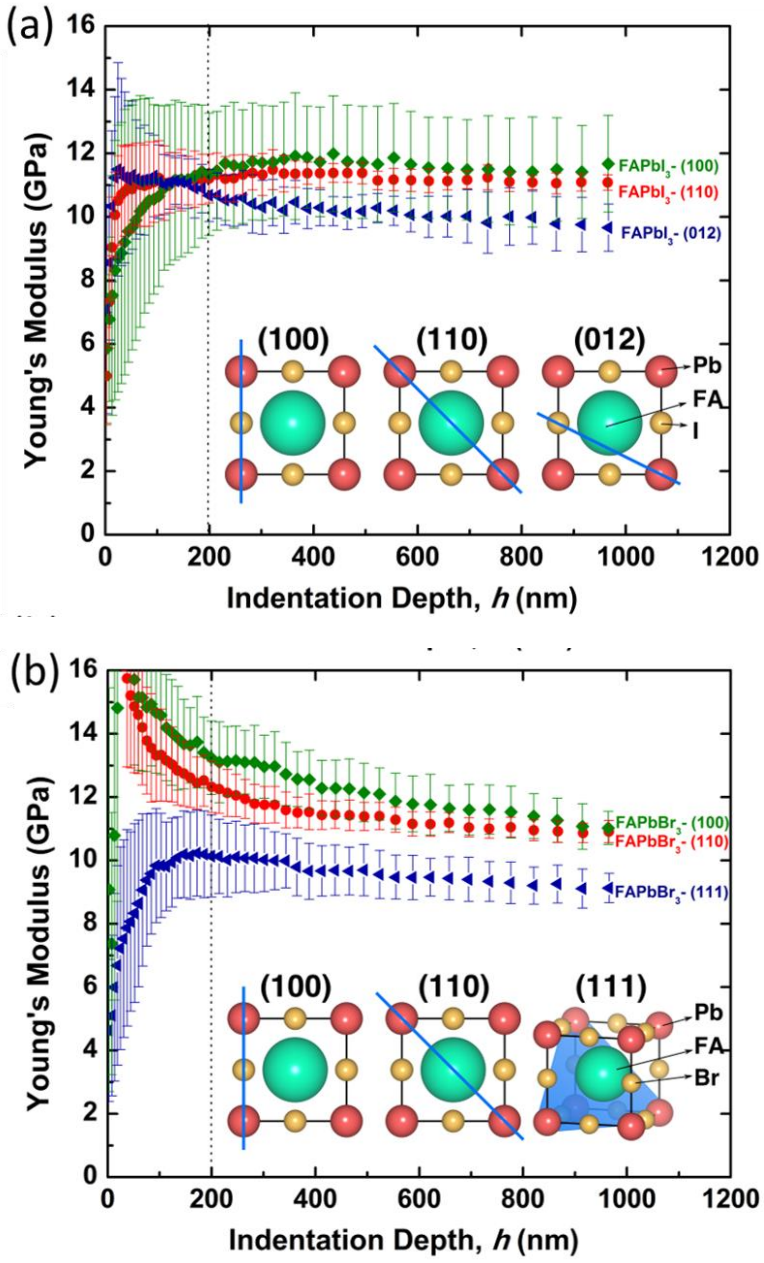

Figure 5-7 (a) Young's moduli of cubic $FAPbI_3$ as a function of indentation depth. Indentations were conducted on (100), (110) and (012) facets and these planes are highlighted in blue on the unit cells. (b) Young's moduli of cubic $FAPbBr_3$ as a function of indentation depth with indentations conducted on (100), (110) and (111) facets. The Young's modulus obtained at each point is the average of at least 10 individual indents and the standard deviations are shown with error bars.

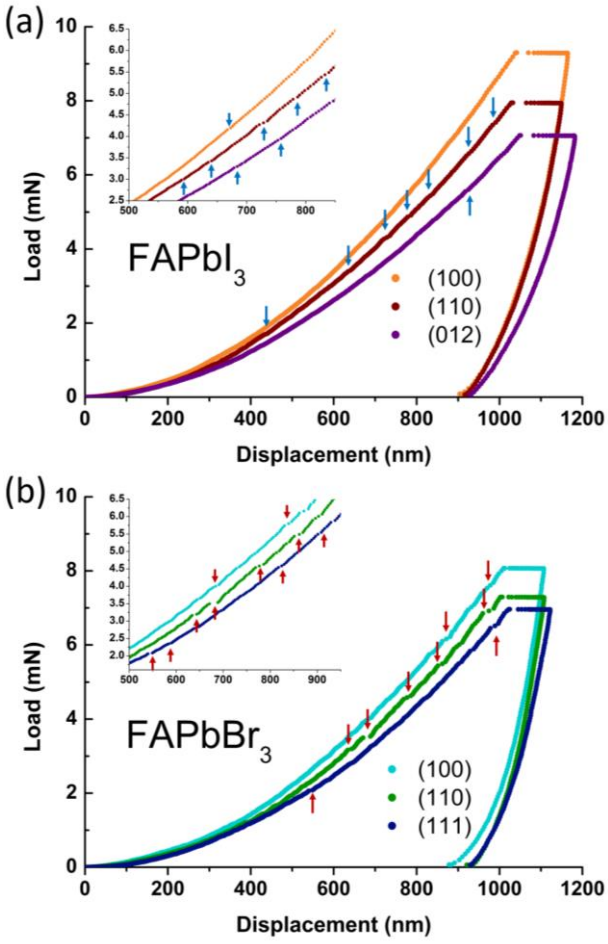

Figure 5-8 Typical load-displacement curves for (a) cubic $FAPbI_3$ and (b) cubic $FAPbBr_3$. Sections of the loading curves are enlarged and presented in the insets. Pop-in events, shown as discontinuities in the loading curves (marked using blue and red arrows for $FAPbI_3$ and $FAPbBr_3$ respectively), are observed in both perovskites, suggesting a series of dislocation nucleation events and associated hydrogen bond breaking. Pop-in events are more pronounced in the bromide perovskite than in the iodide.

Interestingly, the load–displacement curves for $FAPbI_3$ and $FAPbBr_3$ show discontinuities, as illustrated in Figure 5-8. Similar discontinuities (pop-ins) have been observed previously in organic-inorganic formate perovskites where they were attributed to the breaking of hydrogen bonds.[114,118,217] Recently, Reyes-Martinez *et al*. reported the time- and rate-dependent creep behaviour of MA- and Cs-based perovskites.[213] They credited the first pop-in positions to the onset of dislocation-led plastic deformation during the indentation. The observed plastic deformation indicates good ductility in these hybrid perovskite systems. Crystallizing in the cubic space group $Pm\bar{3}m$, both $FAPbBr_3$ and $FAPbI_3$ are expected to slip most easily on the {110} <111> slip system. This is

consistent with our observation that the most frequent and strongest pop-in events are seen on the (110) plane (see Figure 5-8 insets). On the other hand, the results of the hardness show a less clear trend as the differences between the facets are within the standard deviations (see Figure S2, ESI). It is seen in Figure 2 that the more pronounced pop-in events occur in $FAPbBr_3$ suggesting that it takes more energy to break the hydrogen bonds in the bromide rather than the iodide due to the higher electronegativity of the bromine ion.

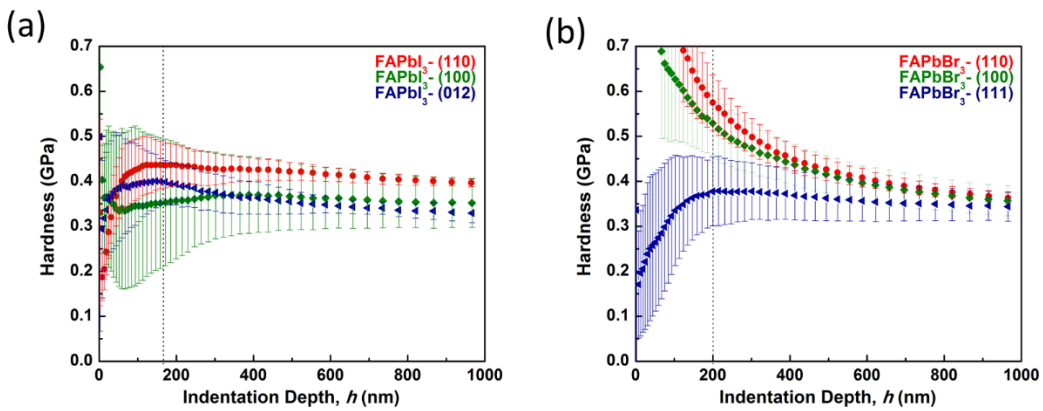

Figure 5-9 Hardness as a function of indentation depth for (a) cubic $FAPbI_3$ and (b) cubic $FAPbBr_3$.

One significant feature observed in cubic $FAPbI_3$ is a change in properties as it undergoes a phase transition from a perovskite to a non-perovskite structure. The black cubic phase of $FAPbI_3$ is metastable at room temperature and transforms to a yellow hexagonal one-dimensional chain structure within a few days.[66] This hexagonal phase adopts space group $P6_3mc$ and forms chains of face sharing octahedra along [001] with the FA cations located between the inorganic chains. Leaving our perovskite crystals at ambient conditions for two weeks yielded the hexagonal polymorph with poor crystal quality (see Figure S1, ESI). The elastic response measured from the freshly synthesized hexagonal phase showed that the inter-chain stiffness is lower than the three-dimensional framework, with a Young's modulus of 8.2 GPa normal to (120) (Figure 5-3). We were unable to make measurements along the chain direction.

Table 5-2 Mechanical properties of $FAPbX_3$ (X = I, Br).

Crystal	Orientation	Young's Modulus (GPa)	Hardness (GPa)
$FAPbI_3$ Cubic	(100)	11.8 ± 1.9	0.37 ± 0.10
	(110)	11.3 ± 0.7	0.40 ± 0.05
	(012)	10.2 ± 0.5	0.36 ± 0.03
$FAPbBr_3$ Cubic	(100)	12.3 ± 0.8	0.43 ± 0.04
	(110)	11.5 ± 0.4	0.45 ± 0.03
	(111)	9.7 ± 0.8	0.36 ± 0.05
$FAPbI_3$ non-perovskite, hexagonal	(120)	8.2 ± 1.3	0.20 ± 0.02

5.3.2 Effect of A-site cation on mechanical response

We now consider the effect of the FA cation on mechanical properties. In the literature, the influence of the A-site cation is still a topic of discussion with previous reports suggesting that the organic molecule in a hybrid perovskite simply acts to balance the charge and fill the space inside the 12-fold cavity and contributes little to mechanical behavior.[213]

Table 5-3 Experimental crystal structure and properties of $APbX_3$ (A = MA, FA, X = Br, I).

	Space group	Density (g/cm^3)	Tolerance Factor[6]	Pb-X distance
$FAPbBr_3$	$Pm\bar{3}m$	3.75	1.008	2.998
$MAPbBr_3$	$Pm\bar{3}m$	3.81[170]	0.927	2.966[170]
$MAPbI_3$	$I4/mcm$ $(I4cm, Fmmm)$	4.18[170]	0.912	3.146 -3.199[170]
$FAPbI_3$	$Pm\bar{3}m$	4.09[101]	0.987	3.178[101]

It is important to mention that the mechanical properties of $FAPbI_3$ are not readily compared to those of $MAPbI_3$ due to their different crystallographic symmetries at room temperature (Table 5-3). The unit cell of cubic $FAPbI_3$ is larger than that of tetragonal $MAPbI_3$ at room temperature, but the Pb-I bond lengths are very similar in both structures. From consideration of the Pb-I-Pb bond angles, the octahedral tilting in $MAPbI_3$ is

expected to affect the mechanical properties as the deviation of these angles from 180° in $MAPbI_3$ should reduce its stiffness along <100>; however, such tilting also indicates that the tetragonal structure at room temperature is more closely packed than its tolerance factor reveals.

Since $FAPbBr_3$ and $MAPbBr_3$ both crystalise in the same cubic space group, a direct comparison can be made between them. Interestingly, the Young's moduli of $FAPbBr_3$ are substantially lower than those of $MAPbBr_3$ along all indentation directions (Table 5-2). Replacing the MA cation with the larger FA cation increases the lattice parameter from the XRD data and hence the average Pb-Br length by about 1% [46] and weakens the inorganic framework. The lower Young's modulus of $FAPbBr_3$ is evidence that the Pb-Br bond strength is an important factor determining the elastic response of single Pb-based hybrid perovskites.

Another aspect of the difference between FA- and MA-based perovskites is their hydrogen bonding characteristics. One reasonable indicator of the hydrogen bonding strength in hydrogen bonded systems is the Y···X interatomic distance,[222223] where, in our case, Y = N (or C) and X = Br. However, such distances are difficult to measure using X-ray diffraction in the present system because of the difference in atomic number between Br and N (or C) and the presence of FA cation disorder at room temperature. Recent X-ray studies on $MAPbBr_3$ and $FAPbBr_3$ have simply focused on the Pb-Br bond lengths and other distortions of the inorganic framework using X-ray pair distribution functions (PDFs).[192,224,225] Therefore, to further understand the effects of hydrogen bonding on the stiffness, we performed AIMD simulations (calculations were done by Zeyu Deng) at 300K on both $MAPbBr_3$ and $FAPbBr_3$. The results, presented in terms of radial distribution functions (RDFs), are shown in Figure 5-10, which shows the statistics of interatomic distances averaged throughout the calculations.

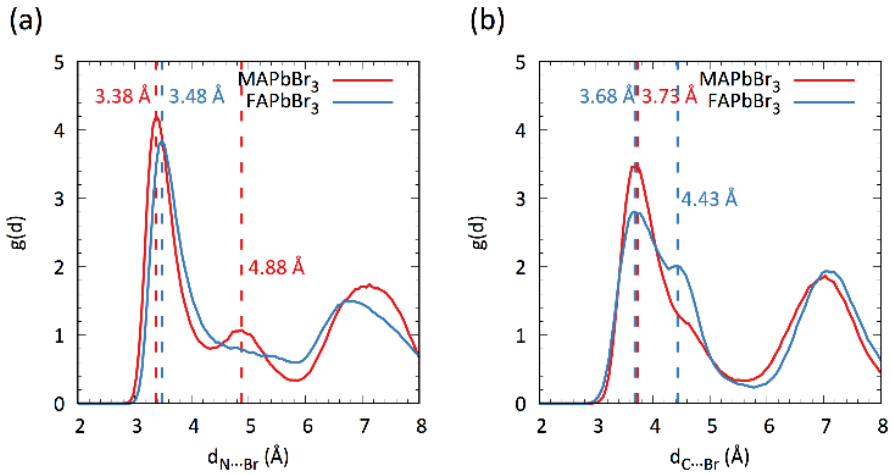

Figure 5-10 Computed radial distribution functions (g(d)) of $MAPbBr_3$ and $FAPbBr_3$ for (a) N···Br and (b) C···Br interatomic distances.

Figure 5-10 shows that the 1st peaks corresponding to the closest N···Br interatomic distances are at around 3.38 Å and 3.48 Å for $MAPbBr_3$ and $FAPbBr_3$, respectively. However, the closest C···Br distances are longer (3.73 Å and 3.68 Å) and slightly larger in $MAPbBr_3$ (~ 0.05 Å) than in $FAPbBr_3$, as shown in Figure 5-10 (b). Hydrogen bonding depends mainly on the electronegativity of the hydrogen bond donor (C and N here) and the electronegativity of N (3.0) is much larger than C (2.5),[221] hence the strength of the hydrogen bonding interaction in N-H···Br is much greater than in C-H···Br. The N···Br distance is a good indicator of the strength of hydrogen bonding and there is a significant difference (~0.1 Å) in N···Br between $MAPbBr_3$ and $FAPbBr_3$, suggesting that hydrogen bonding in the former is stronger. Previous calculations on $MAPbI_3$ have indicated that the MA cation is not located at the centre of the cubic unit cell and molecular translation is very important for stabilizing the structure due to the N-H···I hydrogen bonding interaction.[226] One explanation for the different RDFs could be the different hydrogen bonding characteristics in $MAPbBr_3$ and $FAPbBr_3$ originating from the symmetry of the organic cation, whereby MA can be displaced from the centre of the 12-fold inorganic cage more than FA, since FA has a mirror plane containing the C-H bond direction. In addition, the cationic charge is distributed over its entire structure via the π system for $FAPbBr_3$. The same effect was seen experimentally in the low temperature iodide perovskites, where the N···I distance is longer and the C···I distance is shorter in $FAPbI_3$ compared to $MAPbI_3$.[187] The weaker hydrogen bonding in $FAPbBr_3$ contributes to its low stiffness.

5.4 Mechanical properties of double perovskites

5.4.1 $(MA)_2KBiCl_6$

As the first HOIP double perovskite for photovoltaic applications, $(MA)_2KBiCl_6$ has attracted considerable attention since the structure was published in 2016.[99] In this 3D perovskite network, alternating KCl_6 and $BiCl_6$ octahedra share corners and form a ReO_3-like framework, with the MA cations filling the A-site cavities. The crystal forms in rhombohedral space group $R\bar{3}m$ at room temperature, with lattice parameters a = 7.8372(2) Å and c = 20.9938(7) Å (Figure 5-11). The tolerance factor of $(MA)_2KBiCl_6$ was estimated to be 0.93, which is well within the range of stable 3D perovskite architectures (0.80–1.0). Due to the size difference between K^+ (1.38 Å) and Bi^{3+} (1.03 Å),[220] the KCl_6 octahedra are slightly distorted with K–Cl bond lengths of 3.049(2) Å and two octahedral bond angles of 81.67(9)° and 98.33(9)°, while the $BiCl_6$ octahedra have a more regular shape with Bi-Cl distances of 2.681(2) Å and bond angles of 91.76(10)° and 88.24(10)°. Furthermore, hydrogen bonding is evident in $(MA)_2KBiCl_6$, with N···Cl distance of 3.406(1) Å, shorter than the C···Cl distance (3.848(2) Å). The corresponding distances for N···Cl in orthorhombic $(MA)PbCl_3$ are 3.273(2) Å, 3.346(2) Å, 3.366(10) Å and 3.421(2) Å, suggesting that hydrogen bonding is important for both structures.

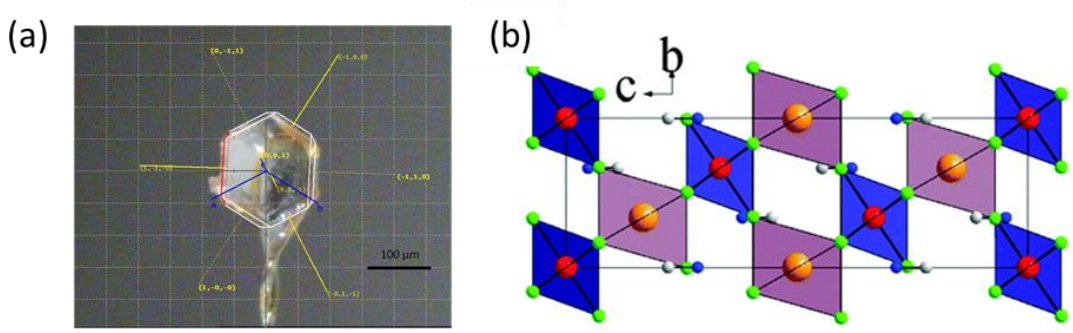

Figure 5-11 (a) Photographs of representative face-indexed single crystal $(MA)_2KBiCl_6$. (b) Crystal structure of $(MA)_2KBiCl_6$, obtained from single crystal X-ray diffraction, viewed along a axis, Red: Bi, brown: K, green: Cl, white: C, blue: N. $BiCl_6$ and KCl_6 octahedra are shown in blue and purple, respectively.[99]

Nanoindentation was carried out normal to the (001) plane of the single crystals. The Young's modulus was found to be 10.50 ± 1.18 GPa and the hardness 0.39 ± 0.07 GPa,

averaging the results from an indentation depth of 200 nm to 900 nm (Figure 5-12). Unfortunately, we were not able to indent on other facets due to the plate-like crystal shapes. In comparison with the experimental mechanical properties of the lead-based perovskites, the Young's modulus of $(MA)_2KBiCl_6$ is comparable with that of (MA)PbI_3 ($E \approx 11$ GPa) and lower than that of (MA)$PbCl_3$ ($E \approx 17$–20 GPa). Since the crystal structures of (MA)$PbCl_3$ and $(MA)_2KBiCl_6$ adopt the same topology and differ only in terms of the B-site cations, the greater compliance of $(MA)_2KBiCl_6$ can be attributed to the weaker K–Cl bonding in comparison with that of Pb–Cl.

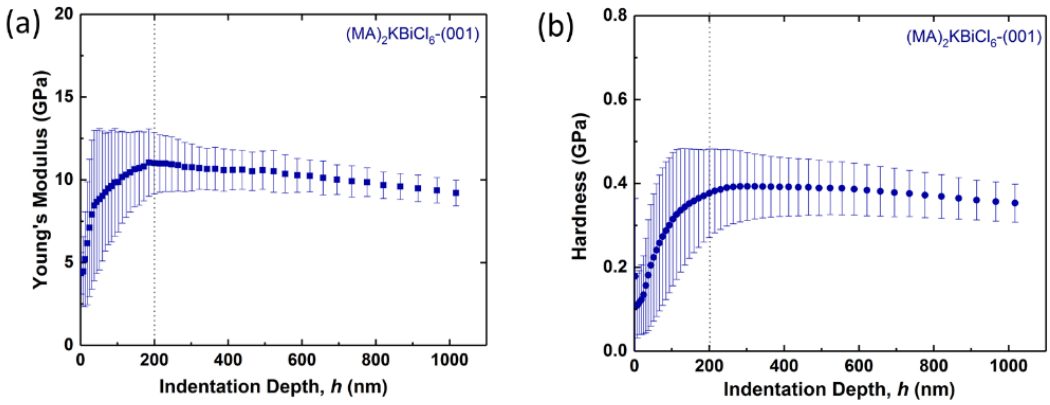

Figure 5-12 (a) Young's modulus and (b) hardness of $(MA)_2KBiCl_6$ as a function of indentation depth.

In addition, we compared our measured Young's modulus with the computational results from DFT calculations (calculations were done by Zeyu Deng), where single crystal stiffness constants (C_{ij}) were calculated from the stress-strain relationship by applying 2 types of strain: e_1 and e_3+e_4 to the cell (each strain with ±0.5% and ±1% deformation) and relaxing the internal degrees of freedom.[39] In order to better understand the mechanical properties of $(MA)_2KBiCl_6$, a 3D directional Young's modulus and its contour plots were calculated by tensorial analysis of the C_{ij}'s and is shown in Figure 5-13. The directions along Bi-Cl-K bonds have the largest value of the Young's modulus, which is similar to (MA)PbX_3 (X = I, Br or Cl).[30] The calculations predict a Young's modulus of 13.07 GPa normal to the (001) facet, which is in reasonable agreement with the experimental nanoindentation results.

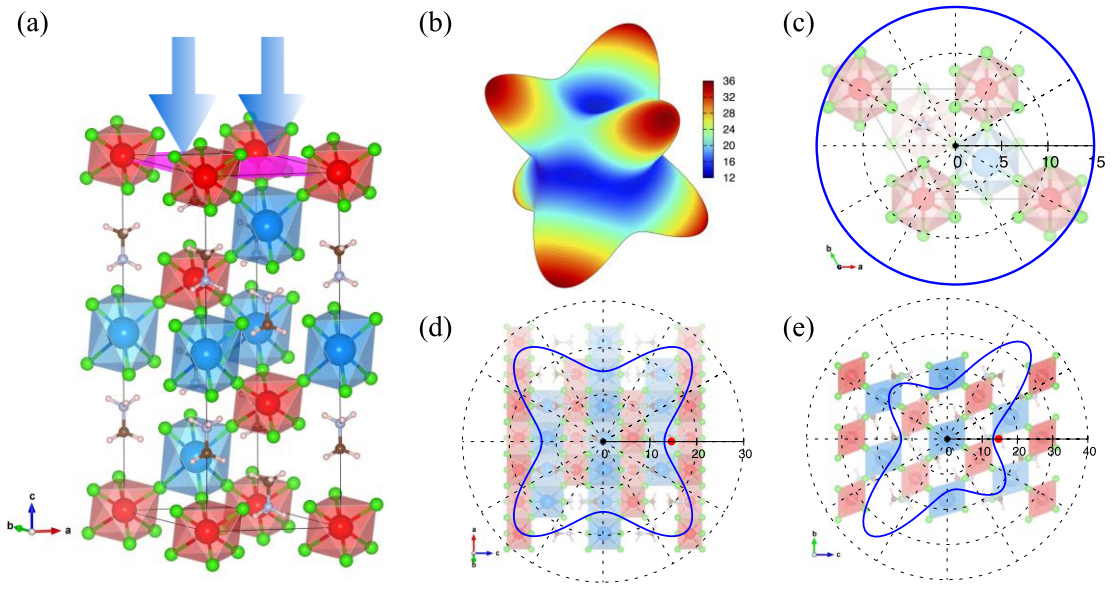

Figure 5-13 (a) Nanoindentation plane (purple) and direction (blue arrow) (b) Calculated 3D directional Young's modulus of $(MA)_2KBiCl_6$ and its contour plot on (c) (001) plane (d) (010) plane and (e) the plane perpendicular to [100]. Nano-indentation Young's modulus is shown as red dot in (d) and (e) along c-axis compared with DFT results (blue curve). Units shown are in GPa.

5.4.2 $(MA)_2TlBiBr_6$

$(MA)_2TlBiBr_6$ is isoelectronic with $MAPbBr_3$ and has a direct bandgap of 2.16 eV, which is much narrower bandgap than $(MA)_2KBiCl_6$.[101] However, despite its interesting electronic properties, the severe toxicity of Tl precludes $(MA)_2TlBiBr_6$ from being a practical alternative to the Pb analogue. $(MA)_2TlBiBr_6$ crystallises in cubic space group $Fm\bar{3}m$ (a = 11.762(2) Å) at room temperature, with Tl^+ and Bi^{3+} occupying alternating octahedral sites. The MA^+ cations are disordered, and the corresponding size of the electron density is ~2.25 Å, similar to the size of MA^+ (2.17 Å). The bond length of Bi–Br is 2.794(4) Å and that of Tl–Br is 3.087(4) Å, which are comparable with the calculated bond lengths of 2.854 Å and 3.145 Å. The Pb–Br bond length is 2.966 Å in the previously reported cubic $MAPbBr_3$ (Table 5-3).

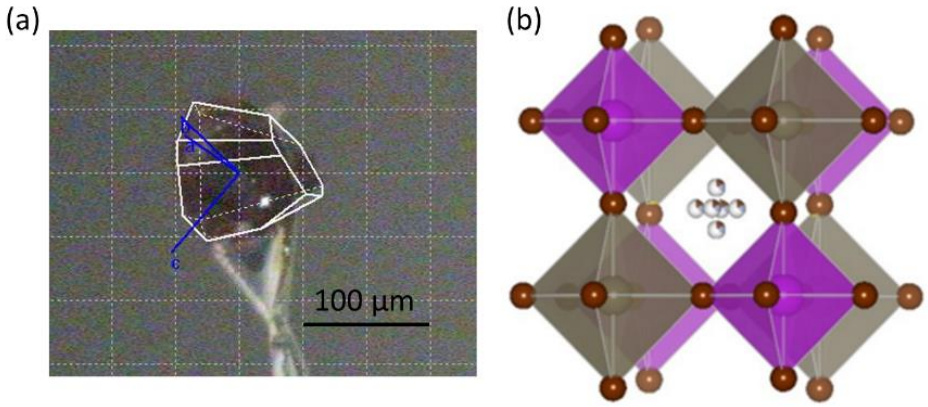

Figure 5-13 (a) Photographs of representative face-indexed single crystal $(MA)_2TlBiBr_6$. (b) Crystal structure of $(MA)_2TlBiBr_6$, obtained from SCXRD. $BiBr_6$ and $TlBr_6$ octahedra are shown in purple and grey, respectively. C and N are modelled with partial occupancies to show the disorder.[99]

Young's modulus of 12.8 ± 1.9 GPa and hardness of 0.56 ± 0.10 GPa were obtained with the indenter tip normal to the (111) facets in a cubic structure (Figure 5-14). DFT calculations of $(MA)_2TlBiBr_6$ in rhombohedral symmetry shows Young's modulus of 11.98 GPa along the equivalent direction normal to (111) in the cubic structure, which is in reasonable agreement to the experimental value.

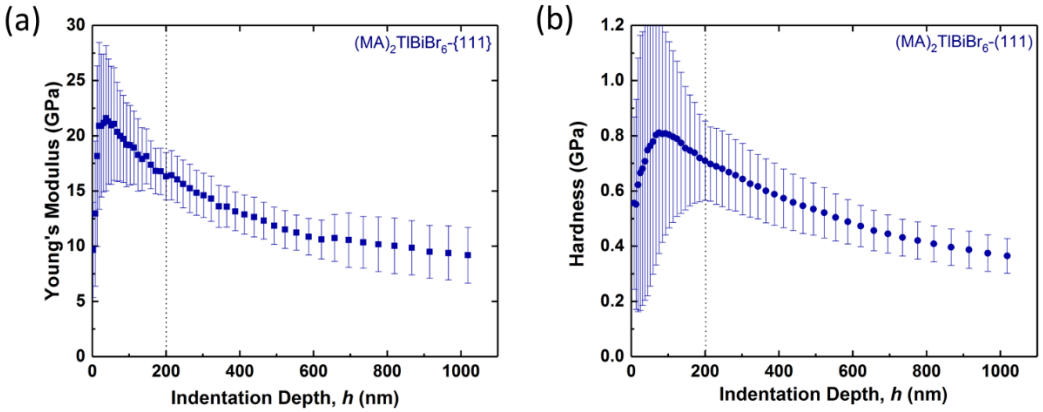

Figure 5-14 (a) Young's modulus and (b) hardness of $(MA)_2TlBiBr_6$ as a function of indentation depth.

5.4.3 $(MA)_2AgBiBr_6$

$(MA)_2AgBiBr_6$ also crystallizes in cubic space group $Fm\bar{3}m$ at room temperature with a lattice parameter a of 11.6370(1) Å. Alternating $AgBr_6$ and $BiBr_6$ octahedra form a 3D framework, resulting in a doubled cell compared to the normal hybrid perovskite. The Ag–Br bond (2.952(2) Å) is slightly longer than the Bi–Br bond (2.868(2) Å). The orientation of the MA cation, which is disordered in $Fm\bar{3}m$ (Figure 5-15).

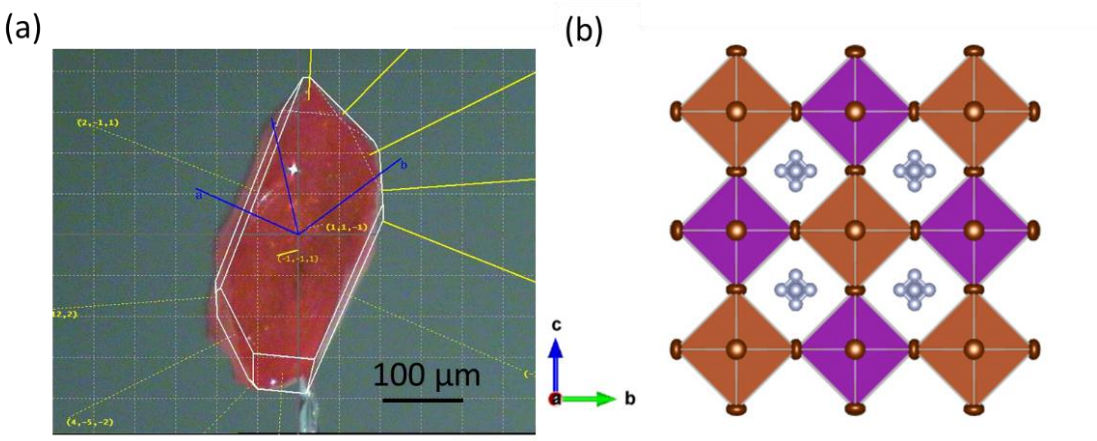

Figure 5-15 (a) Photographs of representative face-indexed single crystal $(MA)_2AgBiBr_6$. (b) Crystal structure of $(MA)_2AgBiBr_6$ viewed along a-axis from SCXRD. $BiBr_6$ and $AgBr_6$ octahedra are shown in purple and orange, respectively. C and N are modelled with partial occupancies to show the disorder.

The mechanical properties of $(MA)_2AgBiBr_6$ were measured by nanoindentation along the normals of the (110) and (111) facets in the cubic space group. The following Young's moduli (E) and hardnesses (H) were found: E_{110} = 8.4 ± 1.7 GPa, and H_{110} = 0.47 ± 0.09 GPa; E_{111} = 7.9 ± 1.4 GPa, and H_{111} = 0.55 ± 0.11 GPa. The anisotropy observed here is attributed to the different orientations of the inorganic Ag–Br–Bi linkages with respect to indentation directions (Figure 5-16). Via comparison of the mechanical properties of $(MA)_2AgBiBr_6$ with those of the analogous Pb-based phase, $MAPbBr_3$, the nanoindentation results on the (110) facets show that $(MA)_2AgBiBr_6$ is far more compliant than $MAPbBr_3$; In addition, via comparison of $(MA)_2AgBiBr_6$ with $(MA)_2TlBiBr_6$, the Ag phase shows a Young's modulus lower than that of the Tl-

containing double perovskite along the same crystallographic orientation, probably because of the greater packing density in the thallium phase.

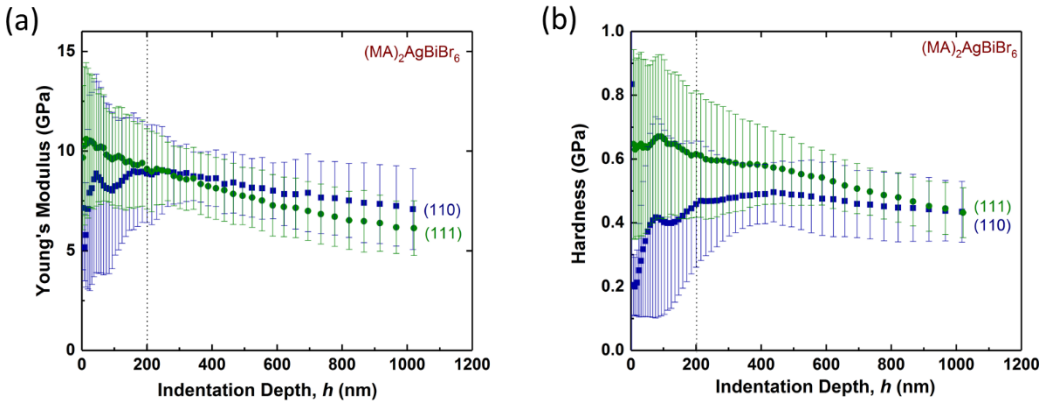

Figure 5-16 (a) Young's modulus and (b) hardness of $(MA)_2TlBiBr_6$ as a function of indentation depth.

5.5 Comparison of single and double perovskites

To further explore the structure-property relationships underlying the observed mechanical behaviour, we compare our results with other systems in the broader halide HOIP family. Figure 5-17 summarizes the reported mechanical properties of single and double hybrid halide perovskites to date. When looking at double perovskites with the general formula A_2MBiX_6 (A = MA, M = a monovalent cation), it is found that replacing the B-site ion, Pb^{2+}, with a monovalent cation and a trivalent cation, in this case Bi, reduces the overall stiffness. This trend likely originates in the weaker bonds between the monovalent ion and the halide, which allow for elastic deformation to occur at relatively low stress. A similar phenomenon has been observed in metal organic frameworks, such as $Zn(Im)_2$(Im = imidazole), where the stiffness is three times higher than its lithium boron analogue, $LiB(Im)_4$.[227] Replacing Zn^{2+} cations with alternating Li^+ and B^{3+} in zeolitic imidazolate frameworks (ZIFs) reduces the elastic modulus from 8–9 GPa for $Zn(Im)_2$ to ~3 GPa for $LiB(Im)_4$. [227]

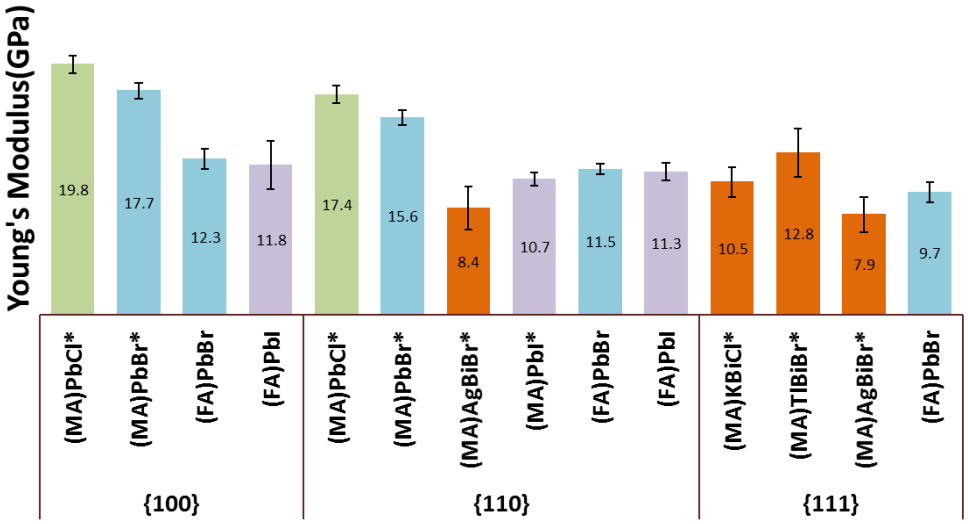

Figure 5-17 Young's moduli of single and double hybrid halide perovskites normal to the {100}, {110} and {111} planes, respectively. Comparisons of elastic properties of $APbX_3$ with A_2MBiX_6 (A = MA or FA, M = K, Tl or Ag and X = I, Br or I) are shown. For the tetragonal ($MAPbI_3$) and rhombohedral (MA_2KBiCl_6) systems, the equivalent cubic planes are used. All values were determined by nanoindentation using the Oliver-Pharr method at room temperature. *Young's moduli were taken from Ref ([211]) for $MAPbX_3$ and Refs ([99–101]) for the double perovskites. Perovskite compositions were labelled with the atom names, instead of the full chemical formulae for presentation purpose. The Cl-, Br- and I-based single perovskites are marked in green, blue and purple respectively. All the double perovskites are marked in orange.

Considering the effect of the halide, the general trend for the single perovskites is that the stiffness decreases as the electronegativity of the halogen decreases, i.e. from Cl to Br to I (green, blue and purple histograms respectively in Figure 5-17). The smaller electronegativity causes a reduction in Pb-X bond strengths. Concerning the anisotropy of the stiffness, <100> directions in the cubic perovskites are the strongest since they lie along the direction of the lead halide bonds Figure 5-18 (a) shows that across the family of lead-based single halide perovskites, longer Pb-X bond distances lead to lower mechanical stiffness. The approximately linear dependence of Young's modulus on bond distance is not observed in double perovskites, as seen in Figure 5-18 (b) and (c). Clearly the presence of both monovalent and trivalent metal cations in the structure disturbs the uniformity of the bonding and the elastic response of the double perovskite cannot be represented by a single bond distance.

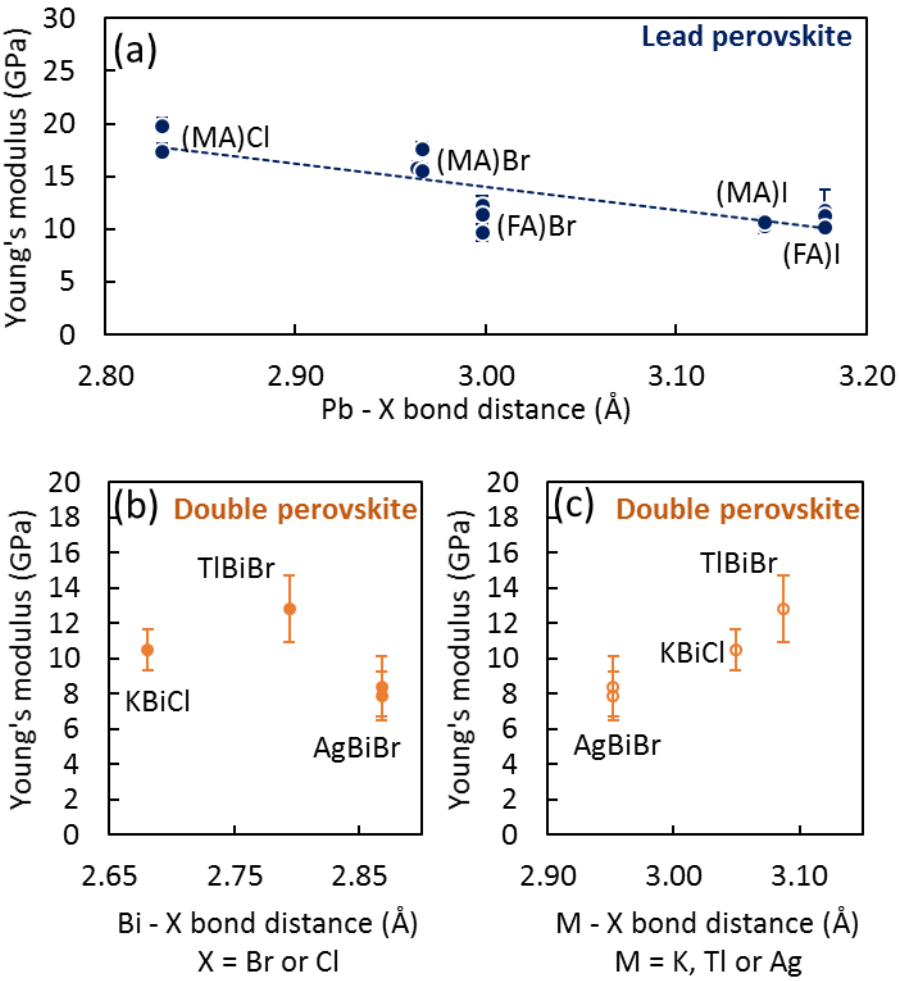

Figure 5-18 Young's moduli of hybrid halide perovskites as a function of metal-halogen bond distance at room temperature for lead-based single MA and FA perovskites shown in (a),[170] and lead-free double MA perovskites in (b) and (c).[99–101] Different data points on the same materials refer to Young's moduli along different crystallographic directions. For $MAPbI_3$, which is tetragonal,, the shortest Pb – I distance was used.[170] Perovskites with different compositions were labelled with the atom names instead of the full chemical formulae. The dotted line is to guide the eye.

Interestingly, from Figure 5-18 (a), the Young's modulus of $FAPbBr_3$ is lower than expected from its bond strength compared to $MAPbBr_3$. The tolerance factor of $FAPbBr_3$ is high (1.01), indicating that the structure is on the edge of the stability range for a three-dimensional perovskite. Recently, $FAPbBr_3$ and $MAPbBr_3$ were reported to undergo a phase transition to a body-centred cubic structure (space group $Im\bar{3}$) at 0.53 GPa and 0.9 GPa, respectively, using high pressure X-ray diffraction.[170] The lower phase transition

pressure for $FAPbBr_3$ further indicates that it is less mechanically stable than its MA counterpart under external load. One factor is likely to be the weakness of the hydrogen bonding in $FAPbBr_3$, as discussed above. Another factor is that for perovskites with high tolerance factors, the accommodation of large cations increases the possibility of local octahedral tilting, which reduces their mechanical stability while attempting to maintain the overall cubic structure. We should note that a hard sphere model was used in the tolerance factor approach, assuming the cations are fully disordered at room temperature. The effect of the asymmetric cation shape on the lattice distortions, however, is not captured in the tolerance factor calculations. Considering ionic size effects in double perovskites, we calculated using DFT the mechanical properties of a range of existing and hypothetical hybrid double perovskites in $R\bar{3}m$ space group symmetry (calculations were done by Zeyu Deng).[15] The results revealed that although most double perovskites are most stiff along the inorganic bond direction, for compositions with high tolerance factors, directions parallel to the C-N bonds of the MA cation become the stiffest, highlighting the role of cationic steric effects and hydrogen bonding.

5.6 Conclusions and future work

In summary, systematic studies of mechanical properties of halide HOIPs have been addressed in this chapter, including the prototypical MA and FA based lead halide perovskites, as well as the non-toxic Bi-based halide double perovskites. Considering the effect of the halide on mechanical response, the Young's moduli of $MAPbX_3$ decreases along the series $E_{Cl} > E_{Br} > E_{I,}$ as a result of combined influences from the Pb - X bond strengths, relative packing density and hydrogen bonding interactions. On the other hand, replacing the B-site metal, Pb, with one trivalent and one monovalent cation leads to a drop in the stiffness. This is likely due to the weaker bond between the monovalent cation and the halide in the perovskite structure.

Despite the hypothesis that larger A-site cations will lead to tighter packing and stiffer perovskites, we find that in $FAPbBr_3$ is more compliant than expected. There appears to be two main factors contributing to the observed mechanical behavior. Firstly, the effect of hydrogen bonding is evident, since more pronounced pop-in events were observed in bromide than the iodide perovskites. Our computational study indicates that $FAPbBr_3$

exhibits weaker hydrogen bond than $MAPbBr_3$, as the former shows longer N···Br distances at room temperature. Secondly, the longer Pb-Br bond length in $FAPbBr_3$ leads to a smaller Young's modulus compared to values for $MAPbBr_3$. Comparing previous studies on the mechanical properties of HOIPs with our current work, we find that although the bond strength of the inorganic framework is a main factor determining stiffness, the size of the organic cations become more important when the perovskites are at their limits of structural stability. This steric effect can be qualitatively captured by the tolerance factor. In addition, as the organic cations become ordered at lower temperatures, the importance of hydrogen bonding on mechanical stability is expected to increase. This effect will be interesting to explore in the future.

In the context of solar cell research, a knowledge of mechanical properties is of crucial importance and has significant influence on manufacturing processes, the design of the cells, and their specific applications. For example, the low hardness of HOIPs is interesting for flexible devices, for instance as soft absorption layer in thin film solar cells. A direction for further research is therefore to compare the mechanical stabilities of HOIPs in the form the bulk single crystals and the polycrystalline thin films. The study of the intrinsic mechanical properties of the HOIPs gives a unique insight into underlying structure-property relations and contributes to the future design of devices with tailored properties.

Chapter 6 Beyond the three-dimensional perovskites

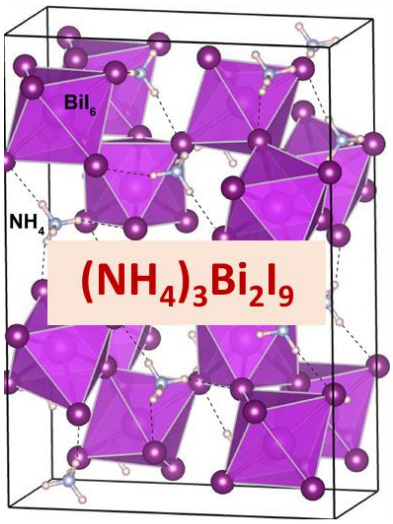

The research in this chapter explores the structural diversity of HOIPs, aiming to searching for more stable and environmentally friendly alternatives to the current 3D perovskites, guanidinium (GUA)-based low dimensional lead perovskites were firstly discussed in the context of using the tolerance factor as a guideline for materials design. The research then focuses on using Bi to replace Pb in hybrid halide perovskites. The synthesis, structure and physical properties of a 2D layered perovskite, $(NH4)_3Bi_2I_9$ and its related Bi- based perovskite-like systems are herein presented.

Some of the results in this chapter have been published in:

- **S. Sun**, S. Tominaka, J. H. Lee, F. Xie, P. D. Bristowe, and A. K. Cheetham. "Synthesis, Crystal Structure and Properties of a Perovskite-Related Bismuth Phase, $(NH_4)_3Bi_2I_9$." *APL Materials*, 2016, **4**, 031101
- G. Kieslich, **S. Sun** and A. K. Cheetham "Solid-state principles applied to organic–inorganic perovskites: new tricks for an old dog", *Chem. Sci.*, 2014, **5**, 4712–4715.

6.1 Overview

In spite of the excellent performances of the 3D hybrid lead perovskites in photovoltaic applications, their instability such as thermal degradation and moisture sensibility limits the use of these materials in devices.[228] Low dimensional perovskite-like structures have hence attracted increasing attention recently due to their chemical stabilities.[108,229] In addition, the wide range of perovskite-like architectures allows compositional engineering, providing the options of removing the toxic lead in the perovskite structures.[106] Hence, this chapter is divided into two parts: the choices of A-site cations in lead based perovskites are briefly discussed first, and we then focus on lead-free systems, in particular, we synthesised perovskite-related structures replacing the B-site metal, lead, with the non-toxic bismuth. A range of materials characterization were conducted to examine the Bi-based perovskite-related systems for photovoltaic applications.

6.2 A-site substitution in lead iodide perovskites

6.2.1 Tolerance factor for HOIPs

The ABX_3 perovskite architecture allows for many potential atom substitutions in order to achieve tailored physical properties.[230] As discussed in Chapter 1, one of the geometric criteria to form a stable 3D perovskite is that the tolerance factor, *t*, lies between 0.8 and 1. Expanding the concept of Goldschmidt's tolerance factor to the big family of HOIPs, however, the major challenges lies in estimating the size of the organic cations. The nature of the organic cations, such as the varying bond lengths due to hydrogen-bonding interactions, makes it difficult to define its ionic radius. Even highly symmetric cations (e.g. $[NH_4]^+$ or $[(CH_3)_4N]^+$), exhibit radii which strongly depend upon their anionic counterparts.[19] In order to choose suitable cations for materials design, we estimated a consistent set of effective radii, r_{eff}, of organic ions (Table 6-1), applying the following model developed by Dr. Gregor Kieslich from the author's research group:

$$r_{eff} = r_{mass} + r_{ion}$$

Where r_{mass} is the distance between the mass centre of the molecule and the atom with the largest ionic radius, and r_{ion} is the corresponding ionic radius. Here we should note that the tolerance factor, *t*, is not the only predominant factor considering the formation

of a 3D perovskite, since non-geometric factors, such as the bond valence and chemical stability, are also important determine the formability or stability of a perovskite structure.[231]

Table 6-1 Calculated effective radii of molecular cations.

Cation		Effective radius (pm)
1	Ammonium $[NH_4]^+$	148
2	Hydroxlammonium $[H_3NOH]^+$	208
3	Methylammonium $[CH_3NH_3]^+$	215
4	Hydrazinium $[H_3N\text{-}NH_2]^+$	218
5	Formamidinium $[HC(NH_2)_2]^+$	241
6	Azetidinium $[(CH_2)_3NH_2]^+$	251
7	Dimethylammonium $[(CH_3)_2NH_2]^+$	271
8	Ethylammonium $[(C_2H_5)NH_3]^+$	273
9	Guandiunium $[C(NH_2)_3]^+$	276
10	Tetramethylammonium $[(CH_3)_4N]^+$	290

6.2.2 Crystal structures of guanidinium lead iodide

Most current research focus on lead iodide perovskites, as they are presently the holders of record conversion efficiencies in photovoltaics.[58] Considering the size of A-site cavity in a $APbI_3$ crystal, medium-sized cations such as caesium (Cs), MA and FA crystallise in 3D perovskite forms. Smaller cations, such as ammonium (NH_4), give $t < 0.8$, and larger ones, e.g. ethylammonium (C_2NH_7), have $t > 1.0$; this leads to the formation of lower dimensional architectures.[232,233] Using the tolerance factor rule as a guidance, hydrazinium and hydroxylammonium have the desirable cation sizes ($0.8 < t < 1$), however, we were not able to incorporate them into the structure due to their chemical instability.

As an alternative to polar organic cations, the non-polar cation, guanidinium (GUA) forms an interesting range of halides. For example, in a recent study, Kanatzidis *et al.*

reported the structure of guanidinium germanium iodide, $GUAGeI_3$.[84] With a tolerance factor as large as 1.202, $GUAGeI_3$ adopts the 1D hexagonal perovskite structure. In addition, despite of the high tolerance factor (t >1), hybrid guanidinium tin halides and related compounds (A= GUA, B=Sn or Ge and X = Br or Cl) have been reported as 3D perovskite.[234] In this case, a stereochemically active lone pair leads to heavily distorted structures and hence the concept of tolerance factor does not exactly fit the experiment. Considering the GUA-based iodoplumates, despite the computational study on the hypothetical 3D perovskite structure of $GUAPbI_3$ reported in 2015,[235] the 3D perovskite form of $GUAPbI_3$ exhibits a tolerance factor of 1.035 and experimentally the low dimensional structures of $GUAPbI_3$ and $(GUA)_2PbI_4$ have been previously reported in the powder form.[236–238] More recently, due to its potential relevance to perovskite-based photovoltaic devices, there have been a few reports on incorporating GUA in the mixed cation perovskites as a route to enhanced carrier lifetime and improved stability,[239,240] and hence a thorough study on the structural characteristics of GUA-based iodoplumates was necessary.

As shown in Figure 6-1, we synthesised the single crystals of three GUA-based iodoplumates, $(GUA)PbI_3$, $(GUA)_2PbI_4$ and $(GUA)_3PbI_5$. The crystals were grown under the same experimental conditions as the reported FA- and MA-based perovskites[56] and the different stoichiometry were obtained by tuning the ratio of GUA and Pb^{2+} in the starting materials. The crystal structures were solved using SCXRD at room temperature and the crystallographic data is listed in Table 6-2.

Figure 6-1 Representative single crystal of (a) $GUAPbI_3$, (b) $(GUA)_2PbI_4$ and (c) $(GUA)_3PbI_5$.

Table 6-2 Crystallographic data and refinement of $GUAPbI_3$, $(GUA)_2PbI_4$ and $(GUA)_3PbI_5$.

Empirical formula*	$C_3I_5N_9Pb$	$C_2I_4N_6Pb$	CI_3N_3Pb
Formula weight	1021.95	834.97	641.93
Temperature/K	297.5(5)	293(2)	299.7(6)
Crystal system	monoclinic	monoclinic	orthorhombic
Space group	C2/c	$P2_1/n$	Pnma
a/Å	13.0694(5)	9.2440(3)	11.9866(5)
b/Å	13.1946(5)	26.9511(11)	4.4740(2)
c/Å	12.7212(5)	12.7155(3)	20.8652(10)
α/°	90	90	90
β/°	91.276(4)	91.482(2)	90
γ/°	90	90	90
Volume/Å^3	2193.18(15)	3166.82(17)	1118.96(9)
Z	4	8	4
ρ_{calc}g/cm^3	3.095	3.503	3.81
μ/mm^{-1}	14.732	18.433	23.293
F(000)	1784	2880	1072
Crystal size/mm^3	0.17 × 0.09 × 0.06	0.35 × 0.11 × 0.06	0.72 × 0.08× 0.07
2Θ range /°	4.388 to 56.64	3.542 to 56.848	3.904 to 46.496
Index ranges	$-17 \le h \le 11$, $-11 \le k \le 17$, $-16 \le l \le 14$	$-9 \le h \le 12$, $-35 \le k \le 15$, $-17 \le l \le 13$	$-13 \le h \le 11$, $-4 \le k \le 4$, $-22 \le l \le 23$
Reflections collected	4425	12954	5700
Independent reflections	2433 [R_{int} = 0.0284, R_{sigma} = 0.0413]	6990 [R_{int} = 0.0212, R_{sigma} = 0.0342]	918 [R_{int} = 0.0403, R_{sigma} = 0.0256]
Data/restraints/parameters	2433/0/103	6990/1/235	918/0/40
Goodness-of-fit on F^2	1.056	1.186	1.018
Final R indexes [I>=2σ (I)]	R_1 = 0.0367, wR_2 = 0.0784	R_1 = 0.0301, wR_2 = 0.0667	R_1 = 0.0216, wR_2 = 0.0482
Final R indexes [all data]	R_1 = 0.0547, wR_2 = 0.0868	R_1 = 0.0365, wR_2 = 0.0687	R_1 = 0.0258, wR_2 = 0.0500
Largest diff. peak/hole / e Å^{-3}	1.16/-1.06	2.27/-1.88	0.80/-0.81

*H positions were not considered in the structural solution due to the difficulty of detecting light H in the presence of heavy Pb and I in X-ray diffraction.

The yellow, needle-like $GUAPbI_3$ crystallises in an orthorhombic space group, *Pnma* with lattice parameters a = 11.9987(8) Å, b = 4.4693(4) Å and c = 20.874(2) Å at room temperature. The lattice parameters from our SCXRD study are consistent to the recent PXRD study by Jodlowski *et al*.[238] The crystal adopts a one-dimensional chain structure, within which each Pb^{2+} ion is coordinated by six I-ions in a distorted octahedral environment. The PbI_6 octahedra are connected by common edges and arranged into double chains along the *b*-axis and the guanidinium ions fit in the spaces between the double chains, as shown in Figure 6-2. This chain-like structure of $GUAPbI_3$ belongs to the NH_4CdCl_3 type and it is isostructural with NH_4PbI_3[232], the room temperature phases (δ phase) of $CsPbI_3$ and $RbPbI_3$[65] grown by the Bridgman technique.[95]

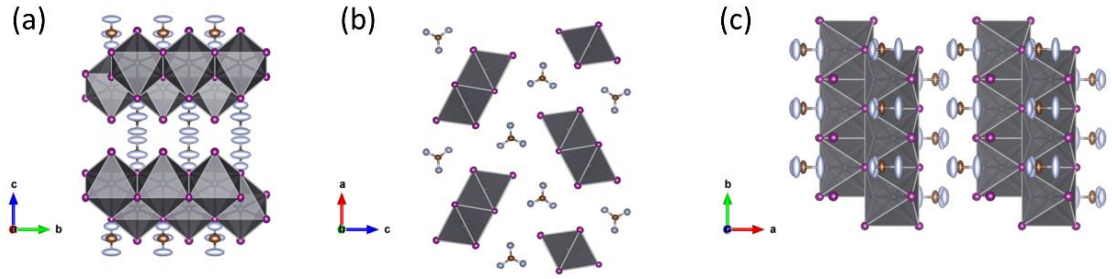

Figure 6-2 Illustration of the crystal structure of $(GUA)PbI_3$ along (a) *a*-axis, (b) *b*-axis and (c) *c*-axis, respectively. Key: the grey polyhedra represent the 1D edge sharing PbI_6 octahedra, purple spheres represent iodide, blue nitrogen and brown carbon. The large ellipsoids of nitrogen show the disorder of GUA cation at room temperature. Hydrogen atoms are not represented.

The yellow/orange rectangular shaped $(GUA)_2PbI_4$ crystals crystallise in the space group $P2_1/n$ with lattice parameter of a = 9.2440(3) Å, b = 26.9511(11) Å, c = 12.7155(3) Å and β = 91.482(2)°. Our SCXRD data is consistent with the reported lattice parmeteters.[236] As shown in Figure 6-3, the structure consists of 2D double layers of corner-sharing octahedra. GUA cations fill the cavities between two polyhedra within a layer and between the layers. The two adjacent polyhedra in the same layer along the *a*-axis are heavily tilted in order to accommodate a GUA ion, with the most distorted Pb-I-Pb angle as low as 154.405(19)°. This is an indication that the GUA cation is too large to fit in the perovskite cage, and this is consistent with the theoretical prediction using our tolerance factor approach. The concept of extending the Goldschmidt tolerance factor to HOIPs and the calculation method to estimate the size of organic cations are reliable here and the

lone pair effects to produce a distorted 3D perovskite are not as dominant as the size factor in this case, unlike in Sn and Ge based guanidinium perovskites in the previous discussion.

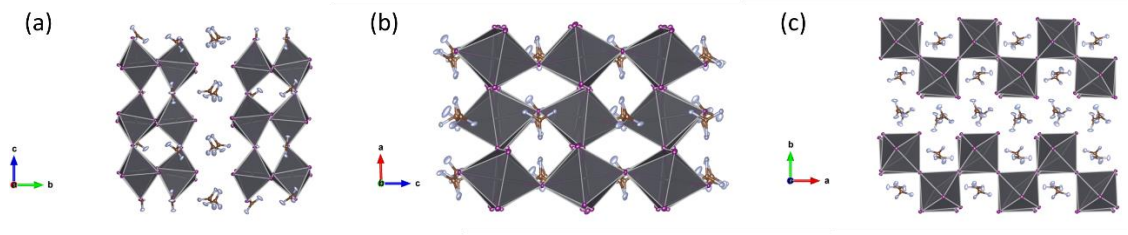

Figure 6-3 Illustration of the crystal structure of $(GUA)_2PbI_4$ along (a) *a*-axis, (b) *b*-axis and (c) *c*-axis, respectively. Key: the grey polyhedra represent the 2D corner sharing PbI_6 octahedra, purple spheres represent iodide, blue nitrogen and brown carbon. The large ellipsoids of nitrogen represent the disorder of GUA cation at room temperature. Hydrogen atoms are not represented.

The yellow crystals of $(GUA)_3PbI_5$ are in monoclinic space group $C2/c$ with lattice parameters of a = 13.0694(5) Å, b = 13.1946(5) Å, c = 12.7212(5) Å and β = 91.276(4)° at room temperature. This composition and crystal structure were not previously reported. In this structure, the PbI_5^{3-} network of corner sharing octahedra forms 1D chains extending along the *c*-axis. The octahedra are relatively less distorted, with Pb-I bond lengths ranging from 3.2123(6) to 3.2505(2) Å and the bridging Pb-I-Pb angle of two adjacent octahedra is 156.13(3)°. Our synthesised $(GUA)_3PbI_5$ crystals have the same inorganic connectivity to the reported FA_3PbI_5 in the space group $P2_1/c$,[241,242] the latter also exhibited 1D chain character with corner sharing octahedra.

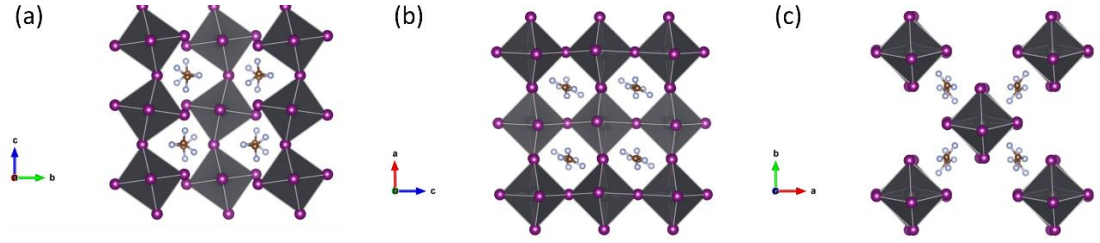

Figure 6-4 Illustration of the crystal structure of $(GUA)_3PbI_5$ along (a) *a*-axis, (b) *b*-axis and (c) *c*-axis, respectively. Key: the grey polyhedra represent the 1D corner sharing PbI_6 octahedra,

purple spheres represent iodide, blue nitrogen and brown carbon. The large ellipsoids of nitrogen represent the disorder of GUA cation at room temperature. Hydrogen atoms are not represented.

The choice of A cation affects the dimensionality of the structure. Under the same synthetic conditions, with a size increase from 241pm (FA) to 276 pm (GUA), 3D lead iodide perovskites were not obtained. The example of A-site substitution using GUA demonstrates the structural diversity of the HOIP family. However, as shown in Figure 6-1, the yellow colours of the GUA-based low dimensional perovskites indicate relatively large bandgaps (2.3 eV for $GUAPbI_3$[238]) and hence their potential in photovoltaic applications are limited. The investigation of the eluminescence properties of these low dimensional materials is interesting for future studies.

6.3 B-site substitution and lead-free systems

6.3.1 Recent reports on Bi-based perovskite-related systems

In order to remove the toxicity in perovskite devices, Snaith *et al.* and Kanatzidis *et al.* recently reported the replacement of Pb by other Group IV metals, specifically Sn[83,243] and Ge.[84] However, the preferred oxidation states of Sn^{4+} and Ge^{4+} reduce the stability of these perovskite structures in air. Beyond the Group IV metals, our attention is drawn to the possibility of using bismuth as an alternative to lead in perovskite architectures. Bismuth is used in medicine, where it is available in tablet form to treat upset stomachs, heartburn, nausea and diarrhea.[244] However, the conventional hybrid perovskites have the formula ABX_3 (where A is a monovalent amine cation, B is a divalent metal and X is a halide ion) and hence it is challenging to accommodate Bi^{3+} instead of Pb^{2+} at the B site. When replacing PbI_2 by BiI_3 with the same synthesis condition as $MAPbI_3$, we obtained methylammonium bismuth iodide, $MA_3Bi_2I_9$, which is a 0D dimer at room temperature (see Appendix Figure-A 5) and the structure is isostructural with $(CN_3H_6)_3Sb_2I_9$, $(CN_3H_6)_3Bi_2I_9$,[245] as well as $Cs_3Bi_2I_9$.[246] This structure type is also known in Sb-based compounds, such as $(NH_4)_3Sb_2I_9$[247] and $Rb_3/Cs_3Sb_2I_9$,[248] and Mitzi *et al.* characterized $Cs_3Sb_2I_9$ thin-films[249] and reported their potential for photovoltaic applications. In addition, $MA_3Bi_2I_9$ has recently been made into solar cell devices and achieved efficiency

of over 1%,[85] and alkaline metal based bismuth iodides, $A_3Bi_2I_9$ (A = K, Rb and Cs) were studied in the context of photovoltaic applications for the first time in 2016. [250]

6.3.2 $(NH_4)_3Bi_2I_9$

The applications of the recent wide band-gap layered perovskite materials encouraged us to explore layered perovskites with the ABX_4 structure where, in this case, A is a monovalent cation, B is a trivalent metal, e.g. Bi and X is a monovalent halide.[251] In attempts to synthesise a layered structure isostructural to NH_4FeF_4,[252] a 2D perovskite-related phase, $(NH_4)_3Bi_2I_9$ was obtained, which is isostructural to hexagonal $Rb_3Bi_2I_9$.[250,253] This perovskite-like structure was characterized and its potential as a photovoltaic material was examined by band structure analysis and conductivity measurements.

6.3.2.1 Crystal structure

A dark red bismuth phase, $(NH_4)_3Bi_2I_9$, with a 2D layered perovskite-like architecture was synthesised in solution under the similar experimental conditions as $MAPbI_3$ (see Chapter 2 for experimental details). $(NH_4)_3Bi_2I_9$ crystallises in the monoclinic space group $P2_1/n$ with lattice parameters a = 14.6095(4) Å, b = 8.1427(3) Å, c = 20.9094(5) Å and β = 90.917(2)°. A summary of the crystal structure information is shown in Table 6-3. (CCDC deposition number 1434984).

The framework of $(NH_4)_3Bi_2I_9$ consists of bismuth iodide layers stacked in a closed-packed fashion, forming hexagonal layers in the *ab* plane, as shown in Figure 6-5 (a) and (c). Each Bi^{3+} atom is coordinated by six I^- ions in a distorted octahedral environment, as shown in Figure 6-5 (d), with Bi –I bond distances ranging from 2.93 Å to 3.27 Å. The BiI_6 octahedra are corner sharing and there are Bi atoms filling two-thirds of the available BiI_6 octahedra cavities. As seen in Figure 6-5 (b), the structure of $(NH_4)_3Bi_2I_9$ is hence related to the conventional 3D perovskites, as it is the structure obtained after removing every third octahedral layer along the <111> direction of a cubic ABX_3 perovskite.

Table 6-3 Crystallographic data and refinement of $(NH_4)_3Bi_2I_9$.

Empirical formula	$Bi_2I_9N_3$*
Formula weight	1602.09
Temperature/K	300.00(14)
Crystal system	monoclinic
Space group	$P2_1/n$
a/Å	14.6095(4)
b/Å	8.1427(3)
c/Å	20.9094(5)
α/°	90
β/°	90.917(2)
γ/°	90
Volume/Å^3	2487.06(12)
Z	4
ρ_{calc}g/cm^3	4.279
μ/mm^{-1}	25.288
F(000)	2656
Crystal size/mm^3	0.2023 × 0.1729 × 0.1098
Radiation	MoKα (λ = 0.71073)
2Θ range for data collection/°	3.376 to 54.202
Index ranges	$-18 \leq h \leq 9$, $-10 \leq k \leq 8$, $-26 \leq l \leq 24$
Reflections collected	10639
Independent reflections	5325 [R_{int} = 0.0253, R_{sigma} = 0.0441]
Data/restraints/parameters	5325/0/129
Goodness-of-fit on F^2	1.001
Final R indexes [I>=2σ (I)]	R_1 = 0.0362, wR_2 = 0.0710
Final R indexes [all data]	R_1 = 0.0653, wR_2 = 0.0823
Largest diff. peak/hole / e Å^{-3}	1.13/-0.93

*H positions were not considered in the structural solution due to the difficulty of detecting light H in the presence of heavy Bi and I in X-ray diffraction.

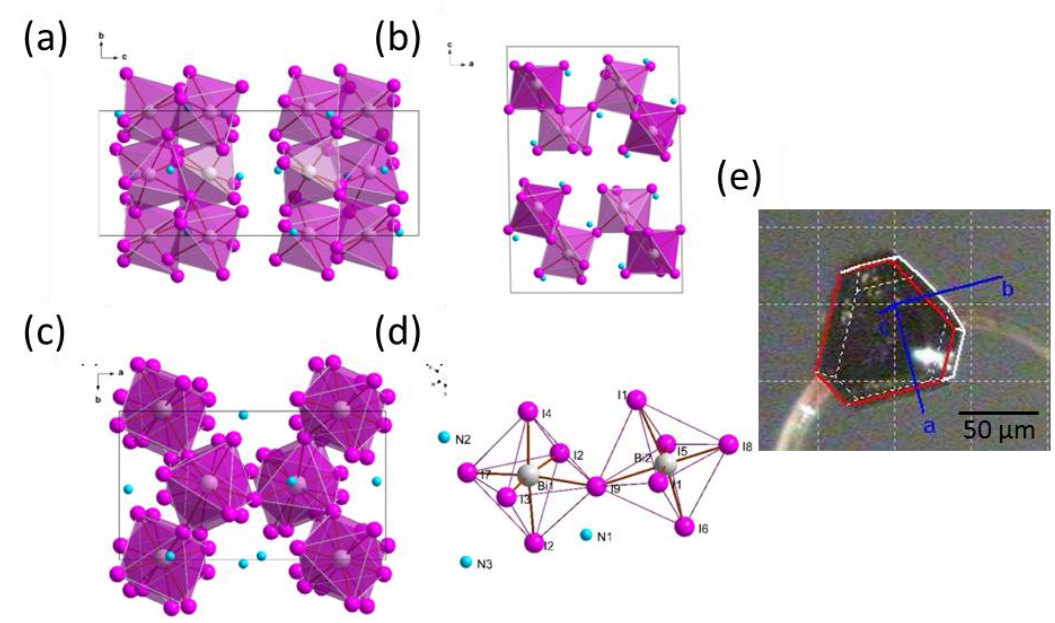

Figure 6-5 Crystal structure of the $(NH4)_3Bi_2I_9$ phase along (a) *a*-axis, (b) *b*-axis and (c) *c*-axis. Black lines mark the unit cell edges. (d) Two corner sharing BiI_6 octahedra. The silver, purple and blue spheres represent bismuth ions, iodine ions and nitrogen atoms in NH_4 ions respectively. (e) photograph of a representative single crystal of $(NH4)_3Bi_2I_9$.

6.3.2.2 Phase stability

CHN analysis was performed to confirm the elemental composition; observed: H: 0.80wt%, N: 2.5wt%; calc: H: 0.75wt%, N: 2.6wt%. The bulk phase purity was confirmed by PXRD (Figure 6-6).

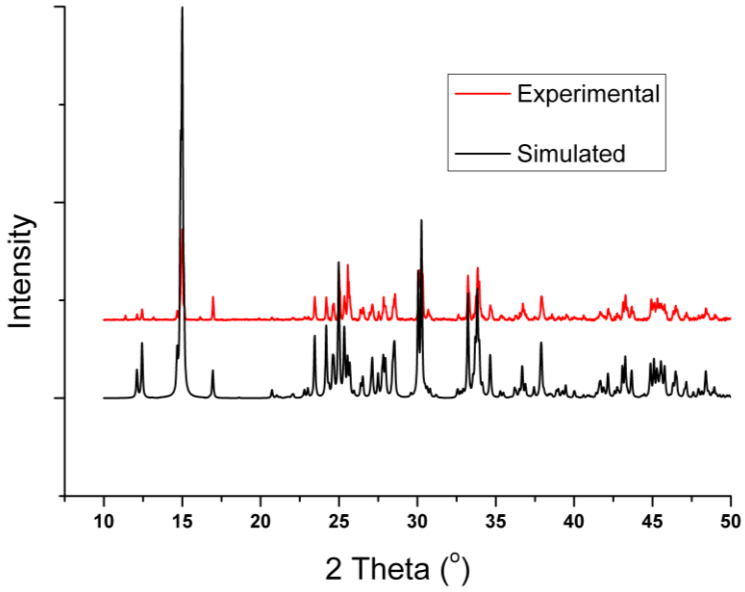

Figure 6-6 PXRD pattern of experimental and simulated $(NH_4)_3Bi_2I_9$ phase.

Unlike $Cs_3Sb_2I_9$, which forms both 0D dimer and 2D layered polymorphs,[249] our VT SCXRD studies on $(NH_4)_3Bi_2I_9$ reveal no evidence of a phase transition and the layered structure was stable across the temperature range 120 K to 380 K (Figure 6-7).

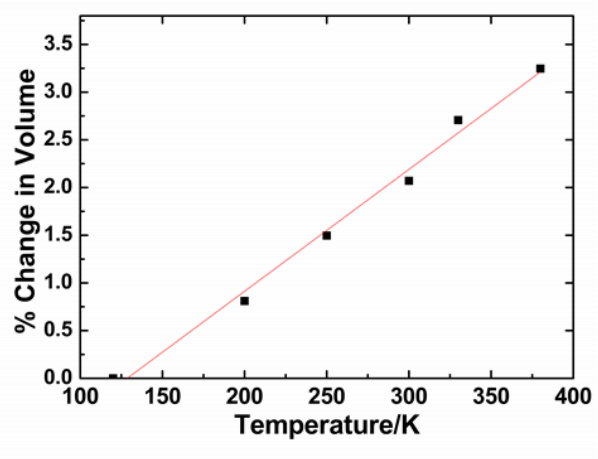

Figure 6-7 Change in unit cell volume as a function of temperature from 120 K to 380 K.

The change of lattice parameters as a function of temperature is shown in Figure 6-8 and coefficients of thermal expansion of $(NH_4)_3Bi_2I_9$ (along *a*, *b*, *c* axis and volumetric) over 120 K - 380 K (10^{-5}/K) were calculated: $\alpha_a = 4.6$, $\alpha_b = 5.6$, $\alpha_c = 2.1$, $\alpha_v = 12.5$. The small thermal expansion along the *c* direction is because that the inorganic layers are perpendicular to *c*-axis.

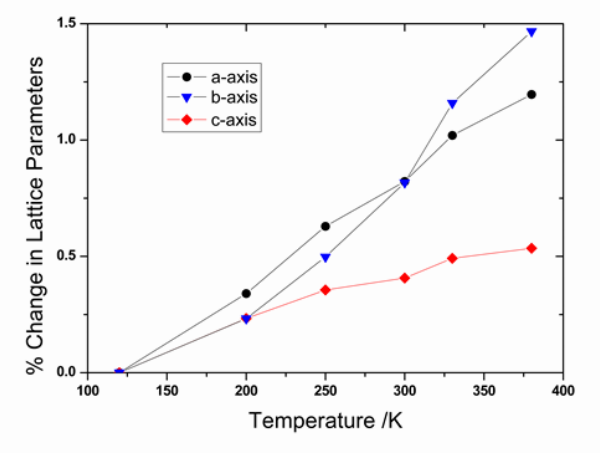

Figure 6-8 Change in lattice parameters as a function of temperature from 120 K to 380 K.

To examine the thermal stability of $(NH_4)_3Bi_2I_9$, TGA analysis was performed with 6.31 mg of the sample on a platinum pan. The sample was heated at a rate of 10 °C min^{-1} up to 800 °C, with significant weight loss being observed from around 240 °C.

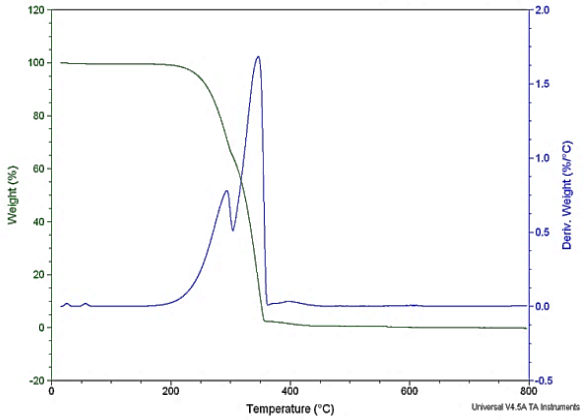

Figure 6-9 TGA curve of $(NH4)_3Bi_2I_9$ under a continuous nitrogen flow.

6.3.2.3 Band gap determination

The optical characterization of $(NH_4)_3Bi_2I_9$ was performed on a PerkinElmer Lambda 750 UV-visible spectrometer and the measurements were repeated with several sample rotations of 45° by Fei Xie. The band gap of the powder sample was measured to be 2.04 eV, (Figure 6-10), and this is lower than the band gap of the 0D dimer bismuth phase $MA_3Bi_2I_9$,[11] which is 2.11 eV (see Appendix Figure-A 5). The band gap of layered $(NH_4)_3Bi_2I_9$ is also lower than the 3D perovskite, $MAPbBr_3$, which was reported with a band gap around 2.20 eV.[57]

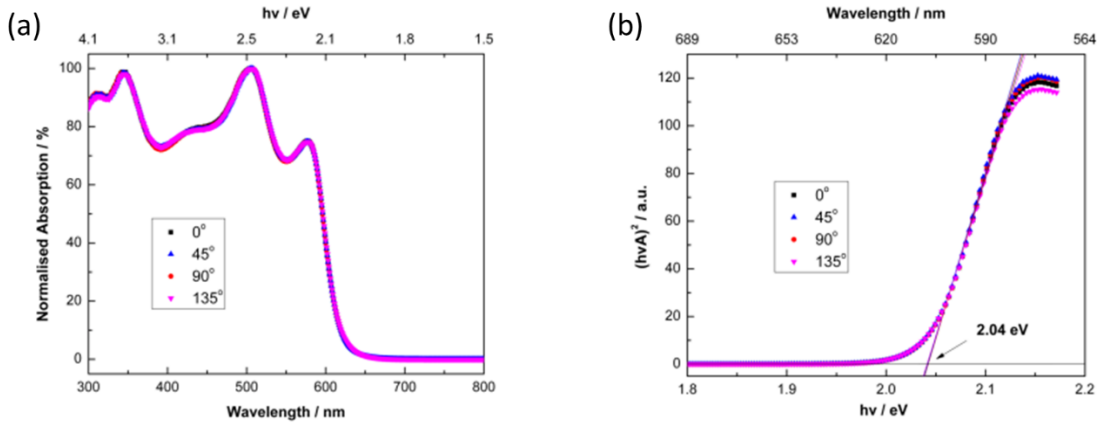

Figure 6-10 (a) Normalized absorption spectrum and (b) Tauc plot with band gap calculated, showing a direct band gap. The measurements were repeated with sample rotations to confirm consistency.

6.3.2.4 DFT calculations

The calculated lattice parameters obtained at 0 K were a = 14.6094 Å, b = 8.1617 Å, c = 20.8595 Å, and β = 90.61°, in good agreement with our experimental values. The DFT calculations were performed by Dr. Jung-Hoon Lee in the author's department. In this structure, the hydrogen-bond interactions play a key role in stabilising the layered architecture. Namely, hydrogen-bonds provide links between the BiI_6 octahedra and thereby stabilize the whole structure (Figure 6-11).

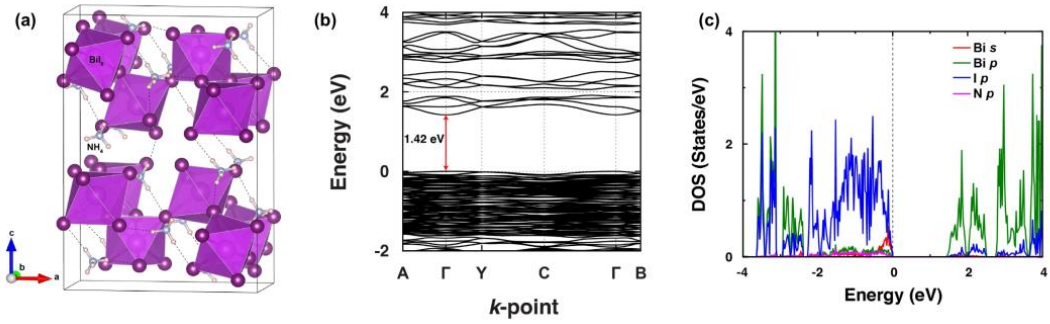

Figure 6-11 (a) Optimized geometry of the layered $(NH_4)_3Bi_2I_9$ structure; the dotted lines indicate hydrogen-bonds between I and H and N and H atoms. (b) Band structures along the k vectors of the high symmetry line of the first Brillouin zone. (c) Partial density of states indicating the Bi s, Bi p, I p, and N p orbitals.

As shown in Figure 6-11 (b), the computed band gap of $(NH_4)_3Bi_2I_9$ is 1.46 eV and it has a direct band gap (note the band gaps calculated by DFT method are typically smaller than the experimental values). DFT calculations show relatively flat valence and conduction bands, which we ascribe to the heavy effective masses of the electrons and holes. Figure 6-11 (c) shows the orbital-resolved partial density of states (PDOS) for the Bi *s*, Bi *p*, I *p*, and N *p* orbitals. The two prominent features of the PDOS are: (i) weak overlap between the Bi 6*s* orbital PDOS and the I 5*p* orbital PDOS for energies between -0.5 and 0 eV below the valence-band edge, and (ii) overlap between the Bi 6*p* orbital PDOS and the I 5*p* orbital PDOS for energies between 1.5 and 3 eV above the conduction-band edge. These orbital levels can be further visualized in real space using isosurface plots of the computed partial-charge density (PCD) of the highest band below the valence-band edge and the lowest band above the conduction-band edge. Figure 6-12 shows that the highest occupied molecular orbital (HOMO) is mainly composed of Bi 6*s* – I 5*p*

antibonding states, and the lowest unoccupied molecular orbital (LUMO) is mainly composed of Bi 6*p* – I 5*p* antibonding states. Interestingly, the HOMOs clearly reveal the stereo-active Bi 6*s* lone-pair orbitals, as shown in Figure 6-12 (a). Because of these lone-pair electrons, the Bi ions are displaced with respect to the centers of the BiI_6 octahedra.[11] Both the sharp increase near the observed absorption edge and the DFT prediction support the direct band gap of $(NH_4)_3Bi_2I_9$.

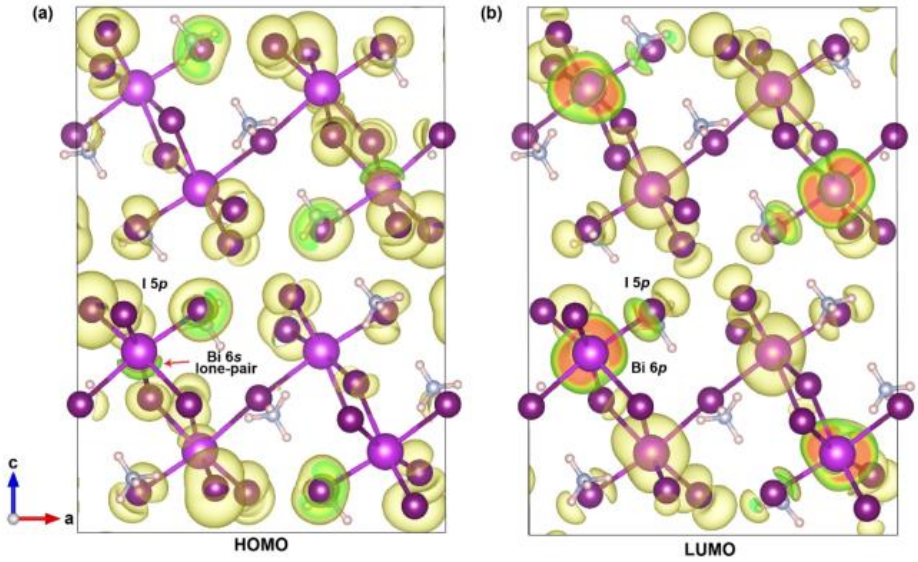

Figure 6-12 Isosurface plots of the PCD of (a) the HOMOs and (b) the LUMOs of layered $(NH_4)_3Bi_2I_9$. The colour saturation levels are between 0 (blue) and 0.0008 e/Å^3 (red).

6.3.2.5 Conductivity

In order to further examine the potential of $(NH_4)_3Bi_2I_9$ as a photovoltaic material, measurements of its conductivity were performed by Dr. Satoshi Tominaka. Several crystals were tested, and we confirmed that they are, at least intrinsically, insulating, judging by the high resistivity, which is > 3.1 x 10^8 Ωm, at 20°C measured along a diagonal line of a hexagonal plate (*ab* plane), 35 μm thick and 178 μm wide, mounted on a 20 μm gap (over the detection limit of 1 TΩ as found in previous works[163,164]). Considering the fact that closely related structures have similar band gaps to our compound and can work as the absorption layer for photovoltaics, these compounds might be extrinsically conductive. In fact, the AC impedance data for the powder sample shows a low resistivity of 0.42 Ωm (20°C) without phase shifts below 10 kHz (Figure 6-13), indicating electrical conduction (not ionic). Since the powder resistivity is very low, we tried to measure temperature-dependent conductivities in order to estimate the activation energy for the conduction. However, the resistivity increased after the measurements, up to 1.5 Ωm at 20°C (note the value mentioned above is around the lowest value), and thus we consider that the conductivity is unstable. Following these measurements, we found by using an electrometer that the conductivity is not from the bulk red material but from shiny black material on the surface. We therefore speculate that surface defects act as carriers, though further details on the origin of the conductivity are still under investigation.

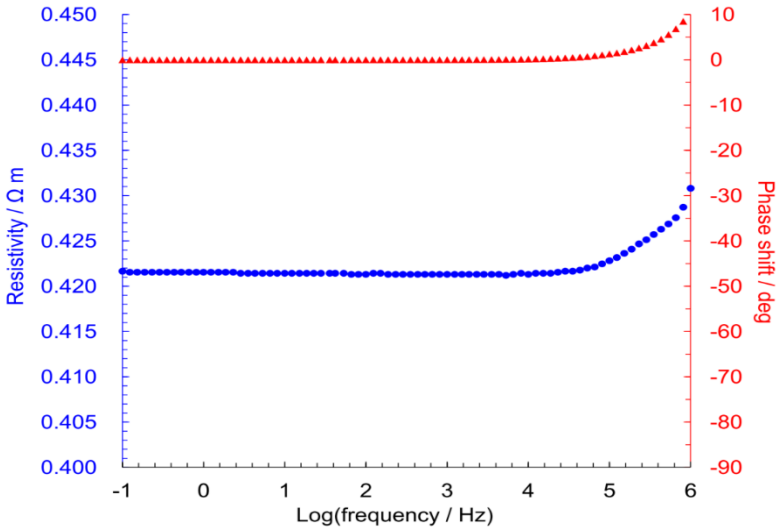

Figure 6-13 AC impedance data for the pellet sample of $(NH_4)_3Bi_2I_9$ (20°C).

6.4 Conclusions and future work

The structural diversity of perovskite and perovskite-like architectures allows a wide range of possible compositions with tailored physical properties.[106] As more attention is focused on lead-free, perovskite-related structures, a range of new hybrid compositions with framework dimensions spanning 0D to 3D are being studied. In this chapter, the dimensionality of perovskites was firstly discussed using tolerance factor as a guideline. The formation of the low dimensional perovskites with GUA filling in the A-site shows that to obtain 3D lead iodide perovskites, the size of the cation is limited to smaller than 276 pm.

To remove the toxic Pb in the structure, a dark red bismuth phase, $(NH_4)_3Bi_2I_9$, with a 2D layered perovskite-like architecture was synthesised in solution and characterised by X-ray diffraction. DFT calculations were in good agreement with the experimental X-ray diffraction results and also revealed the locations of the hydrogen atoms. The calculations also point to a significant lone pair effect on the bismuth ion. The band gap of the material was measured to be 2.04 eV (compared with 1.42 eV in the DFT calculation). The results of single crystal conductivity measurements suggest that the bulk material is insulating, but that pellets made from powders show good conductivity due to surface effects from making the pellets. For future studies, X-ray photoelectron spectroscopy and thin film fabrications are required to provide a better understanding of the application of this bismuth based perovskite family in photovoltaic devices.

Chapter 7 Conclusions and outlook

Throughout the course of the present study, metal halide HOIPs continued to revolutionise the field of new generation photovoltaic devices. Started with an efficiency of 3.8% reported in 2009,[1] this number soon soared to 15% employing the star HOIP, $MAPbI_3$, in 2013 (when this research started),[254] attributed to the remarkable device designs and thin-film optimisations. Since then, increasing attentions were drawn to materials chemistry, for example, FA perovskites was firstly introduced as a bandgap tuner in 2014[29] and crystal structures as well as cation orientations of $MAPbI_3$ and $FAPbI_3$ were revised by neutron diffraction in 2015.[67,172] Such intensive researches in the materials science field allowed tailored property designs and the current record holding efficiency is 23.6% employing silicon-perovskites tandem cells, with perovskite composition of $(Cs_{0.17}FA_{0.83}Pb(Br_{0.17}I_{0.83})_3$ (CsFA)) (February 2017).

7.1 Summary

With the aim of improving the stability and reducing the toxicity of HOIPs for photovoltaic applications, the research described in this thesis built the understanding of two main areas, namely 1) structure-property relationships of halide HOIPs, and 2) in search for alternatives to $MAPbI_3$.

Crystal chemistry of $FAPbI_3$ and $FAPbBr_3$ was firstly studied in this thesis to explore the materials' responses to external stimuli of temperature and pressure. A cubic to tetragonal phase transitions on cooling was observed and preferred orientations of the FA cations at low temperatures were detected with N-N axis aligning parallel to <110> in $P4/mbm$. Similar phase transition was also seen in $FAPbI_3$ under hydrostatic pressure. Following the observations of octahedral tilting and cation dynamics, in this thesis the anisotropic strain broadening for lead bromide perovskites were described, providing a systematic way to quantify lattice distortions. The intrinsic strains in cubic bromide perovskites were anisotropic, with <100> being the least strained direction. In additional to the structural

anisotropy due to local symmetry breaking, the mechanical anisotropy in HOIPs was also examined in the present study, with the highest Young's modulus were detected along the directions of Pb – X bonds (<100> in cubic). The robustness and ductility of HOIPs are also reflected in its static mechanical properties, making them promising candidates in deformable technologies, such as flexible photovoltaic devices, sensors, and displays. In additional to the known Pb-based perovskite, it is also shown in this thesis that the approach of replacing Pb with Bi marked a promising way to achieve non-toxic alternatives to $MAPbI_3$. The synthesized $(NH4)_3Bi_2I_9$ phase exhibited a 2D perovskite structure with band gap of 2.0 eV and thermal stability up to 230 °C. The analogue of $A_3Bi_2I_9$ (A = a monovalent cation) together with the double perovskites approach shed light on the search for more stable and eco-friendly HOIP materials for use in photovoltaic devices.

In a broader context, in additional to the advances in device design, there has been an increasing interest in the materials chemistry and intrinsic properties of HOIP materials. The research in this thesis highlights the interplay between their inorganic frameworks and the organic cations and hence have enhanced our understanding of the great chemical flexibility and structural diversity of this class of materials. It is shown in the present study that the unique physical properties of HOIPs are greatly influenced by the soft and dynamic nature of their frameworks. For lead halide perovskites, Pb – X bonds are strong but the Pb – X – Pb bridging angles are more flexible and hence octahedral tilting is common to accommodate the organic cations. Tiling angle of upto ~ 8° were measured at 120 K for $FAPbI_3$. This dynamic nature allowed high defect tolerance to lattice distortions, bringing the opportunities of mixed alloying and exploiting the "self-healing" plastic characteristics in wearable devices. In addition, the importance of the organic cation in HOIPs was sometimes neglected in previous studies, since it doesn't directly contribute to the band structures. However, the present study emphasises that the cation size, dynamics as well as hydrogen bonding conditions also contributes to the materials properties in many ways. For instance, the steric effect and rotational disorder of the cation can alter the intrinsic strain field, break the symmetry and tunes the band gaps.

7.2 Future perspectives

The outcomes of this thesis suggest research in the following areas for further investigations. Regarding the studies on the crystal chemistry, low temperature chemistry for $FAPbX_3$ can be further examined using neutron diffraction and explore the phases with ordered FA cations. Together with the displacement in Pb positions, this study is expected to shed light on designing ferroelectric semiconductors from a crystallographic point of view. In addition, the anisotropic strain model developed in this thesis can be applied a range of HOIP systems to quantify the lattice distortions and anisotropic strains. In particular, it can be applied to examine the peak profile at the foreset of phase transitions and for mixed cation or halide perovskite systems, investigations on the effects of compositions on the strain fields can be studied.

In addition, according to the reported flexibly and plasticity in the mechanical responses of HOIPs in this study, wearable and flexible photovoltaic devices can be manufactured and their performances can be studied. Furthermore, thin films technology using layered perovskites of Bi and double perovskites can also be developed for eco-friendly solar cells using the materials discussed in this work. The challenge of reducing the band gaps of the current double perovskites can be approached by doping iodide into the systems.

The structures and properties, as well as the chemical diversity of the halide HOIPs discussed in this thesis contribute to the materials design for achieving more stable. flexible and non-toxic perovskite photovoltaic devices. Designing materials with distinct physical properties tailored to their functionalities is the overall goal for future studies.

References

1 A. Kojima, K. Teshima, Y. Shirai and T. Miyasaka, *J. Am. Chem. Soc.*, 2009, **131**, 6050–6051.

2 National Renewable Energy Laboratory (NREL) Best Reserach-Cell Efficiencies, *http://www.nrel.gov/ncpv/images/efficiency_chart.jpg*, accessed at 5th July 2017.

3 S. Sasaki, C. T. Prewitt, J. D. Bass and W. A. Schulze, *Acta Crystallogr. Sect. C Cryst. Struct. Commun.*, 1987, **43**, 1668–1674.

4 D. B. Mitzi, C. Feild, W. T. Harrison and M. Guloy, *Nature*, 1994, **369**, 467–469.

5 M. T. Anderson, K. B. Greenwood, G. A. Taylor and K. R. Poeppelmeier, *Prog. Solid State Chem.*, 1993, **22**, 197–233.

6 G. Kieslich, S. Sun and A. K. Cheetham, *Chem. Sci.*, 2014, **5**, 4712–4715.

7 J. S. Forrester, E. H. Kisi, K. S. Knight and C. J. Howard, *J. Phys. Condens. Matter*, 2006, **18**, L233–L240.

8 C. J. Rhodes, *Sci. Prog.*, 2010, **93**, 223–284.

9 A. K. Cheetham and C. N. R. Rao, *Science*, 2007, **318**, 58–59.

10 G. Férey, *Chem. Mater.*, 2001, **13**, 3084–3098.

11 W. Li, Z. Wang, F. Deschler, S. Gao, R. H. Friend and A. K. Cheetham, *Nat. Rev. Mater.*, 2017, **2**, 16099.

12 P. Jain, V. Ramachandran, R. J. Clark, D. Z. Hai, B. H. Toby, N. S. Dalal, H. W. Kroto and A. K. Cheetham, *J. Am. Chem. Soc.*, 2009, **131**, 13625–13627.

13 G. Kieslich, S. Kumagai, A. C. Forse, S. Sun, S. Henke, M. Yamashita, C. P. Grey and A. K. Cheetham, *Chem. Sci.*, 2016, **7**, 5108–5112.

14 D. Weber, *Zeitschrift für Naturforsch.*, 1978, **33b**, 862–865.

15 D. B. Mitzi, *J. Chem. Soc. Dalt. Trans.*, 2001, **0**, 1–12.

16 D. B. Mitzi, S. Wang, C. a Feild, C. a Chess and a M. Guloy, *Science*, 1995, **267**, 1473–1476.

17 C. R. Kagan, *Science*, 1999, **286**, 945–947.

18 H. J. Snaith, *J. Phys. Chem. Lett.*, 2013, **4**, 3623–3630.

19 J. Berry, T. Buonassisi, D. A. Egger, G. Hodes, L. Kronik, Y. L. Loo, I. Lubomirsky, S. R. Marder, Y. Mastai, J. S. Miller, D. B. Mitzi, Y. Paz, A. M. Rappe, I. Riess, B. Rybtchinski, O. Stafsudd, V. Stevanovic, M. F. Toney, D. Zitoun, A. Kahn, D. Ginley and D. Cahen, *Adv. Mater.*, 2015, **27**, 5102–5112.

20 M. A. Green, A. Ho-Baillie and H. J. Snaith, *Nat. Photonics*, 2014, **8**, 506–514.

21 M. Liu, M. B. Johnston and H. J. Snaith, *Nature*, 2013, **501**, 395–398.

22 G. Hodes and D. Cahen, *Nat. Photonics*, 2014, **8**, 87–88.

23 W. E. I. Sha, X. Ren, L. Chen and W. C. H. Choy, *Appl. Phys. Lett.*, 2015, **106**, 221104.

24 S. P. Singh and P. Nagarjuna, *Dalton Trans.*, 2014, **43**, 5247–51.

25 E. J. W. Crossland, N. Noel, V. Sivaram, T. Leijtens, J. Alexander-Webber and H. J. Snaith, *Nature*, 2013, **495**, 215–9.

26 H.-S. Kim, S. H. Im and N.-G. Park, *J. Phys. Chem. C*, 2014, **118**, 5615–5625.

27 H.-S. Kim, C.-R. Lee, J.-H. Im, K.-B. Lee, T. Moehl, A. Marchioro, S.-J. Moon, R. Humphry-Baker, J.-H. Yum, J. E. Moser, M. Grätzel and N.-G. Park, *Sci. Rep.*, 2012, **2**, 591.

28 J. Burschka, N. Pellet, S.-J. Moon, R. Humphry-Baker, P. Gao, M. K. Nazeeruddin and M. Grätzel, *Nature*, 2013, **499**, 316–319.

29 G. E. Eperon, S. D. Stranks, C. Menelaou, M. B. Johnston, L. M. Herz and H. J. Snaith, *Energy Environ. Sci.*, 2014, **7**, 982–988.

30 M. M. Lee, J. Teuscher, T. Miyasaka, T. N. Murakami and H. J. Snaith, *Science*, 2012, **338**, 643–647.

31 H. J. Snaith, *J. Phys. Chem. Lett.*, 2013, **4**, 3623–3630.

32 M. He, D. Zheng, M. Wang, C. Lin and Z. Lin, *J. Mater. Chem. A*, 2014, **2**, 5994.

33 Y. Tidhar, E. Edri, H. Weissman, D. Zohar, G. Hodes, D. Cahen, B. Rybtchinski

and S. Kirmayer, *J. Am. Chem. Soc.*, 2014, **136**, 13249–13256.

34 H. Zhou, Q. Chen, G. Li, S. Luo, T. -b. Song, H.-S. Duan, Z. Hong, J. You, Y. Liu and Y. Yang, *Science*, 2014, **345**, 542–546.

35 M. Seetharaman S, P. Nagarjuna, P. N. Kumar, S. P. Singh, M. Deepa and M. A. G. Namboothiry, *Phys. Chem. Chem. Phys.*, 2014, **16**, 24691–24696.

36 G. Xing, N. Mathews, S. S. Lim, N. Yantara, X. Liu, D. Sabba, M. Grätzel, S. Mhaisalkar and T. C. Sum, *Nat. Mater.*, 2014, **13**, 476–80.

37 P. Qin, S. Tanaka, S. Ito, N. Tetreault, K. Manabe, H. Nishino, M. K. Nazeeruddin and M. Grätzel, *Nat. Commun.*, 2014, **5**, 3834–3840.

38 N. J. Jeon, J. H. Noh, Y. C. Kim, W. S. Yang, S. Ryu and S. Il Seok, *Nat. Mater.*, 2014, **13**, 897–903.

39 L. Meng, E.-P. Yao, Z. Hong, H. Chen, P. Sun, Z. Yang, G. Li and Y. Yang, *Adv. Mater.*, 2017, **29**, 1603826.

40 D. Shi, V. Adinolfi, R. Comin, M. Yuan, E. Alarousu, A. Buin, Y. Chen, S. Hoogland, A. Rothenberger, K. Katsiev, Y. Losovyj, X. Zhang, P. A. Dowben, O. F. Mohammed, E. H. Sargent and O. M. Bakr, *Science*, 2015, **347**, 519–522.

41 Q. Dong, Y. Fang, Y. Shao, P. Mulligan, J. Qiu, L. Cao and J. Huang, *Science*, 2015, **347**, 967–970.

42 B. Murali, M. I. Saidaminov, A. L. Abdelhady, W. Peng, J. Liu, J. Pan, O. M. Bakr and O. F. Mohammed, *J. Mater. Chem. C*, 2016, **4**, 2545–2552.

43 Y. He and G. Galli, *Chem. Mater.*, 2014, **26**, 5394–5400.

44 Z.-K. Tan, R. S. Moghaddam, M. L. Lai, P. Docampo, R. Higler, F. Deschler, M. Price, A. Sadhanala, L. M. Pazos, D. Credgington, F. Hanusch, T. Bein, H. J. Snaith and R. H. Friend, *Nat. Nanotechnol.*, 2014, **9**, 687–692.

45 F. Deschler, M. Price, S. Pathak, L. E. Klintberg, D. D. Jarausch, R. Higler, S. Hüttner, T. Leijtens, S. D. Stranks, H. J. Snaith, M. Atatüre, R. T. Phillips and R. H. Friend, *J. Phys. Chem. Lett.*, 2014, **5**, 1421–1426.

46 A. A. Zhumekenov, M. I. Saidaminov, M. A. Haque, E. Alarousu, S. P. Sarmah, B. Murali, I. Dursun, X.-H. Miao, A. L. Abdelhady, T. Wu, O. F. Mohammed and O. M. Bakr, *ACS Energy Lett.*, 2016, **1**, 32–37.

47 Q. Han, S.-H. Bae, P. Sun, Y.-T. Hsieh, Y. M. Yang, Y. S. Rim, H. Zhao, Q. Chen, W. Shi, G. Li and Y. Yang, *Adv. Mater.*, 2016, **28**, 2253–2258.

48 J.-W. Lee, D.-J. Seol, A.-N. Cho and N.-G. Park, *Adv. Mater.*, 2014, **26**, 4991–4998.

49 D. P. McMeekin, G. Sadoughi, W. Rehman, G. E. Eperon, M. Saliba, M. T. Horantner, A. Haghighirad, N. Sakai, L. Korte, B. Rech, M. B. Johnston, L. M. Herz and H. J. Snaith, *Science*, 2016, **351**, 151–155.

50 M. R. Filip, G. E. Eperon, H. J. Snaith and F. Giustino, *Nat. Commun.*, 2014, **5**, 5757.

51 F. C. Hanusch, E. Wiesenmayer, E. Mankel, A. Binek, P. Angloher, C. Fraunhofer, N. Giesbrecht, J. M. Feckl, W. Jaegermann, D. Johrendt, T. Bein and P. Docampo, *J. Phys. Chem. Lett.*, 2014, **5**, 2791–2795.

52 O. J. Weber, B. Charles and M. T. Weller, *J. Mater. Chem. A*, 2016, **4**, 15375–15382.

53 A. Poglitsch and D. Weber, *J. Chem. Phys.*, 1987, **87**, 6373–6378.

54 Y. Fu, F. Meng, M. B. Rowley, B. J. Thompson, M. J. Shearer, D. Ma, R. J. Hamers, J. C. Wright and S. Jin, *J. Am. Chem. Soc.*, 2015, **137**, 5810–5818.

55 Y. Takahashi, R. Obara, Z.-Z. Lin, Y. Takahashi, T. Naito, T. Inabe, S. Ishibashi and K. Terakura, *Dalt. Trans.*, 2011, **40**, 5563–5568.

56 T. Baikie, Y. Fang, J. M. Kadro, M. Schreyer, F. Wei, S. G. Mhaisalkar, M. Graetzel and T. J. White, *J. Mater. Chem. A*, 2013, **1**, 5628–5641.

57 L. Dimesso, M. Dimamay, M. Hamburger and W. Jaegermann, *Chem. Mater.*, 2014, **26**, 6762–6770.

58 M. A. Green and A. Ho-Baillie, *ACS Energy Lett.*, 2017, **2**, 822–830.

59 M. A. Green, Y. Jiang, A. M. Soufiani and A. Ho-Baillie, *J. Phys. Chem. Lett.*, 2015, 6, 4774–4785.

60 I. P. Swainson, R. P. Hammond, C. Soullière, O. Knop and W. Massa, *J. Solid State Chem.*, 2003, **176**, 97–104.

61 M. Szafrański and A. Katrusiak, *J. Phys. Chem. Lett.*, 2016, **7**, 3458–3466.

62 A. M. Glazer, *Acta Crystallogr. Sect. B Struct. Crystallogr. Cryst. Chem.*, 1972,

28, 3384–3392.

63 P. M. Woodward, *Acta Crystallogr. Sect. B Struct. Sci.*, 1997, **53**, 32–43.

64 M. Rodová, J. Brožek, K. Knížek and K. Nitsch, *J. Therm. Anal. Calorim.*, 2003, **71**, 667–673.

65 D. M. Trots and S. V. Myagkota, *J. Phys. Chem. Solids*, 2008, **69**, 2520–2526.

66 C. C. Stoumpos, C. D. Malliakas and M. G. Kanatzidis, *Inorg. Chem.*, 2013, **52**, 9019–9038.

67 M. T. Weller, O. J. Weber, P. F. Henry, A. M. Di Pumpo and T. C. Hansen, *Chem. Commun.*, 2015, **51**, 4180–4183.

68 J.-H. Lee, N. C. Bristowe, P. D. Bristowe and A. K. Cheetham, *Chem. Commun.*, 2015, **51**, 6434–6437.

69 J. H. Lee, N. C. Bristowe, J. H. Lee, S. H. Lee, P. D. Bristowe, A. K. Cheetham and H. M. Jang, *Chem. Mater.*, 2016, **28**, 4259–4266.

70 Y. Wang, X. Lü, W. Yang, T. Wen, L. Yang, X. Ren, L. Wang, Z. Lin and Y. Zhao, *J. Am. Chem. Soc.*, 2015, **137**, 11144–11149.

71 J. Dai, H. Zheng, C. Zhu, J. Lu and C. Xu, *J. Mater. Chem. C*, 2016, **4**, 4408–4413.

72 Y. Rakita, O. Bar-Elli, E. Meirzadeh, H. Kaslasi, Y. Peleg, G. Hodes, I. Lubomirsky, D. Oron, D. Ehre and D. Cahen, *Proc. Natl. Acad. Sci.*, 2017, **114**, 7191–7193.

73 X. Zheng, C. Wu, S. K. Jha, Z. Li, K. Zhu and S. Priya, *ACS Energy Lett.*, 2016, **1**, 1014–1020.

74 Z. Li, M. Yang, J. S. Park, S. H. Wei, J. J. Berry and K. Zhu, *Chem. Mater.*, 2016, **28**, 284–292.

75 F. Brivio, A. B. Walker and A. Walsh, *APL Mater.*, 2013, **1**.

76 W. S. Yang, J. H. Noh, N. J. Jeon, Y. C. Kim, S. Ryu, J. Seo and S. Il Seok, *Science*, 2015, **348**, 1234–1237.

77 J. H. Noh, S. H. Im, J. H. Heo, T. N. Mandal and S. Il Seok, *Nano Lett.*, 2013, **13**, 1764–1769.

78 R. Comin, G. Walters, E. S. Thibau, O. Voznyy, Z.-H. Lu and E. H. Sargent, *J. Mater. Chem. C*, 2015, **3**, 8839–8843.

79 P. Gao and M. K. Nazeeruddin, *Energy Environ. Sci.*, 2014, **1**, 2448–2463.

80 A. H. Slavney, R. W. Smaha, I. C. Smith, A. Jaffe, D. Umeyama and H. I. Karunadasa, *Inorg. Chem.*, 2017, 56, 46–55.

81 L. Q. Xie, L. Chen, Z. A. Nan, H. X. Lin, T. Wang, D. P. Zhan, J. W. Yan, B. W. Mao and Z. Q. Tian, *J. Am. Chem. Soc.*, 2017, **139**, 3320–3323.

82 C. Yi, J. Luo, S. Meloni, A. Boziki, N. Ashari-Astani, C. Grätzel, S. M. Zakeeruddin, U. Röthlisberger and M. Grätzel, *Energy Environ. Sci.*, 2016, **9**, 656–662.

83 N. K. Noel, S. D. Stranks, A. Abate, C. Wehrenfennig, S. Guarnera, A.-A. Haghighirad, A. Sadhanala, G. E. Eperon, S. K. Pathak, M. B. Johnston, A. Petrozza, L. M. Herz and H. J. Snaith, *Energy Environ. Sci.*, 2014, **7**, 3061–3068.

84 C. C. Stoumpos, L. Fraser, D. J. Clark, Y. S. Kim, S. H. Rhim, A. J. Freeman, J. B. Ketterson, J. I. Jang and M. G. Kanatzidis, *J. Am. Chem. Soc.*, 2015, **137**, 6804–6819.

85 B. W. Park, B. Philippe, X. Zhang, H. Rensmo, G. Boschloo and E. M. J. Johansson, *Adv. Mater.*, 2015, **27**, 6806–6813.

86 C. C. Stoumpos, C. D. Malliakas, J. A. Peters, Z. Liu, M. Sebastian, J. Im, T. C. Chasapis, A. C. Wibowo, D. Y. Chung, A. J. Freeman, B. W. Wessels and M. G. Kanatzidis, *Cryst. Growth Des.*, 2013, **13**, 2722–2727.

87 L. Protesescu, S. Yakunin, M. I. Bodnarchuk, F. Krieg, R. Caputo, C. H. Hendon, R. X. Yang, A. Walsh and M. V. Kovalenko, *Nano Lett.*, 2015, **15**, 3692–3696.

88 J. Song, J. Li, X. Li, L. Xu, Y. Dong and H. Zeng, *Adv. Mater.*, 2015, **27**, 7162–7167.

89 I. Chung, J. H. Song, J. Im, J. Androulakis, C. D. Malliakas, H. Li, A. J. Freeman, J. T. Kenney and M. G. Kanatzidis, *J. Am. Chem. Soc.*, 2012, **134**, 8579–8587.

90 N. J. L. K. Davis, F. J. De La Pena, M. Tabachnyk, J. M. Richter, R. D. Lamboll, E. P. Booker, F. Wisnivesky Rocca Rivarola, J. T. Griffiths, C. Ducati, S. M. Menke, F. Deschler and N. C. Greenham, *J. Phys. Chem. C*, 2017, **121**, 3790–3796.

91 J. Brgoch, A. J. Lehner, M. Chabinyc and R. Seshadri, *J. Phys. Chem. C*, 2014, **118**, 27721–27727.

92 J. H. Heo, S. H. Im, J. H. Noh, T. N. Mandal, C.-S. Lim, J. A. Chang, Y. H. Lee, H. Kim, A. Sarkar, M. K. Nazeeruddin, M. Grätzel and S. Il Seok, *Nat. Photonics*, 2013, **7**, 486–491.

93 J. Jeon, T. Eom, E. Lee, S. Kim, S. Kim, K.-H. Hong and H. Kim, *J. Phys. Chem. C*, 2017, **121**, 9508–9515.

94 L. R. Morss, M. Siegal, L. Stenger and N. Edelstein, *Inorg. Chem.*, 1970, **9**, 1771–1775.

95 I. N. Flerov, M. V. Gorev, K. S. Aleksandrov, A. Tressaud, J. Grannec and M. Couzi, *Mater. Sci. Eng. R Reports*, 1998, **24**, 81–151.

96 A. H. Slavney, T. Hu, A. M. Lindenberg and H. I. Karunadasa, *J. Am. Chem. Soc.*, 2016, **138**, 2138–2141.

97 X. G. Zhao, J. H. Yang, Y. Fu, D. Yang, Q. Xu, L. Yu, S. H. Wei and L. Zhang, *J. Am. Chem. Soc.*, 2017, **139**, 2630–2638.

98 G. Volonakis, M. R. Filip, A. A. Haghighirad, N. Sakai, B. Wenger, H. J. Snaith and F. Giustino, *J. Phys. Chem. Lett.*, 2016, **7**, 1254–1259.

99 F. Wei, Z. Deng, S. Sun, F. Xie, G. Kieslich, D. M. Evans, M. A. Carpenter, P. D. Bristowe and A. K. Cheetham, *Mater. Horiz.*, 2016, **3**, 328–332.

100 F. Wei, Z. Deng, S. Sun, F. Zhang, D. M. Evans, G. Kieslich, S. Tominaka, M. A. Carpenter, J. Zhang, P. D. Bristowe and A. K. Cheetham, *Chem. Mater.*, 2017, **29**, 1089–1094.

101 Z. Deng, F. Wei, S. Sun, G. Kieslich, A. K. Cheetham and P. D. Bristowe, *J. Mater. Chem. A*, 2016, **4**, 12025–12029.

102 V. M. Goldschmidt, *Naturwissenschaften*, 1926, **14**, 477–485.

103 J. Darriet and M. A. Subramanian, *J. Mater. Chem.*, 1995, **5**, 543–552.

104 B. Saparov and D. B. Mitzi, *Chem. Rev.*, 2016, **116**, 4558–4596.

105 A. M. Ganose, C. N. Savory and D. O. Scanlon, *J. Phys. Chem. Lett.*, 2015, **6**, 4594–4598.

106 R. L. Z. Hoye, R. E. Brandt, A. Osherov, V. Stevanovic, S. D. Stranks, M. W. B. Wilson, H. Kim, A. J. Akey, J. D. Perkins, R. C. Kurchin, J. R. Poindexter, E. N. Wang, M. G. Bawendi, V. Bulovic and T. Buonassisi, *Chem. Eur. J.*, 2016, **22**,

2605–2610.

107 I. C. Smith, E. T. Hoke, D. Solis-ibarra, M. D. Mcgehee and H. I. Karunadasa, *Angew. Chem. Int. Ed.*, 2014, 11232–11235.

108 D. H. Cao, C. C. Stoumpos, O. K. Farha, J. T. Hupp and M. G. Kanatzidis, *J. Am. Chem. Soc.*, 2015, **137**, 7843–7850.

109 J. Calabrese, N. L. Jones, R. L. Harlow, N. Herron, D. L. Thorn and Y. Wang, *J. Am. Chem. Soc.*, 1991, **113**, 2328–2330.

110 M. Era, S. Morimoto, T. Tsutsui and S. Saito, *Appl. Phys. Lett.*, 1994, **65**, 676–678.

111 Z. Xiao, W. Meng, J. Wang, D. B. Mitzi and Y. Yan, *Mater. Horiz.*, 2017, **4**, 206–216.

112 Y. Li, G. Zheng, C. Lin and J. Lin, *Solid State Sci.*, 2007, **9**, 855–861.

113 T. Matsui, A. Yamaguchi, Y. Takeoka, M. Rikukawa and K. Sanui, *Chem. Commun.*, 2002, **3**, 1094–1095.

114 J. C. Tan and A. K. Cheetham, *Chem. Soc. Rev.*, 2011, **40**, 1059–80.

115 C. T. Jin, J. D. Furman and A. K. Cheetham, *J. Am. Chem. Soc.*, 2009, **131**, 14252–14254.

116 F. Mammeri, E. Le Bourhis, L. Rozes and C. Sanchez, *J. Mater. Chem.*, 2005, **15**, 3787–3811.

117 S. Henke, W. Li and A. K. Cheetham, *Chem. Sci.*, 2014, **5**, 2392–2397.

118 W. Li, M. S. R. N. Kiran, J. L. Manson, J. Schlueter, A. Thirumurugan, U. Ramamurty and A. K. Cheetham, *Chem. Commun.*, 2013, **49**, 4471–4473.

119 J. C. Tan, T. D. Bennett and A. K. Cheetham, *Proc. Natl. Acad. Sci.*, 2010, **107**, 9938–9943.

120 J.-C. Tan, P. Jain and A. K. Cheetham, *Dalt. Trans.*, 2012, **41**, 3949–3952.

121 W. Li, A. Thirumurugan, P. T. Barton, Z. Lin, S. Henke, H. H. M. Yeung, M. T. Wharmby, E. G. Bithell, C. J. Howard and A. K. Cheetham, *J. Am. Chem. Soc.*, 2014, **136**, 7801–7804.

122 M. F. Ashby, *Materials Selection in Mechanical Design*, Butterworth-Heinemann, Fifth Ed., 2016.

123 J. Feng, *APL Mater.*, 2014, **2**, 81801.

124 J. Yu, M. Wang and S. Lin, *ACS Nano*, 2016, **10**, 11044–11057.

125 M. M. Tavakoli, K. H. Tsui, Q. Zhang, J. He, Y. Yao, D. Li and Z. Fan, *ACS Nano*, 2015, **9**, 10287–10295.

126 H. Zhou, Y. Shi, K. Wang, Q. Dong, X. Bai, Y. Xing, Y. Du and T. Ma, *J. Phys. Chem. C*, 2015, **119**, 4600–4605.

127 C. Gu and J. S. Lee, *ACS Nano*, 2016, **10**, 5413–5418.

128 L. Wang, K. Wang, G. Xiao, Q. Zeng and B. Zou, *J. Phys. Chem. Lett.*, 2016, **7**, 5273–5279.

129 L. Wang, K. Wang and B. Zou, *J. Phys. Chem. Lett.*, 2016, **7**, 2556–2562.

130 Y. Lee, D. B. Mitzi, P. W. Barnes and T. Vogt, *Phys. Rev. B*, 2003, **68**, 20103.

131 A. N. Beecher, O. E. Semonin, J. M. Skelton, J. M. Frost, M. W. Terban, H. Zhai, A. Alatas, J. S. Owen, A. Walsh and S. J. L. Billinge, *ACS Energy Lett.*, 2016, **1**, 880–887.

132 B. R. Vincent, K. N. Robertson, T. S. Cameron and O. Knop, *Can. J. Chem.*, 1987, **65**, 1042–1046.

133 M. I. Saidaminov, A. L. Abdelhady, G. Maculan and O. M. Bakr, *Chem. Commun.*, 2015, **51**, 17658–17661.

134 K. Hasegawa, *Rigaku J.*, 2012, **28**, 14–18.

135 G. M. Sheldrick, *Acta Cryst.*, 2008, **A64**, 112–122.

136 G. M. . Sheldrick, *Acta Cryst.*, 2015, **A71**, 3–8.

137 O. V. Dolomanov, L. J. Bourhis, R. J. Gildea, J. A. K. Howard, H. Puschmann, S. K., W. L., P. G. and S. R., *J. Appl. Crystallogr.*, 2009, **42**, 339–341.

138 R. E. Dinnebier, *Powder diffraction : theory and practice*, RSC Publ, 2009.

139 R. W. Cheary, A. Coelho and IUCr, *J. Appl. Crystallogr.*, 1992, **25**, 109–121.

140 R. W. Cheary and A. A. Coelho, *J. Appl. Crystallogr.*, 1998, **31**, 851–861.

141 S. P. Thompson, J. E. Parker, J. Marchal, J. Potter, A. Birt, F. Yuan, R. D. Fearn, A. R. Lennie, S. R. Street and C. C. Tang, *J. Synchrotron Radiat.*, 2011, **18**, 637–648.

142 H. Nowell, S. A. Barnett, K. E. Christensen, S. J. Teat and D. R. Allan, *J. Synchrotron Radiat.*, 2012, **19**, 435–441.

143 S. A. Moggach, D. R. Allan, S. Parsons and J. E. Warren, *J. Appl. Crystallogr.*, 2008, **41**, 249–251.

144 CrysAlis CCD. CrysAlis RED and associated programs. Abingdon: Oxford Diffraction Ltd., 2008.

145 W. C. Oliver and G. M. Pharr, *J. Mater. Res.*, 1992, **7**, 1564–1583.

146 W. C. Oliver and G. M. Pharr, *J. Mater. Res.*, 2004, **19**, 3–20.

147 G. Kresse and J. Furthmüller, *Phys. Rev. B*, 1996, **54**, 11169–11186.

148 P. E. Blöchl, *Phys. Rev. B*, 1994, **50**, 17953–17979.

149 J. P. Perdew, K. Burke and M. Ernzerhof, *Phys. Rev. Lett.*, 1996, **77**, 3865–3868.

150 J. Even, L. Pedesseau, J.-M. Jancu and C. Katan, *J. Phys. Chem. Lett.*, 2013, **4**, 2999–3005.

151 G. Kresse and D. Joubert, *Phys. Rev. B*, 1999, **59**, 1758–1775.

152 G. Kresse and J. Hafner, *Phys. Rev. B*, 1993, **47**, 558–561.

153 G. Kresse and J. Hafner, *Phys. Rev. B*, 1994, **49**, 14251–14269.

154 G. Kresse and J. Furthmüller, *Comput. Mater. Sci.*, 1996, **6**, 15–50.

155 J. Klimeš, D. R. Bowler and A. Michaelides, *Phys. Rev. B*, 2011, **83**, 195131.

156 J. D. Pack and H. J. Monkhorst, *Phys. Rev. B*, 1977, **16**, 1748–1749.

157 C. Elsässer, M. Fähnle, C. T. Chan and K. M. Ho, *Phys. Rev. B*, 1994, **49**, 13975–13978.

158 S. Grimme, *J. Comput. Chem.*, 2006, **27**, 1787–1799.

159 D. A. Egger and L. Kronik, *J. Phys. Chem. Lett.*, 2014, **5**, 2728–2733.

160 W. Humphrey, A. Dalke and K. Schulten, *J. Mol. Graph.*, 1996, **14**, 33–38.

161 P. Kubelka, *J. Opt. Soc. Am.*, 1948, **38**, 448–457.

162 J. Tauc, *Mater. Res. Bull.*, 1968, **3**, 37–46.

163 S. Tominaka, A. K. Cheetham, J. A. Chisholm, P. R. Edgington, P. McCabe, E. Pidcock, L. Rodriguez-Monge, R. Taylor, J. van de Streek and P. A. Wood, *RSC*

Adv., 2014, **4**, 54382–54387.

164 S. Tominaka, S. Henke and A. K. Cheetham, *CrystEngComm*, 2013, **15**, 9400–9407.

165 S. Tominaka, H. Hamoudi, T. Suga, T. D. Bennett, A. B. Cairns and A. K. Cheetham, *Chem. Sci.*, 2015, **6**, 1465–1473.

166 B. V. Lotsch, *Angew. Chem. Int. Ed.*, 2014, **53**, 635–637.

167 A. L. Montero-Alejo, E. Menendez-Proupin, D. Hidalgo-Rojas, P. Palacios, P. Wahnon and J. C. Conesa, *J. Phys. Chem. C*, 2016, **120**, 7976–7986.

168 J. M. Frost and A. Walsh, *Acc. Chem. Res.*, 2016, 49, 528–535.

169 A. Sharenko and M. F. Toney, *J. Am. Chem. Soc.*, 2016, **138**, 463–470.

170 A. Jaffe, Y. Lin, C. M. Beavers, J. Voss, W. L. Mao and H. I. Karunadasa, *ACS Cent. Sci.*, 2016, **2**, 201–209.

171 O. Knop, R. E. Wasylishen, M. A. White, T. S. Cameron and M. J. M. Van Oort, *Can. J. Chem.*, 1990, **68**, 412–422.

172 M. T. Weller, O. J. Weber, J. M. Frost and A. Walsh, *J. Phys. Chem. Lett.*, 2015, **6**, 3209–3212.

173 D. H. Fabini, C. C. Stoumpos, G. Laurita, A. Kaltzoglou, A. G. Kontos, P. Falaras, M. G. Kanatzidis and R. Seshadri, *Angew. Chem. Int. Ed.*, 2016, **55**, 15392–15396.

174 I. P. Swainson, M. G. Tucker, D. J. Wilson, B. Winkler and V. Milman, *Chem. Mater.*, 2007, **19**, 2401–2405.

175 Y. Wang, X. Lü, W. Yang, T. Wen, L. Yang, X. Ren, L. Wang, Z. Lin and Y. Zhao, *J. Am. Chem. Soc.*, 2015, **137**, 11144–11149.

176 G. Liu, L. Kong, J. Gong, W. Yang, H. K. Mao, Q. Hu, Z. Liu, R. D. Schaller, D. Zhang and T. Xu, *Adv. Funct. Mater.*, 2017, **27**, 1604208.

177 P. Wang, J. Guan, D. T. K. Galeschuk, Y. Yao, C. F. He, S. Jiang, S. Zhang, Y. Liu, M. Jin, C. Jin and Y. Song, *J. Phys. Chem. Lett.*, 2017, **8**, 2119–2125.

178 M. Szafrański and A. Katrusiak, *J. Phys. Chem. Lett.*, 2017, **8**, 2496–2506.

179 T. Baikie, N. S. Barrow, Y. Fang, P. J. Keenan, P. R. Slater, R. O. Piltz, M. Gutmann, S. G. Mhaisalkar, T. J. White, D. Credgington, F. Hanusch, T. B. Bein, H. J. Snaith and R. H. Friend, *J. Mater. Chem. A*, 2015, **3**, 9298–9307.

180 T. Chen, B. J. Foley, C. Park, C. M. Brown, L. W. Harriger, J. Lee, J. Ruff, M. Yoon, J. J. Choi and S.-H. Lee, *Sci. Adv.*, 2016, **2**.

181 T. J. Jacobsson, L. J. Schwan, M. Ottosson, A. Hagfeldt and T. Edvinsson, *Inorg. Chem.*, 2015, **54**, 10678–10685.

182 M. A. Carignano, Y. Saeed, S. A. Aravindh, I. S. Roqan, J. Even and C. Katan, *Phys. Chem. Chem. Phys.*, 2016, **18**, 27109–27118.

183 K. T. Butler, K. Svane, G. Kieslich, A. K. Cheetham and A. Walsh, *Phys. Rev. B - Condens. Matter Mater. Phys.*, 2016, **94**, 180103.

184 C. Motta, F. El-Mellouhi and S. Sanvito, *Phys. Rev. B - Condens. Matter Mater. Phys.*, 2016, **93**, 235412.

185 N. Onoda-Yamamuro, T. Matsuo and H. Suga, *J. Phys. Chem. Solids*, 1990, **51**, 1383–1395.

186 K. T. Butler, A. Walsh, A. K. Cheetham and G. Kieslich, *Chem. Sci.*, 2016, **7**, 6316–6324.

187 S. Sun, Z. Deng, Y. Wu, F. Wei, F. Isikgor, F. Brivio, M. Gaultois, J. Ouyang, P. Bristowe, T. Cheetham and G. Kieslich, *Chem. Commun.*, 2017, **53**, 7537–7540.

188 F. C. Hanusch, E. Wiesenmayer, E. Mankel, A. Binek, P. Angloher, C. Fraunhofer, N. Giesbrecht, J. M. Feckl, W. Jaegermann, D. Johrendt, T. Bein and P. Docampo, *J. Phys. Chem. Lett.*, 2014, **5**, 2791–2795.

189 B. Murali, E. Yengel, W. Peng, Z. Chen, M. S. Alias, E. Alarousu, B. S. Ooi, V. Burlakov, A. Goriely, M. Eddaoudi, O. M. Bakr and O. F. Mohammed, *J. Phys. Chem. Lett.*, 2017, **8**, 137–143.

190 E. H. Kisi, J. S. Forrester and K. S. Knight, *Acta Crystallogr. C.*, 2006, **62**, i46-8.

191 J. Frantti, *J. Phys. Chem. B*, 2008, 112, 6521–6535.

192 E. Article, G. Laurita, D. H. Fabini, C. C. Stoumpos, M. G. Kanatzidis and R. Seshadri, *Chem. Sci.*, 2017, **0**, 1–8.

193 R. E. Dinnebier and S. J. L. Billinge, Eds., *Powder diffraction: theory and practice*, Royal Society of Chemistry, Cambridge, 2008.

194 M. Attfield, P. Barnes, J. K. Cockcroft and H. Driessen, *Internet Course: Powder Diffraction*, Birkbeck College, London, UK.

195 T. Ungár, *Scr. Mater.*, 2004, **51**, 777–781.

196 G. Williamson and W. Hall, *Acta Metall.*, 1953, **1**, 22–31.

197 P. W. Stephens, *J. Appl. Crystallogr.*, 1999, **32**, 281–289.

198 A. Sarkar, P. Mukherjee and P. Barat, *Mater. Sci. Eng. A*, 2008, **485**, 176–181.

199 R. Ohmann, L. K. Ono, H.-S. Kim, H. Lin, M. V. Lee, Y. Li, N.-G. Park and Y. Qi, *J. Am. Chem. Soc.*, 2015, **137**, 16049–16054.

200 A. Perumal, S. Shendre, M. Li, Y. K. E. Tay, V. K. Sharma, S. Chen, Z. Wei, Q. Liu, Y. Gao, P. J. S. Buenconsejo, S. T. Tan, C. L. Gan, Q. Xiong, T. C. Sum and H. V. Demir, *Sci. Rep.*, 2016, **6**, 36733.

201 L. Protesescu, S. Yakunin, M. I. Bodnarchuk, F. Bertolotti, N. Masciocchi, A. Guagliardi and M. V. Kovalenko, *J. Am. Chem. Soc.*, 2016, **138**, 14202–14205.

202 A. Leineweber and E. J. Mittemeijer, *J. Appl. Crystallogr.*, 2004, **37**, 123–135.

203 B. H. Toby, *J. Appl. Crystallogr.*, 2001, **34**, 210–213.

204 D. Kubicki, D. Prochowicz, A. Hofstetter, P. Pechy, S. M. Zakeeruddin, M. Grätzel, L. Emsley, D. J. Kubicki and P. Péchy, *J. Am. Chem. Soc.*, 2017, accepted manuscript.

205 D. B. Mitzi and K. Liang, *J. Solid State Chem.*, 1997, **134**, 376–381.

206 D. H. Fabini, G. Laurita, J. S. Bechtel, C. C. Stoumpos, H. A. Evans, A. G. Kontos, Y. S. Raptis, P. Falaras, A. Van der Ven, M. G. Kanatzidis and R. Seshadri, *J. Am. Chem. Soc.*, 2016, **138**, 11820–11832.

207 O. Selig, A. Sadhanala, C. Müller, R. Lovrincic, Z. Chen, Y. L. A. Rezus, J. M. Frost, T. L. C. Jansen and A. A. Bakulin, *J. Am. Chem. Soc.*, 2017, **139**, 4068–4074.

208 F. Zhao, D. Chen, S. Chang, H. Huang, K. Tong, C. Xiao, S. Chou, H. Zhong, Q. Pei, A. Huan, Q. Xiong, T. Siegrist, C. Xu, Z. Yu, Y. Jin, Y. Liu, Q. Ding, D. Di, L. Yang, G. Xing, H. Tian, C. Jin, F. Gao, R. H. Friend, J. Wang and W. Huang, *J. Mater. Chem. C*, 2017, **5**, 531–538.

209 G. Xing, N. Mathews, S. Sun, S. S. Lim, Y. M. Lam, M. Gratzel, S. Mhaisalkar and T. C. Sum, *Science*, 2013, **342**, 344–347.

210 S. A. Bretschneider, J. Weickert, J. A. Dorman and L. Schmidt-Mende, *APL*

Mater., 2014, **2**, 40701.

211 S. Sun, Y. Fang, G. Kieslich, T. J. White and A. K. Cheetham, *J. Mater. Chem. A*, 2015, **3**, 18450–18455.

212 Y. Rakita, S. R. Cohen, N. K. Kedem, G. Hodes and D. Cahen, *MRS Commun.*, 2015, **5**, 623–629.

213 M. A. Reyes-Martinez, A. L. Abdelhady, M. I. Saidaminov, D. Y. Chung, O. M. Bakr, M. G. Kanatzidis, W. O. Soboyejo and Y.-L. Loo, *Adv. Mater.*, 2017, **29**, 1606556.

214 M. K. Mishra, U. Ramamurty, G. R. Desiraju, S. State, S. C. Unit and S. Arabia, 2015, **34**, 1–5.

215 R. M. Mohamed, M. K. Mishra, L. M. AL-Harbi, M. S. Al-Ghamdi and U. Ramamurty, *RSC Adv.*, 2015, **5**, 64156–64162.

216 A. C. Fischer-Cripps, *Surf. Coatings Technol.*, 2006, **200**, 4153–4165.

217 J. C. Tan, C. A. Merrill, J. B. Orton and A. K. Cheetham, *Acta Mater.*, 2009, **57**, 3481–3496.

218 A. Walsh, *J. Phys. Chem. C*, 2015, **119**, 5755–5760.

219 J. E. Huheey, E. A. Keiter, R. L. Keiter and O. K. Medhi, *Inorganic chemistry : principles of structure and reactivity*, Pearson Education, 2006.

220 R. D. Shannon, *Acta Crystallogr. Sect. A*, 1976, **32**, 751–767.

221 L. Pauling, *The Nature of the Chemical Bond*, Cornell University Press, USA, 3rd ed., 1960.

222 X.-Z. Li, B. Walker and A. Michaelides, *Proc. Natl. Acad. Sci. U. S. A.*, 2011, **108**, 6369–6373.

223 M. L. Huggins, *J. Am. Chem. Soc.*, 1953, **75**, 4126–4133.

224 R. J. Worhatch, H. Kim, I. P. Swainson, A. L. Yonkeu and S. J. L. Billinge, *Chem. Mater.*, 2008, **20**, 1272–1277.

225 J. J. Choi, X. Yang, Z. M. Norman, S. J. L. Billinge and J. S. Owen, *Nano Lett.*, 2014, **14**, 127–133.

226 J. S. Bechtel, R. Seshadri and A. Van der Ven, *J. Phys. Chem. C*, 2016, **120**, 12403–12410.

227 T. D. Bennett, J.-C. Tan, S. A. Moggach, R. Galvelis, C. Mellot-Draznieks, B. A. Reisner, A. Thirumurugan, D. R. Allan and A. K. Cheetham, *Chem. Eur. J.*, 2010, **16**, 10684–10690.

228 G. Divitini, S. Cacovich, F. Matteocci, L. Cinà, A. Di Carlo and C. Ducati, *Nat. Energy*, 2016, **1**, 15012.

229 Q. Jiang, D. Rebollar, J. Gong, E. L. Piacentino, C. Zheng and T. Xu, *Angew. Chem.*, 2015, **127**, 7727–7730.

230 Q. Chen, N. De Marco, Y. Yang, T. Bin Song, C. C. Chen, H. Zhao, Z. Hong, H. Zhou and Y. Yang, *Nano Today*, 2015, **10**, 355–396.

231 Z. Fan, K. Sun and J. Wang, *J. Mater. Chem. A*, 2015, **3**, 18809–18828.

232 L.-Q. Fan and J.-H. Wu, *Acta Crystallogr. Sect. E Struct. Reports Online*, 2007, **63**, i189–i189.

233 M. Safdari, A. Fischer, B. Xu, L. Kloo, J. M. Gardner, T. Heumuller, M. G. Christoforo, M. D. McGehee, F. D. Angelis, Y. Yang, M. Gratzel and N.-G. Park, *J. Mater. Chem. A*, 2015, **3**, 9201–9207.

234 M. Szafrański and K. Ståhl, *J. Solid State Chem.*, 2007, **180**, 2209–2215.

235 G. Giorgi, J. I. Fujisawa, H. Segawa and K. Yamashita, *J. Phys. Chem. C*, 2015, **119**, 4694–4701.

236 M. Szafrański, *Thermochim. Acta*, 1997, **307**, 177–183.

237 M. Szafran and A. Katrusiak, *Phys. Rev. B*, 2000, **61**, 1026–1035.

238 A. D. Jodlowski, A. Yepez, R. Luque, L. Camacho and G. de Miguel, *Angew. Chem. Int. Ed.*, 2016, **55**, 14972–14977.

239 L. Dimesso, A. Quintilla, Y.-M. Kim, U. Lemmer and W. Jaegermann, *Mater. Sci. Eng. B*, 2016, **204**, 27–33.

240 N. De Marco, H. Zhou, Q. Chen, P. Sun, Z. Liu, L. Meng, E.-P. Yao, Y. Liu, A. Schiffer and Y. Yang, *Nano Lett.*, 2016, **16**, 1009–1016.

241 K. Tanaka, R. Ozawa, T. Umebayashi, K. Asai, K. Ema and T. Kondo, *Phys. E Low-dimensional Syst. Nanostructures*, 2005, **25**, 378–383.

242 K. D Karlin, *Progress in Inorganic Chemistry*, John Wiley & Sons, Inc., Hoboken, NJ, USA, 1996, vol. 48.

243 F. Hao, C. C. Stoumpos, D. H. Cao, R. P. H. Chang and M. G. Kanatzidis, *Nat. Photonics*, 2014, **8**, 489–494.

244 S. L. Gorbach, *Gastroenterology*, 1990, **99**, 863–75.

245 P. Szklarz, A. Pietraszko, R. Jakubas, G. Bator, P. Zieliński and M. Gałazka, *J. Phys. Condens. Matter*, 2008, **20**, 255221.

246 B. Y. B. Chabot and E. Parthe, *Acta Crystallogr. Sect. B*, 1978, **B34**, 645–8.

247 H. Zhang, L. Fang and R.-Z. Yuan, *Acta Crystallogr. Sect. E Struct. Reports Online*, 2005, **61**, i70–i72.

248 K. Yamada, H. Sera, S. Sawada, H. Tada, T. Okuda and H. Tanaka, 1997, **325**, 319–325.

249 B. Saparov, F. Hong, J.-P. Sun, H.-S. Duan, W. Meng, S. Cameron, I. G. Hill, Y. Yan and D. B. Mitzi, *Chem. Mater.*, 2015, **27**, 5622–5632.

250 A. J. Lehner, D. H. Fabini, H. A. Evans, C. A. Hébert, S. R. Smock, J. Hu, H. Wang, J. W. Zwanziger, M. L. Chabinyc and R. Seshadri, *Chem. Mater.*, 2015, **27**, 7137–7148.

251 R. Deblieck, G. Van Tendeloo, J. Van Landuyt and S. Amelinckx, *Acta Crystallogr. Sect. B Struct. Sci.*, 1985, **41**, 319–329.

252 H. M. Gladney and G. B. Street, *J. Inorg. Nucl. Chem.*, 1968, **30**, 2–6.

253 V. I. Sidey, Y. V. Voroshilov, S. V. Kun and E. Y. Peresh, *J. Alloys Compd.*, 2000, **296**, 53–58.

254 G. Hodes, *Science*, 2013, **342**, 317–318.

Appendix

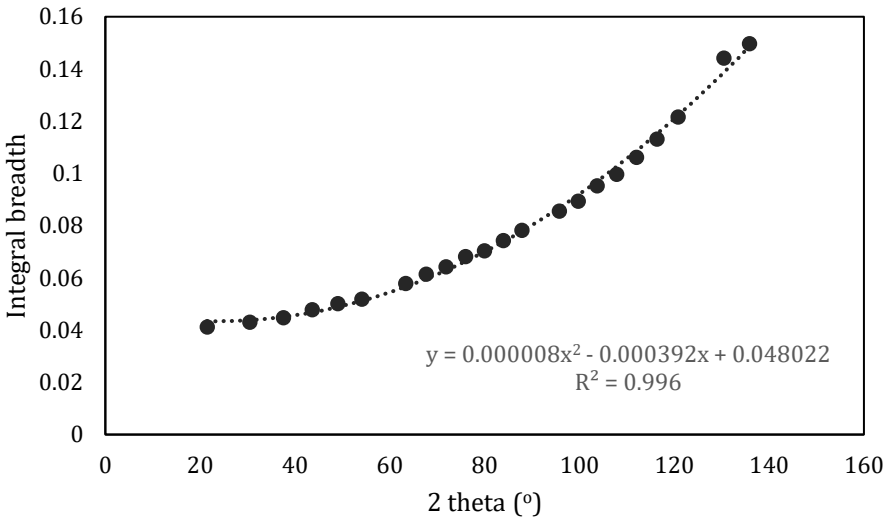

Figure-A 1 Instrumental broadening (integral breadth) using measured with LaB_6 on the Bruker D8 diffractometer as described in Chapter 2.

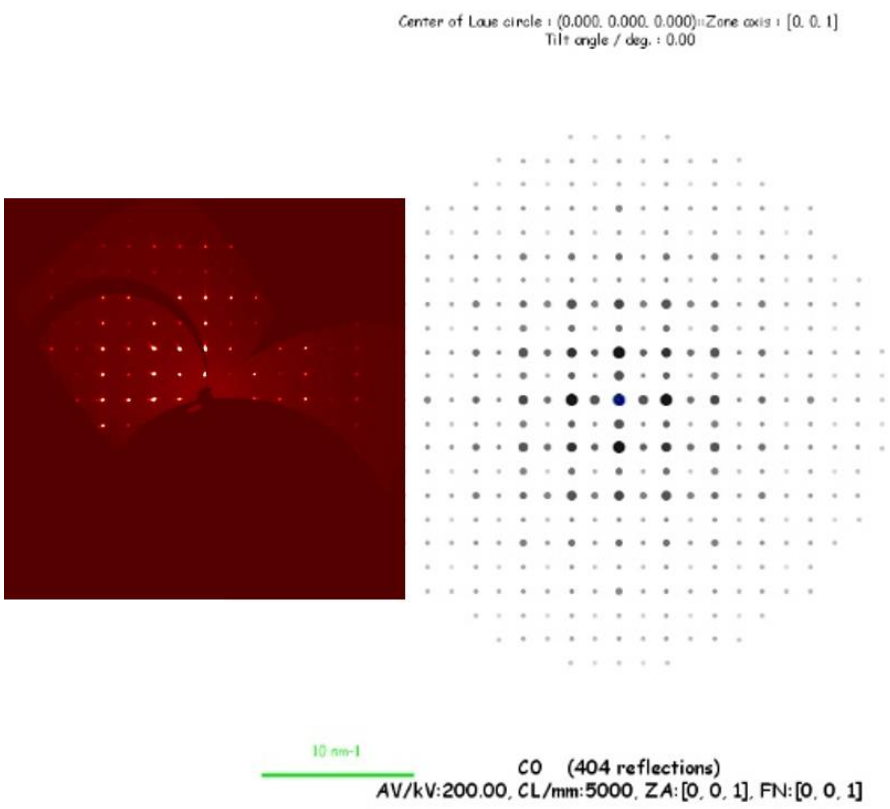

Figure-A 2 X-ray diffraction patterns along [001] of $FAPbI_3$ at 300 K. The collected experimental pattern (left) is consistent with the simulated pattern using JEMS image simulation software (right) after structural solutions in the space group of $Pm\bar{3}m$.

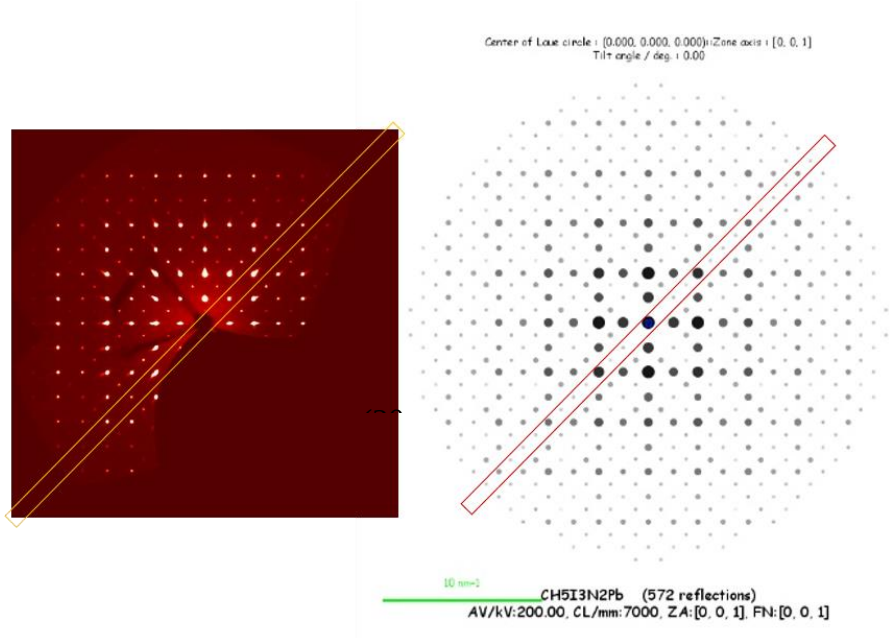

Figure-A 3 The structure of $FAPbI_3$ at 250 K was solved in $\boldsymbol{Im\bar{3}}$ (a = b = c = 12.6895(8) A), Rwp = 5.62%), and X-ray patterns are shown along [001]. The collected experimental pattern (left)

reveals systematic absences along (hh0) where h is odd (highlighted in rectangle). However, reflections are expected at these positions in the simulated patterns using JEMS (right).

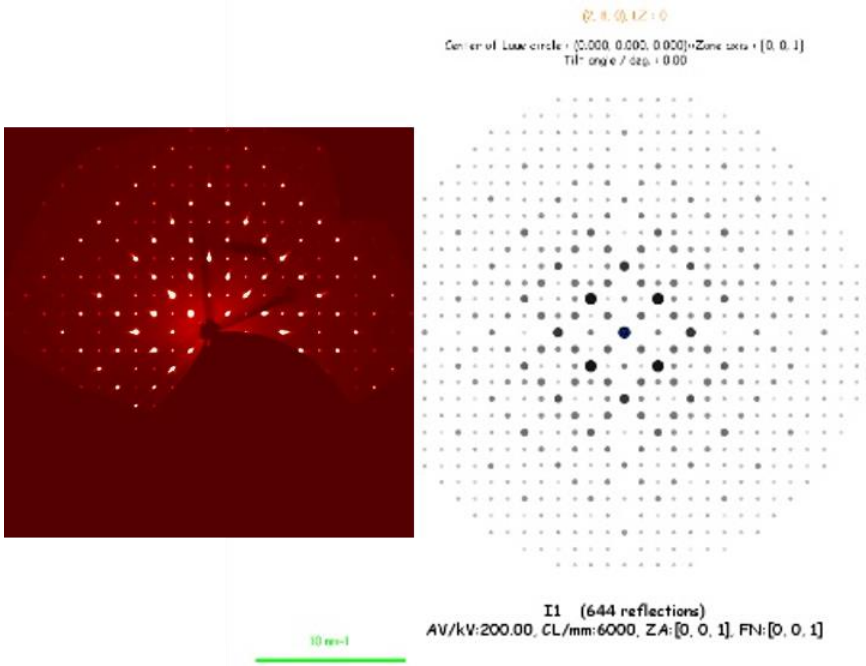

Figure-A 4 Experimental and simulated X-ray diffraction patterns of $[(NH_2)_2CH]PbI_3$ at 250 K along [001] in P4/mbm. The collected experimental patterns (left) are consistent with the simulated patterns using JEMS (right) respectively after structural solutions in $\boldsymbol{P4/mbm}$. Most reflections from different components of the twins overlap, however, the intensities of the reflections are influenced by the intensities of different twinning components.

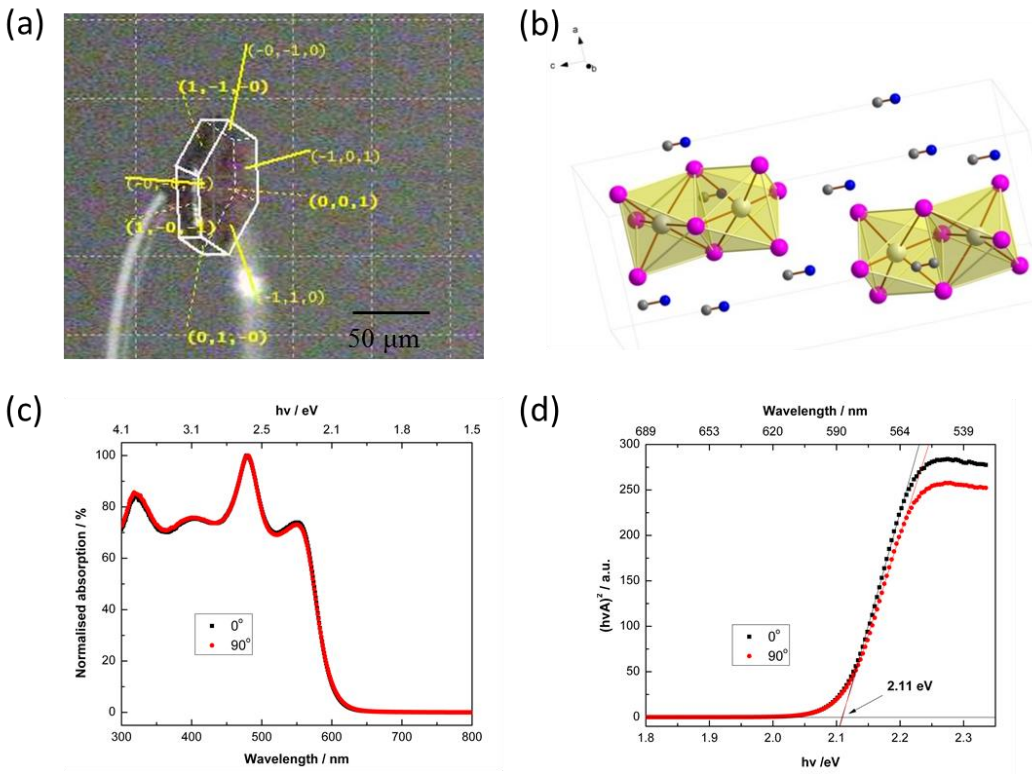

Figure-A 5 (a) Photograph of a typical single crystal $MA_3Bi_2I_9$ with face indexing using SCXRD. (b)The dimer structure of $MA_3Bi_2I_9$, with the crystal structure showing the face sharing polyhedra. Silver, purple, blue and grey spheres represent bismuth, iodine, carbon and nitrogen atoms respectively. (c) The absorption spectrum and (d) Tauc relation plotted using reflectance data on a powder sample of $MA_3Bi_2I_9$. The sample was rotated 90° to ensure accuracy and the average was used to calculate the band gap.

Table-A 1 Details of change in lattice parameters of a representative $FAPbI_3$ single crystal in the temperature range of 240 K – 280 K.

	Temperature (K)	*a*(Å)	c (Å)	Unit Cell Volume ($Å^3$)
1	240	8.9584(4)	6.3360(2)	508.49(17)
3	260	9.0099(9)	6.3803(4)	517.95(8)
4	280	6.3692(2)		258.376(14)
5	300	6.3722(2)		258.748(12)

Table-A 2 Anisotropic strain parameters refined by Topas at 290 K.

Anisotropic strain parameters at 290 K	S_{400}	S_{220}	M_{hkl}		
	771(169)	21150(1582)	6009559		
plane	Cal M_{hkl}	Cal 2θ°*	Cal FWHM*	Obs 2θ°	Obs FIHM
001	771	7.71	0.0069	7.89	0.0292
011	22693	10.92	0.0265	11.17	0.0495
111	65765	13.38	0.0369	13.70	0.0414
002	12340	15.46	0.0139	15.83	0.0348
021	97712	17.28	0.0351	17.72	0.0563
211	204235	18.95	0.0464	19.42	0.0689
022	363085	21.93	0.0538	22.47	0.0789
221	533058	23.26	0.0616	23.85	0.0785
031	253595	24.54	0.0404	25.16	0.0620
222	1052234	26.94	0.0755	27.61	0.1012
032	836222	28.05	0.0648	28.76	0.0897
321	1111947	29.13	0.0722	29.88	0.0956
004	197439	31.20	0.0461	31.99	0.0286

* The calculated angles were deduced from the calculated *d* spacings output from Topas. The calculated peak profile was obtained by applying the anisotropic strain parameters on the Lorentzian peak shape and only sample broadening was considered, without taking into account the instrumental effects.